

Transport and Magnetism in Mesoscopic Superconductors

A dissertation submitted to the
SWISS FEDERAL INSTITUTE OF TECHNOLOGY ZURICH
(ETH Zürich)

for the degree of
Doctor of Natural Sciences

presented by
ALBAN LUC ANDRÉ FAUCHÈRE
Dipl. Phys. ETH
born May 21, 1971
citizen of Urdorf ZH, Evolène VS

accepted on the recommendation of
Prof. Dr. G. Blatter, examiner
Prof. Dr. G. Schön, co-examiner
Dr. V. Geshkenbein, co-examiner

Acknowledgments

I am indebted to Gianni Blatter, who has supervised my thesis with great attention and diligence, for his choice of a fascinating problem to work on, for teaching me a scientific research style, for his availability for long hours of debate, for his expertise in writing, and for the friendly and team-oriented atmosphere in his group.

I am grateful to Prof. Gerd Schön, for being my co-examiner and providing several opportunities to pursue scientific interests, at the Nato Advanced Study Institute and at the University of Karlsruhe. The long-standing collaboration and friendship with Wolfgang Belzig, with whom I have shared the passions on paramagnetism and proximity effect, has been most valuable to me.

I'm grateful to Maurice Rice for his interest in my work and his perspectives on science and life. Vadim Geshkenbein as the *advocatus diaboli* has provided me with sharp-minded criticism and most stimulating discussions. I thank my friends and colleagues at the institute, Daniel Agterberg, Walter Aschbacher, Malek Bou-Diab, Thomas Chen, Matthew Dodgson, Beat Frischmuth, Pierre-Alain Genilloud, Denis Gorokhov, Stefan Haas, Elmar Heeb, Rolf Heeb, Karyn Le Hur, Thierry Müller, Anne van Otterlo, Kai Schnee, Andreas Schönenberger, Manfred Sigrist, Thomas Siller, Matthias Troyer, Orlando Wagner, and Peter Widerin for fruitful exchanges, excellent collaboration on student exercises, late-night philosophical discussions and shared bottles of wine. I'm grateful to Klaus Hepp for promoting me within the Swiss Study Foundation. Urs Ledermann contributed to this thesis through his diploma project.

I have drawn much motivation from the enthusiasm of Prof. Ana-Celia Mota for her experiments and have profited from numerous discussions with Roberto Frassanito and Bernd Müller-Allinger. I acknowledge fruitful discussions and collaborations with Christoph Bruder, Rosario Fazio, Mikhail Feigel'man, Christian Glattli, Lev Ioffe, Gordey Lesovik, Thomas Meyer, Marc Sanquer, and Andrei Zaikin.

Finally, I am most grateful to Claudia, Alexandre, Ivan, Marie-Pierre, Kay, Gisèle and Jean-Luc, who have been a wonderful family to me all these years.

Contents

Acknowledgments	iii
Abstract	ix
Zusammenfassung	xi
1 Introduction	1
2 Nonlinearity in normal-metal – superconductor transport: Conductance and shot noise	11
2.1 Scattering matrix approach to normal-metal – superconductor transport	11
2.1.1 Introduction	11
2.1.2 Spectral conductance in the Andreev approximation	17
2.1.3 Double barrier NINIS junction	19
2.1.4 Discussion	25
2.2 Finite voltage shot noise in normal-metal – superconductor junctions	26
2.2.1 Introduction	26
2.2.2 Interplay between normal scattering and Andreev reflection . .	28
2.2.3 Double barrier junction	31
2.2.4 Discussion	33
3 Magnetic response of a normal-metal – superconductor structure: Nonlocality	35
3.1 Introduction	35
3.2 Quasi-classical equations and proximity effect	36
3.2.1 Eilenberger equation	36
3.2.2 Clean NS slab	38
3.3 Magnetic screening	40
3.3.1 Linear response kernel	40
3.3.2 Clean limit	43
3.4 Sensitivity to impurities	44

3.4.1	Ballistic regime	44
3.4.2	Diffusive regime	48
3.5	Discussion	49
4	Magnetic breakdown in a normal-metal – superconductor proximity structure	51
4.1	Introduction	51
4.2	Constitutive relations	53
4.3	Magnetostatics	54
4.4	Thermodynamics	55
4.5	Experiment	59
4.6	Discussion	62
5	Paramagnetic instability of Andreev electrons	63
5.1	Introduction	63
5.2	Zero energy bound states	64
5.3	Spontaneous currents and magnetization	67
5.4	Discussion	70
6	Nonlocality in Josephson junctions: Anomalous current – flux periodicity	73
6.1	Introduction	73
6.2	Current density pattern	74
6.3	Critical current – flux dependence	78
6.4	Discussion	80
7	Quiet SDS Josephson junctions for quantum computing	83
7.1	Introduction	83
7.2	Device functionality	85
7.3	Discussion	89
8	Conclusions and Outlook	91

<i>CONTENTS</i>	vii
A Bogoliubov-de Gennes equations	95
B Quasi-classical Green's function technique	99
B.1 Eilenberger equations	99
B.2 Quasi-classical current expression	102
C Response kernel	105
List of publications	121
Curriculum Vitae	123

Abstract

Superconductivity, discovered by Kamerlingh Onnes in 1911, continues to be a fascinating subject of condensed matter physics today. Much interest has been devoted to the study of the superconductivity induced in a metal which by itself is not superconducting but is in electrical contact with a superconductor. As the carriers of superconductivity, the Cooper pairs, diffuse across the contact into the metal they remain correlated, although the pairing mechanism is lifted; we call this the proximity effect. The observation of these superconducting correlations has come within the reach of experiments in the last decade. With state-of-the-art fabrication techniques mesoscopic samples have been produced which are small and clean enough for the quantum mechanical coherence of the electrons to be preserved over the sample size. This thesis focuses on the variety of signatures of single-particle physics that appear in the electrical transport and the magnetic screening properties of these systems.

The main contribution of this thesis to the field of mesoscopic superconductivity consists in the study of the thermodynamic properties in the presence of a magnetic induction. We map out the phase diagram of a normal-metal–superconductor (NS) hybrid system in the space spanned by the temperature (T) and the magnetic field (H). The region of the $H - T$ diagram of interest lies well below the transition temperature and the critical field line, i.e. in the Meissner phase, of the superconductor. The involved energy scales are determined by the geometric system size d and the mean free path $l = v_F\tau$ of the normal metal and are given by the single-particle level spacing $\sim \hbar v_F/d$ or the Thouless energy $\sim \hbar v_F l/d^2$, respectively, in ballistic or diffusive systems.

We distinguish two phases in the $H - T$ diagram: a diamagnetic state (at low temperature and field) where the applied field is effectively screened, and a normal state where the magnetic field penetrates into the normal metal. The magnetic breakdown of the Meissner field expulsion occurring at the frontier of the two regimes is interpreted as the critical field of the proximity layer. We give a complete characterization of this first order transition for a ballistic NS structure, determining the spinodals, the magnetization jump, as well as the latent heat, and find a critical point, beyond which the two phases are connected by a continuous cross-over.

We study the magnetic screening in the diamagnetic phase for a NS hybrid layer. We find that the current–field relation is typically non-local in the proximity effect producing a high sensitivity of the diamagnetic susceptibility to the mean free path. We classify the behavior into several regimes between the clean ($l \rightarrow \infty$) and the dirty ($l \rightarrow 0$) limit. The reduction of the screening density and the non-locality range with decreasing purity affect the screening in an opposite way, competing in the diamagnetic susceptibility observed in the experiments.

The screening properties can be traced back to the quasi-particle excitation spectrum in the absence of the field. We thus establish a connection to the transport properties of NS junctions: We explain the resonance structure in the conductance and the shot noise at finite voltage, which appears as a signature of the quantum behavior of the discrete electrons.

Back to the $H - T$ phase diagram: in the field penetration phase, where the screening is negligible, we analyze the geometry of a ballistic SNS Josephson link. We show that the combination of the non-locality and the finite size of the junction produces an anomalous critical-current–flux dependence. As a function of increasing field H we find a cross-over from the usual single to a double flux quantum periodicity.

In the low-temperature low-field corner of the $H - T$ phase diagram we discover a new paramagnetic phase by considering the effect of a repulsive electron–electron interaction in the proximity metal. Quasi-particles are found to be trapped at the NS interface, accumulating to a density of states peak at the Fermi energy. This peak induces a paramagnetic instability towards spontaneous magnetic moments. On top of the Meissner phase we find a first order transition as the moments polarize in the applied field. The hysteresis and the dissipation accompanying a paramagnetic reentrance in the susceptibility provide the characteristic features observed in fascinating experiments on NS cylinders.

Finally, we consider the transport in Josephson junctions with unconventional superconductors, where the current–phase relation exhibits a double frequency. We propose to exploit this π -periodicity for the implementation of a quantum computer.

Zusammenfassung

Supraleitung, in 1911 durch Kamerlingh Onnes entdeckt, ist heute noch ein faszinierendes Gebiet der Festkörperphysik. Die Untersuchung der Supraleitung, welche in einem Metall induziert wird, das selbst nicht supraleitend ist, jedoch im elektrischen Kontakt mit einem Supraleiter steht, hat ein grosses Interesse erfahren. Wenn die Träger der Supraleitung, die Cooper-Paare, durch den Kontakt in das Metall diffundieren, behalten sie ihre Korrelationen, obwohl der Paarungsmechanismus verschwindet. In der letzten Dekade ist die Beobachtung der supraleitenden Korrelationen zwischen einzelnen Quasi-Teilchen in die Reichweite der Experimente gerückt. Die modernsten Fabrikationstechnologien haben die Herstellung von mesoskopischen Systemen ermöglicht, welche klein und sauber genug sind, um die quantenmechanische Phasenkohärenz der Elektronen über die Probengrösse zu gewährleisten. Diese Dissertation widmet sich der Vielfalt der Einteilchen-Physik, welche im elektrischen Transport und der magnetischen Abschirmung in diesen Systemen auftritt.

Der Hauptbeitrag dieser Dissertation zum Feld der mesoskopischen Supraleitung besteht im Studium der thermodynamischen Eigenschaften unter dem Einfluss einer magnetischen Induktion. Wir bestimmen für eine Metall-Supraleiter (NS) Hybridstruktur das Verhalten im Phasendiagramm, welches durch die Temperatur (T) und das Magnetfeld (H) aufgespannt wird. Der untersuchte Bereich im $H - T$ Diagramm liegt deutlich unter der Übergangstemperatur des Supraleiters sowie der kritischen-Feld-Grenze. Die geometrische Masse d und die freie Weglänge $l = v_F \tau$ bestimmen die typische Energieskala im Problem: die Einteilchen-Energie $\sim \hbar v_F / d$ beziehungsweise die Thouless-Energie $\sim \hbar v_F l / d^2$ in ballistischen oder diffusiven Systemen.

Wir unterscheiden zwei Phasen im $H - T$ Diagramm: einen diamagnetischen Zustand (bei kleinen Temperaturen und Feldern), der sich durch die Abschirmung der angelegten Felder auszeichnet, und einen normalleitenden Zustand, wo das Magnetfeld ungehindert in das Metall eindringt. Wir bestimmen das kritische Feld, das die beiden Phasen trennt, und charakterisieren diesen Übergang erster Ordnung in einem ballistischen NS Schichtsystem durch die Spinodalen, den Sprung in der Magnetisierung sowie die latente Wärme. Wir finden, dass die Phasengrenze oberhalb eines kritischen Punktes verschwindet.

In der Beschreibung der diamagnetischen Phase finden wir eine für die induzierte Supraleitung typische nicht-lokale Strom–Feld Relation, welche die diamagnetische Suszeptibilität zu einem feinen Indikator der freien Weglänge macht. Wir unterscheiden mehrere Verhalten zwischen dem reinen ($l \rightarrow \infty$) und dem schmutzigen ($l \rightarrow 0$) Grenzfall. Mit abnehmender Reinheit haben die Reduktion der abschirmenden Dichte sowie der Reichweite der Strom–Feld Relation eine entgegengesetzte Wirkung auf die Abschirmung und stehen daher im Wettbewerb in der experimentell gemessenen diamagnetischen Suszeptibilität.

Das Abschirmverhalten kann auch auf das Quasiteilchen-Spektrum zurückgeführt werden. Dies ergibt eine Verbindung zu den Transport-Eigenschaften in NS Strukturen: Wir untersuchen die Resonanzen im Leitwert und finden sie wieder in den quantenmechanischen Stromfluktuationen aufgrund der Diskretheit der Elektronenladung.

In der normalleitenden Phase, wo die Abschirmung vernachlässigt werden kann, untersuchen wir die Anordnung eines ballistischen SNS Josephson Kontaktes. Wir zeigen, dass die Verbindung von Nichtlokalität und der endlichen Ausdehnung des Metalls zu einer anomalen Abhängigkeit des kritischen Stromes vom magnetischen Fluss führt. Mit zunehmendem Feld finden wir einen Übergang von der einfachen Periode eines Fluss-Quantums zur doppelten.

Wir entdecken die Existenz einer neuen paramagnetischen Phase, welche durch eine repulsive Elektron-Elektron Wechselwirkung verursacht wird, in der Nähe des Ursprungs des $H - T$ Phasendiagramms. Quasiteilchen werden an der NS Grenzfläche festgehalten und tragen zu einer Spitze in der Zustandsdichte bei der Fermi-Energie bei. Diese verursacht eine paramagnetische Instabilität, welche spontane magnetische Momente hervorbringt. Dem diamagnetischen Verhalten überlagert finden wir das die Polarisation der magnetischen Momente zu einem Phasenübergang erster Ordnung bei Feld Null führt. Die Hysterese und Dissipation, welche das paramagnetische Signal in der Suszeptibilität begleiten, sind in qualitativer Übereinstimmung mit bisher noch unerklärten Experimenten auf mesoskopischen Zylindern.

Schliesslich betrachten wir den Transport in Josephson Kontakten mit unkonventionellen Supraleitern, wo eine doppelte Josephson-Frequenz auftritt. Wir schlagen vor, diese π -Periodizität in der Phase zur Implementation eines Quanten-Computers zu benutzen.

Chapter 1

Introduction

In this thesis we study the behavior of electrons in a metal which is in electrical contact with a superconductor. The superconductor (S) can be viewed as a reservoir where due to an effective attraction the electrons condense into Cooper pairs, while the normal metal (N) is idealized as a gas of free electrons. Through the diffusion across the NS contact the metallic electrons acquire superconducting correlations; we call this the proximity effect.

The Cooper pairs are essentially described by one wavefunction (the order parameter of the superconductor) producing quantum behavior on a macroscopic scale. The quantum interference effects between the free electrons instead rely on the coherence of the single-particle wavefunctions and are much more fragile. The observable quantum phenomena are limited to the mesoscopic scale given by the phase coherence length here. The proximity effect offers an experimental access to the coherent single-particle physics by combining it with the macroscopic superconducting correlations.

Here we study the electrical transport and the orbital magnetism of electrons in normal-metal – superconductor hybrid structures. Our theoretical work is motivated by an intense experimental activity in this area of mesoscopic physics triggered by recent advances in nanostructure fabrication technology. For an introduction to the subject we refer the reader to the review on “Mesoscopic Electron Transport” [Kouwenhoven 1997].

The microscopic process underlying the physics of proximity induced superconductivity is the Andreev reflection (AR) at a NS interface: An electron incident from the normal metal into the superconductor is retro-reflected into a hole, transmitting the double electron charge into the superconductor [Andreev 1964]. In the following, we give an introduction to the basic properties of the AR and relate the works of this thesis to this fundamental process.

The quasi-particle transfer at a NS interface is best described by the Bogoliubov-de-Gennes (BdG) equations [de Gennes 1966a], which determine the two-component wavefunctions Φ of electron and hole close to the Fermi level,

$$\begin{pmatrix} h_0 - \mu & \Delta \\ \Delta^* & -h_0^* + \mu \end{pmatrix} \begin{pmatrix} u \\ v \end{pmatrix} = \epsilon \begin{pmatrix} u \\ v \end{pmatrix}, \quad \Phi = \begin{pmatrix} u \\ v \end{pmatrix} e^{i\mathbf{k}_F \mathbf{x}}. \quad (1.1)$$

We use the linearized Hamiltonian $h_0 - \mu = -i\hbar v_F \nabla$, where $v_F = \hbar k_F/m$ is the Fermi velocity, Δ provides the off-diagonal pair-potential and ϵ is the quasi-particle energy with respect to the chemical potential. Let us consider a NS junction as described by the pair potential

$$\Delta(x) = \begin{cases} 0, & x < 0 & (N), \\ \Delta_0 e^{i\varphi} & x > 0 & (S). \end{cases} \quad (1.2)$$

While in the normal metal the electron and hole states decouple ,

$$\Phi_+ = \begin{pmatrix} 1 \\ 0 \end{pmatrix} e^{ik_+x}, \quad \Phi_- = \begin{pmatrix} 0 \\ 1 \end{pmatrix} e^{ik_-x} \quad (1.3)$$

($k_{\pm} = k_x \pm \epsilon/\hbar v_x$, $\hbar k_x/m = v_x = v_F \cos \vartheta$), the quasi-particles in the superconductor are coupled evanescent modes,

$$\Phi_e = \begin{pmatrix} 1 \\ \gamma e^{-i\varphi} \end{pmatrix} e^{ik_e x}, \quad \Phi_h = \begin{pmatrix} \gamma e^{i\varphi} \\ 1 \end{pmatrix} e^{ik_h x} \quad (1.4)$$

($\gamma = \exp[-i \arccos(\epsilon/\Delta)]$, $k_{e,h} = k_x \pm i\sqrt{\Delta_0^2 - \epsilon^2}/\hbar v_x$, $\epsilon < \Delta$). By using the ansatz $\Phi_+ + r_A \Phi_-$ for $x < 0$ and Φ_e for $x > 0$ we easily find the Andreev reflection amplitude from the continuity of the wavefunction,

$$r_A = \gamma e^{-i\varphi} = \exp(-i \arccos \frac{\epsilon}{\Delta}) e^{-i\varphi}. \quad (1.5)$$

For $\epsilon < \Delta$, the incident quasi-particle excitation is reflected with probability $|r_A| = 1$. Similarly the Andreev amplitude describing the conversion of an incident hole to a reflected electron is given by $\gamma \exp(i\varphi)$. Andreev thus found that the incident quasi-particle excitation is prevented from entering the superconductor, and consequently heat (or energy) transport across the NS interface is suppressed [Andreev 1965]. On the other hand, the double charge $2e$ (of incident electron and reflected hole) is transferred across the NS interface. In the superconductor the decaying quasi-particle current is converted into supercurrent [Blonder 1982].

The Andreev reflection (AR) coherently couples electron and hole states and thus induces the superconducting correlations $F(x)$ in the normal metal,

$$F(x) = \langle \hat{\Psi}_{\downarrow}(x) \hat{\Psi}_{\uparrow}(x) \rangle = \sum_{\alpha} u_{\alpha}(x) v_{\alpha}^*(x) f(\epsilon_{\alpha}), \quad (1.6)$$

where the index α denotes the eigenstates and $f(\epsilon)$ is the Fermi occupation number, see also appendix A. Instead of a Cooper pair condensate, the proximity metal exhibits correlated electron-hole pairs, which are mutually independent. Here lies the fragility of the proximity effect: The thermally excited Andreev pairs at energy $\epsilon \sim T$ are dephased over the thermal length $\xi_N(T) = \hbar v_F/2\pi T$ and the correlation function (1.6) is suppressed as $\sim \exp[-x/\xi_N(T)]$ (see Chp. 3.2).

Let us consider in the following a normal metal slab of thickness d on top of a bulk superconductor. Due to the AR process, the quasi-particles at subgap energies $\epsilon < \Delta$ are bound to the normal layer, see Fig. 1.1. The discrete energies of the Andreev bound states follow from a constructive interference condition for an electron and a hole traveling back and forth across the normal layer and being converted into each other at the NS interface ($n = 0, 1, \dots$),

$$2k_+d - 2k_-d - 2 \arccos \frac{\epsilon}{\Delta} = 2n\pi, \quad (1.7)$$

$$\epsilon_n(v_x) = \frac{\hbar v_x}{2d} (n\pi + \arccos \frac{\epsilon}{\Delta}) \stackrel{\epsilon \ll \Delta}{\approx} \frac{\hbar v_x \pi}{2d} (n + \frac{1}{2}). \quad (1.8)$$

The bound states are quantized at energies $\sim \hbar v_x/d$ depending only on the component of the Fermi velocity in forward direction ($v_x = v_F \cos \vartheta$). The energy levels are repelled from the chemical potential, as a finite energy mismatch of the wave vector k_{\pm} of electron and hole is needed to compensate for the phase $\arccos(\epsilon/\Delta) \approx \pi/2$ of the AR. The discrete Andreev levels contribute to the finite density of states at $\epsilon < \Delta$ filling the superconducting gap.

The transport through the ballistic NS structure coupled by means of a tunneling barrier (I) to a NINS junction, see Fig. 1.1, reveals a resonance structure at the energies of the Andreev (quasi)-bound states $\epsilon \sim \hbar v_F/d$ [Rowell 1966]. A similar behavior is expected in a diffusive system, where the average path traveled d is to be replaced by d^2/l (l mean free path). According to the constructive interference condition $\epsilon d^2/\hbar v_F l \sim (2n+1)\pi$ the resonances are found at the Thouless energy $E_c \sim \hbar v_F l/d^2$. In chapter 2 we analyze the spectral conductance $G(\epsilon)$ and the shot noise $S(\epsilon)$ in NS junctions with an arbitrary scattering region in the normal lead, which typically includes a barrier at the NS interface and additional disorder in the normal lead. We describe the single-particle resonance structure that follows from the interplay between the normal scattering and the AR processes and enhances the subgap transport.

The linear transport coefficients $G(0)$ and $S(0)$ in a NS junction are suppressed by the transmission T^2 of the N conductor, reflecting the two-particle nature of the AR process [Blonder 1982, Beenakker 1992a, de Jong 1994]. This explains why the first observation of an enhanced subgap conductance could be misinterpreted as being due to supercurrents [Kastalsky 1991]. Actually, the iterative scattering

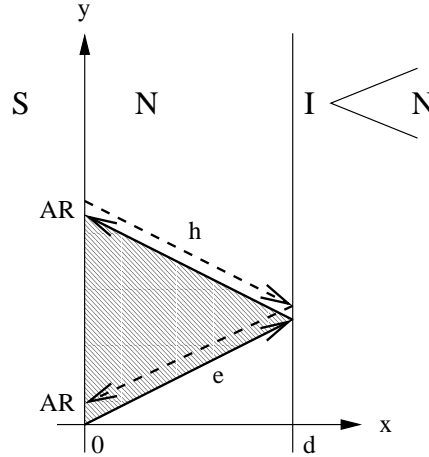


Figure 1.1: Trajectories of electron-hole Andreev levels in a proximity normal-metal layer: electron and hole travel back and forth and are converted into each other by the Andreev reflection (AR). Top: Coupling of the NS slab by a tunnel contact to a NINS junction.

processes between the disorder and the *interface barrier* increase the possibility for an AR as compared to a simple tunneling junction [Melsen 1994]. If, on the other hand, the interface barrier is weak, the resonance structure of the Andreev states, which are el-hole quasi-bound states between the disorder and the *superconductor*, determine the transport coefficients. The conductance $G(\epsilon)$ as well as the shot noise $S(\epsilon)$ exhibit peaks at the Andreev or the Thouless energy, respectively, for a ballistic or a diffusive conductor. Characteristically these resonances are pinned at a finite energy above the Fermi level, which we understand in terms of the $\pi/2$ phase shift in the AR process, and survive in the multichannel limit. The reentrance effect observed in NS junctions with a diffusive lead [Petrashov 1995, Charlat 1996, Poirier 1997a] reflect the non-monotonicity of the spectral conductance due to the underlying Andreev resonances. While theoretical works using the Green's function technique have explained these experiments accurately [Yip 1995, Nazarov 1996, Stoof 1996, Golubov 1997, Wilhelm 1998], the Landauer-Büttiker approach offers an intuitive understanding here, based on a ballistic viewpoint. The diffusive system is described by averaging over an ensemble of impurity configurations, see [Marmokos 1993, Argaman 1997, Lambert 1998]. In Chp. 2 we present new results for the shot noise, which are of interest with respect to ongoing noise experiments in NS junctions [Jehl 1999, Kozhevnikov 1999].

The quantization of the Andreev levels at discrete energies away from the Fermi level suppresses the density of states (DOS) of the proximity layer as compared to

the bulk metal. From the low energy spectrum (1.8) we obtain the Andreev DOS [de Gennes 1963]

$$N(E) = \frac{1}{d} \int \frac{dk_y dk_z}{2\pi^2} \delta[E - \epsilon_0(v_x)] \quad (1.9)$$

$$\sim N_0 \frac{\epsilon d}{\hbar v_F} \quad (1.10)$$

($v_x = \hbar \sqrt{k_F^2 - k_y^2 - k_z^2}/m$, $N_0 = mk_F/\hbar^2\pi^2$). The excitation gap Δ is softened in the normal metal to a linearly vanishing DOS below $\hbar v_F/d$. We note that similar results for the DOS are observed in diffusive NS hybrid structures [Guéron 1996, Belzig 1996b].

The DOS suppression close to the Fermi level affects the response properties of the proximity layer. In chapter 3 we consider the magnetic response, i.e., the screening currents induced by an applied magnetic field. Generically, the linear current response $j = j_{\text{dia}} + j_{\text{para}}$ is given by the sum of the diamagnetic current describing the response of the rigid wavefunction and the paramagnetic current induced by the perturbation of the wavefunction in the applied field. While the diamagnetic current is trivially proportional to the bulk electron density, the paramagnetic current depends on the DOS at the Fermi surface [Schrieffer 1988]. The solution of the screening problem requires the full knowledge of the dispersive relation $j(q) = -(c/\lambda^2)K(q)A(q)$ which has to be solved together with the Maxwell equation $j(q) = q^2 A(q)$. ($\lambda = (4\pi n e^2/mc^2)^{-1/2}$ is the London penetration depth). The variation of the field on wavelength $1/q$ typically induces quasi-particle excitations at energy $E \sim \hbar q v_F$ giving a paramagnetic current. Depending on the availability of the finite energy excitations, the paramagnetic current either vanishes or compensates for the diamagnetic current.

In a BCS superconductor with excitation gap Δ , the paramagnetic current is gapped (the DOS vanishes) for long wavelength and the response is purely diamagnetic, $K(q) \sim 1$ for $\hbar q v_F < \Delta$. Above the gap the paramagnetic current is found to cancel the diamagnetic current leaving a small response $K(q) \sim \Delta/\hbar q v_F$. In real space this implies a range of the current-field relations of the order of $\xi_0 \sim \hbar v_F/\Delta$. For a London length $\lambda > \xi_0$ we find a local response, while for $\lambda < \xi_0$ the current-field dependence is nonlocal according to a Pippard-type relation [Pippard 1953]. In a bulk normal metal, the continuous density of states at the Fermi level implies a cancellation of dia- and paramagnetic currents, leaving no net screening response.

In a clean proximity layer, the suppression of the DOS produces a net diamagnetic current, but the lack of a quasi-particle gap translates to a diverging nonlocality range. It turns out that for finite q the paramagnetic current is able to compensate the diamagnetic current, producing the kernel $K(q) \sim \delta(q)$, and thus the nonlocal

current functional [Zaikin 1982]

$$j(x) \sim -\frac{c}{\lambda^2 d} \int_0^d dx' A(x'). \quad (1.11)$$

We study this screening problem in more detail in Chp. 3, where the magnetic response of a NS slab with arbitrary impurity concentration is discussed. We introduce the powerful quasi-classical Green's function technique to derive the general linear current functional. We find that a finite mean free path provides a cutoff for the nonlocality range, but that the current-field relations in the proximity effect nevertheless remain typically nonlocal. We distinguish several regimes for the magnetic response depending on the geometric thickness d , the thermal length $\xi_N(T)$ and the mean free path l . The reduction of the screening density and the nonlocality range with decreasing purity affect the susceptibility in different ways, producing a non-monotonic dependence in the diamagnetic susceptibility with changing mean free path. This understanding provides the basis for a quantitative fit with the experiments [Müller-Allinger 1999].

The nonlocal field dependence is also found in the spectrum of the Andreev states. Replacing the gradient in (1.1) by $\nabla + ie\mathbf{A}(x)/\hbar c$ we can account for the vector potential by adding an Aharonov-Bohm-type phase to the constructive interference condition (1.7), yielding the bound state energies

$$\epsilon_n = \frac{\hbar v_x}{4d} \left[(2n+1)\pi - \frac{2\pi}{\Phi_0} \oint \mathbf{A} d\mathbf{x} \right]. \quad (1.12)$$

The circular integral gives the flux $\Phi = \oint \mathbf{A} d\mathbf{x}$ enclosed between the quasi-classical trajectory and the NS interface, see Fig. 1.1 (hatched region). The flux enters modulo an integer number of flux quanta $\Phi_0 = hc/2e$. This leads to a random distribution of the Andreev levels at large field $\Phi \gg \Phi_0$, suppressing the energy gap and inducing the magnetic breakdown in the proximity layer. The magnetic breakdown denotes the proximity layer's own critical field H_b , at which the Meissner field expulsion ceases to be effective and the applied field penetrates into the normal layer by a first order transition. While in a small applied magnetic field the Andreev pairs produce diamagnetic screening currents, at large fields the superconducting correlations are destroyed by the random Aharonov-Bohm phases in (1.12) and the net screening current vanishes. In Chp. 4 we determine the $H - T$ phase diagram for this behavior, finding the first order transition line separating the diamagnetic phase of effective field expulsion and the normal state of field penetration.

The magnetic breakdown has been observed recently in increasingly clean samples [Oda 1980, Mota 1982, Bergmann 1987, Visani 1990b] and we find good agreement of both temperature and thickness dependence of the breakdown field with ex-

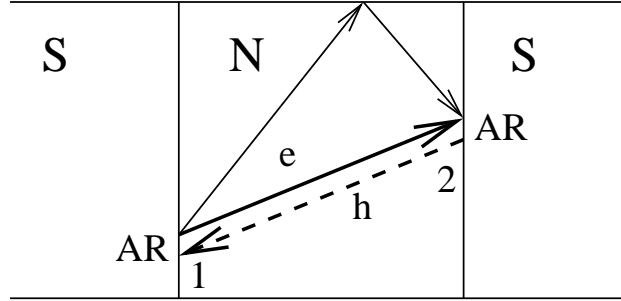


Figure 1.2: Trajectories of electron-hole Andreev levels in a normal-metal – superconductor – normal metal (SNS) junction. Note the existence of trajectories reflecting at the metal boundary.

perimental data on quasi-ballistic Ag-Nb samples [Mota 1989, Müller-Allinger 1999].

We study a different aspect of nonlocality in Chp. 6, where we consider a ballistic normal metal layer connected by two superconducting reservoirs to a SNS junction. The two NS interfaces act as a confining potential for the electrons and holes in the normal interlayer. The junction exhibits current-carrying bound states consisting of an electron traveling forward and a hole traveling backwards which are converted into each other by the AR [Kulik 1970], see Fig. 1.2. The constructive interference condition,

$$(k_+ - k_-)d \mp \Delta\varphi = (2n + 1)\pi, \quad (1.13)$$

now features the phase difference $\Delta\varphi$ of the two superconducting reservoirs (the sign of $\Delta\varphi$ depending on the orientation of the quasi-particle current) and implies the spectrum of bound states

$$\epsilon_n(v_x) = \frac{\hbar v_x}{d} \left(n\pi + \frac{\pi}{2} \pm \Delta\varphi \right). \quad (1.14)$$

These bound states are known to transmit the supercurrent between the two reservoirs: While at phase difference $\Delta\varphi = 0$ the left- and right-going states are degenerate and their respective currents cancel, by changing $\Delta\varphi$ an asymmetry is introduced producing the supercurrents in the junction.

Including a magnetic induction as above, the bound state energies

$$\epsilon_n = \frac{\hbar v_x}{d} \left[n\pi + \frac{\pi}{2} \pm \underbrace{\left(\Delta\varphi - \frac{2\pi}{\Phi_0} \int_1^2 \mathbf{A} \, d\mathbf{x} \right)}_{\gamma} \right], \quad (1.15)$$

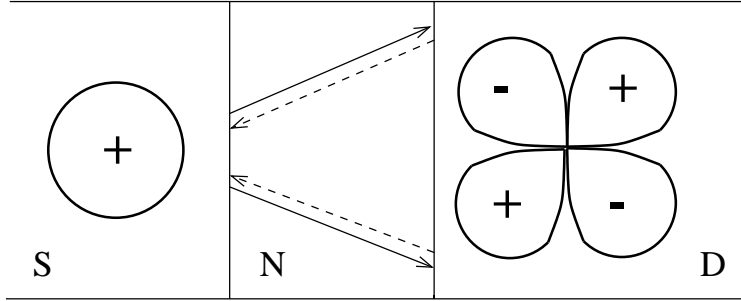


Figure 1.3: Trajectories of representatives from two Andreev level populations shifted by a phase difference π .

depend on the gauge invariant phase difference (γ) between the two endpoints 1 and 2 of the quasiparticle trajectories connecting the superconducting reservoirs, see Fig. 1.2. The currents $j \propto \partial E / \partial \gamma$ depend non-locally on the field $\mathbf{A}(\mathbf{x})$. The Josephson current through the junction is given by the sum of the currents carried along all the quasi-particle trajectories across the junction. In Chp. 6 we find that in a junction of finite width the trajectories with multiple reflections at the metallic boundary alter the field dependence of the Josephson current, as they experience a different gauge invariant phase difference, see Fig. 1.2. The current–flux relation $I = I(\Phi)$ crosses over from the usual Φ_0 - to the anomalous $2\Phi_0$ -periodicity as a function of increasing field. The cross-over takes place when the Josephson vortex distance $a_0 = \Phi_0 / Hd$ becomes smaller than the nonlocality range of the junction. Our results explain the experimental data recently obtain on S-2DEG-S junctions [Heida 1998], where the ballistic link was provided by a two-dimensional electron gas (2DEG).

Let us consider the Josephson relation $I = I(\Delta\varphi)$ in a junction between a conventional, S-wave superconductor (S) and a High- T_c superconductor with D-wave symmetry (D). The order parameter in the D-wave superconductor is direction-dependent as $\sin 2\vartheta$ exhibiting two lobes with positive sign and two lobes with negative sign, see Fig. 1.3. The phase difference $\Delta\varphi$ across the SND junction thus depends on the orientation of the quasi-particle trajectory, varying by π for trajectories connecting with the negative rather than the positive lobes of the D-wave material. For the alignment of the D-wave superconductor with a gap $\Delta \propto \sin 2\vartheta$ with respect to the x -axis, the two quasiparticle populations with $\vartheta > 0$ and $\vartheta < 0$, see Fig. 1.3, correspond to two conventional Josephson junctions shifted by π with respect to each other. The spectrum of the bound states is given by Eq. (1.13), where $\Delta\varphi$ differs by π for the two quasi-particle populations. Therefore, the 2π periodicity of the critical current of each junction is reduced to a π periodicity in

the SND junction.

In chapter 7 we propose to exploit the doubly periodic Josephson relation for the implementation of a quantum bit (qubit). The π -periodic junction can be viewed as a macroscopic two-level system exhibiting two degenerate ground states which carry no current and are thus optimally isolated from the environment. The macroscopic quantum tunneling between these two states opens the possibility for a quantum time evolution of the junction, which we propose to use for quantum computation.

In chapter 5 we return to the orbital magnetism, synthesizing various elements of proximity induced superconductivity discussed above. The motivation for this work has been provided by the puzzling low-temperature anomalies observed in normal-metal – superconductor cylinders by Mota and co-workers [Visani 1990a, Mota 1994]. In the low-temperature low-field corner of the H-T phase diagram, the Ag-Nb and Cu-Nb samples develop a paramagnetic signal on top of the saturated Meissner response, which produces a reentrance in the magnetic susceptibility (for a detailed discussion of the experiments see also [Visani 1990c, Frassanito 1996]). We note that the observed behavior is not believed to be related to the low-temperature reentrance in the conductance of a disordered NS junction discussed above, which is due to the finite energy properties entering the non-equilibrium transport. The magnetic response instead is a thermodynamic property of the system.

In chapter 5 we consider the consequence of a repulsive electron-electron interaction in the normal metal proximity layer. The repulsive coupling $V_N > 0$ induces a finite gap $\Delta(x) = V_N F(x)$ in the normal layer which is proportional to the induced superconducting correlations (1.6). The order parameter changes sign across the NS interface as the coupling constant changes from attractive to repulsive. The NS structure behaves like a Josephson junction with a phase difference of π across the NS interface. We know from Eq. (1.13) that a junction with $\Delta\varphi = \pi$ traps density of states at the Fermi energy $\epsilon = 0$, according to

$$(k_+ - k_-)L = 2n\pi, \quad (1.16)$$

which remains true in the limit of a vanishing junction length $L \rightarrow 0$. The phase difference π across the junction cancels the phase shifts $\pi/2$ of the two AR. As all transverse wavefunction (k_y, k_z) exhibit a zero energy bound state, the DOS shows a peak a zero energy with macroscopic weight

$$N(E) \sim N_0 k_F^2 \delta(E), \quad (1.17)$$

per unit surface.

As we show in Chp. 5, this peak implies a paramagnetic instability in the current response and leads to a spontaneous onset of currents along the interface. Spontaneous moments form at the NS interface producing a low-temperature reentrance

in the magnetic susceptibility. The qualitative agreement of our results with the observed low-temperature anomaly is indicative of a repulsive electron-electron interaction in these systems.

Chapter 2

Nonlinearity in normal-metal – superconductor transport: Conductance and shot noise

2.1 Scattering matrix approach to normal-metal – superconductor transport

2.1.1 Introduction

The study of electronic transport in normal-metal–superconductor (NS) or semiconductor–superconductor (SmS) sandwiches has attracted a considerable amount of interest in the past years. At sufficiently low temperature and in high quality mesoscopic samples, the phase-breaking length of the electrons is larger than the typical system size, resulting in directly observable quantum coherence effects. Of special interest is the effect of the electronic phase-coherence in a normal metal–superconductor system. In the standard theory of the proximity effect, the influence of the superconductor on the normal metal can be understood in terms of the coherent coupling of electrons and holes in the metal as described by the Bogoliubov-de Gennes (BdG) equations [de Gennes 1966a]. The correlation between electrons and holes is produced by the process of Andreev reflection [Andreev 1964, Blonder 1982] at the NS interface, by which an incident electron is back-reflected into a hole, converting quasiparticle current to supercurrent. This microscopic picture of electron-hole correlation is equivalent to that provided by a pair correlation function in the normal metal, which is induced by the superconductor through the contact at the NS interface. The scattering matrix approach makes use of the microscopic single particle picture of coupled electron and hole channels providing a straightforward tool within a formalism of the Landauer–Büttiker type [Landauer 1970, Büttiker 1985,

Beenakker 1992a].

The quality of the interface as well as the phase breaking processes determine the strength of the proximity effect and naturally have their impact on the current–voltage characteristics (CVC). A few fascinating transport experiments [Pothier 1994, Petrashov 1995, Courtois 1996] have been carried out recently, investigating temperature and voltage dependence, as well as the flux modulation, of both NS and SmS junctions. Interestingly, the relative strength of the interface barrier and the elastic scattering in the normal region is crucial for the features of the CVC. The ratio of the two determines whether subgap conductance peaks arise at zero or finite voltage [Volkov 1993, Marmokos 1993, Yip 1995]. The investigation of these so-called zero and finite bias anomalies in the subgap conductance have been the object of recent experiments [Kastalsky 1991, Nguyen 1992, Nitta 1994, Bakker 1994, Magnée 1994, Poirier 1997a]. The present work draws much of its motivation from the ongoing discussions and experiments in this area, see also [Aleiner 1996]. In our case study of a double barrier NINIS junction we observe zero and finite bias anomalies and shed light on the underlying mechanism.

Recently in [Nazarov 1996, Stoof 1996] as well as [Golubov 1997], the carrier transport in disordered NS junctions has been described in terms of an energy-dependent diffusion constant, successfully explaining the recent experiments on reentrance in the conductivity at low temperatures [Petrashov 1995, Charlat 1996]. Their work uses the quasi-classical Green’s functions technique [Rammer 1986], which allows to describe transport both close to equilibrium [Hekking 1994] and far away from equilibrium [Volkov 1993, Volkov 1994, Zhou 1995] and facilitates the averaging over disorder in diffusive conductors. This approach is quite indispensable if phase-breaking processes are to be included. An appealing alternative approach is the scattering matrix technique, which relies on the quasiparticle wavefunctions described by the BdG equations. While being valid in a general context, it describes the transport in mesoscopic systems from the intuitive ballistic point of view. The transport through normal or superconducting leads is expressed through the properties of a multichannel scattering matrix accounting for all elastic scattering processes, whether they be due to a geometric constriction, single impurities, or disorder (inelastic processes are excluded from such a description). By these means, the transport problem is reduced to solving a ballistic problem at the interfaces of the normal and superconducting leads. The current and the conductance of the system are determined analytically in terms of the transmission and reflection amplitudes of the scattering matrix. Adhering to this formalism rather than the Green’s function technique helps us to improve our understanding of zero and finite bias anomalies.

The study of normal–superconducting junctions goes back to the works of Kulik [Kulik 1970] on SNS junctions and of Blonder et al. [Blonder 1982] on NIS junctions, who studied nonlinear transport within the framework of the BdG equations considering quasi one-dimensional models. On the other hand, the scattering matrix tech-

nique was developed by Landauer and co-workers [Landauer 1970, Büttiker 1985] in the linear response regime, resulting in the well known conductance formula for a normal metal. Lambert [Lambert 1991] and Takane and Ebisawa [Takane 1991, Takane 1992] extended the approach to include superconducting segments, on the basis of which Beenakker [Beenakker 1992a] derived a zero temperature, linear response conductance formula for the transport through NS junctions. A few studies have been carried out recently [Marmokos 1993, Brouwer 1995, Claughton 1996] combining the scattering matrix approach with the finite voltage transport model of Ref. [Blonder 1982]. They have limited themselves to the energy dependence of the scattering states to extract finite voltage properties of the CVC in the subgap regime. Here, we extend these works to voltages above the gap and additionally take into account the full voltage dependence of the transport problem. This is important within the context of the sign reversal symmetry of the differential conductance which we discuss below. At the same time, we provide a common framework for the above studies, tracing them back to a single general formula.

In the present chapter, we derive the general expression for the current through a NS junction in the scattering matrix approach, valid for multiple channels, finite voltage, and nonzero temperature. We review the derivation of the current–voltage relation and express it in terms of a *spectral* conductance formula, thereby accounting for the full voltage dependence of the transport problem. The reflection at the NS interface is made explicit using the Andreev approximation and a conductance formula is obtained expressing the result in terms of the normal scattering matrix. We illustrate this formula in the new regime of voltages above the gap and expose its connection to previously obtained limits. We describe the existence of resonances due to quasi-bound Andreev states, and show that they produce sharp conductance peaks in both the single and multichannel junction. We explain the generic mechanism underlying the appearance of zero and finite bias anomalies in the ballistic two barrier system. Finally, we interpret our results in connection to the recent experiments on zero and finite bias anomalies in disordered NS junctions.

Chapter 2.1 closely follows our paper published in [Lesovik 1997]. We would like to point out further works, both theoretical and experimental, which have been carried out since then [Hartog 1997, Lambert 1998, Wilhelm 1998, Lesovik 1998].

We consider a normal–superconducting junction with quasi one-dimensional, ballistic normal and superconducting leads, as shown in Figure 2.1. The pair potential vanishes in the normal part, due to the absence of electron-electron interactions. Between the normal lead and the NS interface, the electrons traverse a disordered region, the transmission through and the reflection thereof are described by a scattering matrix. Between the scattering region and the NS interface, a small ballistic normal region serves to separate the scattering in the normal part, which mixes all electron channels at a given energy, from the scattering at the NS interface, where

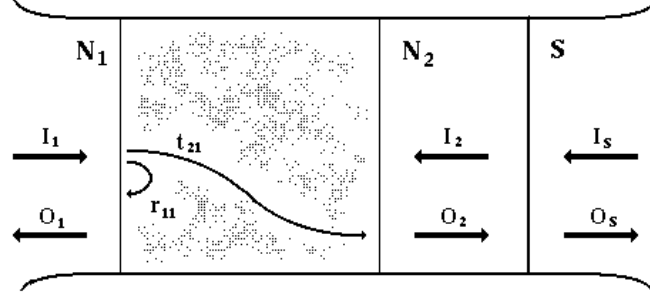


Figure 2.1: Schematic structure of a disordered NS junction. Ballistic normal (N_1 , N_2) and superconducting leads (S) are coupled to reservoirs at chemical potential $\mu - eV$ and μ , respectively. Scattering is limited to the hatched region between leads N_1 and N_2 .

electron and hole channels are mixed in the reflection process. The coherent scattering in the disorder region of the normal metal is described by the $4N \times 4N$ scattering matrix,

$$\begin{aligned}
 \begin{pmatrix} O_1^e \\ O_1^h \\ O_2^e \\ O_2^h \end{pmatrix} &= \begin{pmatrix} r_{11}(\epsilon) & 0 & t_{12}(\epsilon) & 0 \\ 0 & r_{11}^*(-\epsilon) & 0 & t_{12}^*(-\epsilon) \\ t_{21}(\epsilon) & 0 & r_{22}(\epsilon) & 0 \\ 0 & t_{21}^*(-\epsilon) & 0 & r_{22}^*(-\epsilon) \end{pmatrix} \begin{pmatrix} I_1^e \\ I_1^h \\ I_2^e \\ I_2^h \end{pmatrix} \\
 &= \begin{pmatrix} \hat{r}_{11}(\epsilon) & \hat{t}_{12}(\epsilon) \\ \hat{t}_{21}(\epsilon) & \hat{r}_{22}(\epsilon) \end{pmatrix} \begin{pmatrix} I_1^e \\ I_1^h \\ I_2^e \\ I_2^h \end{pmatrix}, \tag{2.1}
 \end{aligned}$$

which we denote by \mathbf{S}_N . The matrix connects the incoming N electron (hole) channels I_i^e (I_i^h) on each side to the equal energy outgoing channels O_i^e (O_i^h) according to Figure 2.1 ($i = 1, 2$). The N channels represent the different transverse states, r_{ii} and t_{ij} are $N \times N$ reflection and transmission matrices for electron channels, \hat{r}_{ii} and \hat{t}_{ij} the comprehensive $2N \times 2N$ matrices including the complex conjugated reflection and transmission amplitudes for holes¹. Following usual convention, we include the propagation in the ballistic region N_2 in the scattering matrix. For states normalized to carry unit probability current [Blonder 1982], the continuity equation implies the unitarity of the scattering matrix. By allowing for a dependence of the scattering matrices on voltage we can account for the full voltage dependence of the scattering problem. We can thus describe the deformation of the states due to the

¹We denote the complex conjugate of a matrix m by m^* , the transposed matrix by m^\top and the adjoint by m^\dagger .

space dependent potential including, e.g., the voltage dependent Schottky barrier at a semiconductor–superconductor (SmS) interface.

We define an analogous unitary scattering matrix for the NS interface \mathbf{S}_I (see Fig. 2.1) by

$$\begin{pmatrix} I_2^e \\ I_2^h \\ O_S^e \\ O_S^h \end{pmatrix} = \begin{pmatrix} \hat{r}_I(\epsilon) & \hat{t}'_I(\epsilon) \\ \hat{t}_I(\epsilon) & \hat{r}'_I(\epsilon) \end{pmatrix} \begin{pmatrix} O_2^e \\ O_2^h \\ I_S^e \\ I_S^h \end{pmatrix}. \quad (2.2)$$

The $2N \times 2N$ matrices $\hat{r}_I, \hat{r}'_I, \hat{t}_I, \hat{t}'_I$ give the reflection and transmission amplitudes of the states normalized to unit probability current in the normal and superconducting lead². In the evaluation of the current, we will consider the matrix (2.1) to be specified by an arbitrary model for the disorder, while the matrix (2.2) will be made explicit below using the BdG equations. The total effect of all scattering processes in the disorder region and at the NS interface can be described by a unitary, global $4N \times 4N$ scattering matrix. We restrict ourselves to its sub-matrix \hat{r} describing the reflection into the normal region,

$$\begin{pmatrix} O_1^e \\ O_1^h \end{pmatrix} = \hat{r}(\epsilon, V) \begin{pmatrix} I_1^e \\ I_1^h \end{pmatrix} = \begin{pmatrix} r_{ee}(\epsilon, V) & r_{eh}(\epsilon, V) \\ r_{he}(\epsilon, V) & r_{hh}(\epsilon, V) \end{pmatrix} \begin{pmatrix} I_1^e \\ I_1^h \end{pmatrix}. \quad (2.3)$$

r_{ee}, r_{eh}, r_{he} , and r_{hh} are again $N \times N$ reflection matrices. $\hat{r}(\epsilon, V)$ can be expressed through the given scattering matrices (2.1) and (2.2),

$$\hat{r}(\epsilon, V) = \hat{r}_{11}(\epsilon) + \hat{t}_{12}(\epsilon) [1 - \hat{r}_I(\epsilon) \hat{r}_{22}(\epsilon)]^{-1} \hat{r}_I(\epsilon) \hat{t}_{21}(\epsilon), \quad (2.4)$$

representing the sum over all scattering paths of an incident electron or hole excitation, multiply scattered between the disorder region and the NS interface. Apart from the direct reflection at the disorder region, the simplest process contributing consists of an excitation, which is first transmitted (\hat{t}_{21}) through the disorder region, reflected (\hat{r}_I) at the NS interface, and transmitted (\hat{t}_{12}) back to the normal lead. All further paths result from iterative scattering processes between the disorder region and the NS interface.

We now derive the current in the normal lead, expressing it through the global reflection matrix $\hat{r}(\epsilon, V)$. Applying a voltage V (denoting the voltage in a two point measurement) on the normal side has two consequences. First, the voltage induces an electrostatic potential drop over the disorder region in the NS junction, resulting in a deformation of scattering states. The coupling of incident and outgoing channels is thus voltage dependent in general, as described by $\hat{r}(\epsilon, V)$. A stationary

²Note that the connection the unit charge currents on either side of the interface will not produce unitarity, since quasiparticle charge current is not a conserved quantity in the superconductor, see also appendix A

state incident from the normal lead (of energy ϵ in channel ν) consists of the incident electron and the reflected electron- and hole- states and carries the current ($e = |e|$),

$$I_\nu(\epsilon, V) d\epsilon = \frac{-e}{h} \left\{ 1 - \sum_\beta |r_{ee}(\epsilon, V)_{\beta\nu}|^2 + \sum_\beta |r_{he}(\epsilon, V)_{\beta\nu}|^2 \right\} d\epsilon. \quad (2.5)$$

Second, the applied voltage shifts the chemical potential of the reservoir attached to the normal lead by $-eV$ with respect to the reservoir on the superconducting side. The deformation of the states by itself produces no net current³. The net current flow results exclusively from the difference in occupation of the (finite voltage) scattering states incident from the left and right reservoirs. Writing the sum over channels as a trace, we obtain the current–voltage relation

$$I = \int d\epsilon \frac{1}{e} [f(\epsilon) - f(\epsilon + eV)] G_s(\epsilon, V), \quad (2.6)$$

with the spectral conductance

$$G_s(\epsilon, V) = \frac{2e^2}{h} \text{Tr} \left[1 - r_{ee}^\dagger(\epsilon, V) r_{ee}(\epsilon, V) + r_{he}^\dagger(\epsilon, V) r_{he}(\epsilon, V) \right]. \quad (2.7)$$

A factor two accounts for the spin degeneracy. The defined *spectral* conductance $G_s(\epsilon, V)$ describes the current contribution of the incident scattering states at energy ϵ , at a given voltage V (by convention, the energy is measured with respect to the chemical potential in the superconductor). Formulas (2.6) and (2.7) imply the differential conductance

$$\begin{aligned} \frac{dI}{dV} \Big|_V &= - \int d\epsilon f'(\epsilon + eV) G_s(\epsilon, V) \\ &+ \int d\epsilon \frac{1}{e} [f(\epsilon) - f(\epsilon + eV)] \frac{\partial G_s(\epsilon, V)}{\partial V}, \end{aligned} \quad (2.8)$$

with the expansion $dI/dV \Big|_V = G_s(-eV, 0) + 2V \partial_V G_s(\epsilon, V) \Big|_{\epsilon=-eV, V=0} + \dots$ at zero temperature. This differs from the differential conductance of Ref. [Blonder 1982], $dI/dV = G_s(-eV, 0)$, by accounting for the change in the conductance of the open channels with increasing voltage.

The expressions (2.4), (2.6), and (2.7) determine the general form of the current–voltage relation of a disordered NS junction, for an arbitrary scattering and pair potential at the NS interface.

We close this section with a discussion of the symmetry of the CVC with respect to sign reversal of the applied voltage. In the subgap regime $e|V| < \Delta$, the incoming

³This can be shown using the unitarity of the global scattering matrix including the Andreev process by an extension of the argument given for a normal junction.

quasiparticle excitations may not enter the superconductor. The probability current of the states $|\epsilon| < \Delta$ is totally reflected and thus the global reflection matrix $\hat{r}(\epsilon, V)$ of (2.3) is unitary. The unitarity produces the relations $r_{ee}^\dagger r_{ee} + r_{he}^\dagger r_{he} = 1$ and $r_{ee} r_{ee}^\dagger + r_{eh} r_{eh}^\dagger = 1$. The symmetry of electron- and hole- type excitations in the BdG equations guarantees $r_{eh}(\epsilon, V) = -r_{he}^*(-\epsilon, V)$. As a consequence, the subgap conductance takes the form

$$\begin{aligned} G_s(\epsilon, V) &= \frac{4e^2}{h} \text{Tr} \left[r_{he}^\dagger(\epsilon, V) r_{he}(\epsilon, V) \right] = \frac{4e^2}{h} \text{Tr} \left[r_{eh}^\dagger(\epsilon, V) r_{eh}(\epsilon, V) \right] \\ &= \frac{4e^2}{h} \text{Tr} \left[r_{he}^\dagger(-\epsilon, V) r_{he}(-\epsilon, V) \right] = G_s(-\epsilon, V). \end{aligned} \quad (2.9)$$

A subtle issue is that this symmetry does not yet imply a symmetry in the CVC under reversal of voltage [Leadbeater 1996]. The latter requires that $G_s(\epsilon, V) = G_s(-\epsilon, -V)$, which amounts to $G_s(\epsilon, V)$ being independent of voltage. Then we have $G_s(\epsilon) |_{\epsilon=-eV} = dI/dV|_V$ and the differential conductance is invariant under sign reversal of the voltage. Indeed, in recent experiments on SmS junctions [Magnée 1994, Poirier 1997a], an asymmetry in the CVC was found in the subgap regime, which can be understood on the basis of the above discussion taking into account the voltage dependent Schottky barrier at the SmS interface. An explicit account of the voltage dependence of G_s requires the scattering matrix \mathbf{S}_N to be determined in the applied electrostatic potential. In principle, this task demands the self-consistent solution of the scattering problem and the Poisson equation, see [Christen 1996]. In the next section, we evaluate the spectral conductance (2.7) by using the Andreev approximation for the scattering at the NS interface.

2.1.2 Spectral conductance in the Andreev approximation

The stationary states in the ballistic leads are solutions of the BdG equations [de Gennes 1966a] and are of the plane wave type. A step function model for the pair potential $\Delta(x) = \Delta_0 e^{i\chi} \theta(x)$ is assumed, which neglects the suppression of the pair potential in the superconductor on the scale of a coherence length. The NS interface connects electrons and holes of the same channel with a reflection amplitude depending on the reduced chemical potential $\mu_\nu = \mu - \hbar^2 \mathbf{k}_\perp^2 / 2m$. In the limit $\epsilon, \Delta \ll \mu_\nu$, the BdG equations are simplified by linearizing the dispersion relation around the effective Fermi wave number $k_\nu^{(0)} = \sqrt{2m\mu_\nu}/\hbar$. In this approximation made by Andreev, incoming electrons are purely reflected into holes and vice versa. The reflection matrix at the NS interface is given by

$$\hat{r}_I(\epsilon) = \begin{pmatrix} 0 & e^{-i\chi} \Gamma(\epsilon) \\ e^{i\chi} \Gamma(\epsilon) & 0 \end{pmatrix}, \quad (2.10)$$

depending on the channel independent, scalar Andreev amplitudes

$$\Gamma(\epsilon) = \begin{cases} \frac{\epsilon - \text{sign}(\epsilon) \sqrt{\epsilon^2 - \Delta^2}}{\Delta} \sim \frac{\Delta}{2|\epsilon|}, & |\epsilon| > \Delta, \\ \frac{\epsilon - i\sqrt{\Delta^2 - \epsilon^2}}{\Delta} = \exp(-i \arccos \frac{\epsilon}{\Delta}), & |\epsilon| < \Delta. \end{cases} \quad (2.11)$$

Inserting in (2.4) and (2.7), we obtain the multichannel spectral conductance formula

$$G_s(\epsilon, V) = \frac{2e^2}{h} (1 + |\Gamma(\epsilon)|^2) \text{Tr} \left\{ t_{21}^\dagger(\epsilon) \left[1 - \Gamma^*(\epsilon)^2 r_{22}^\top(-\epsilon) r_{22}^\dagger(\epsilon) \right]^{-1} \right. \\ \left. \times \left[1 - |\Gamma(\epsilon)|^2 r_{22}^\top(-\epsilon) r_{22}^*(-\epsilon) \right] \left[1 - \Gamma(\epsilon)^2 r_{22}(\epsilon) r_{22}^*(-\epsilon) \right]^{-1} t_{21}(\epsilon) \right\}. \quad (2.12)$$

Combined with equation (2.6), Eq. (2.12) provides the finite voltage, finite temperature CVC of a disordered normal–superconducting junction in the Andreev approximation. The spectral conductance depends on the scattering matrices of the electrons at energies $\pm\epsilon$ as a signature of the presence of Andreev reflection. The dependence of this formula on the phases of the reflection and transmission amplitudes proves crucial in determining the resonance peaks in the conductance. The elementary process, which contributes to these phases is the propagation of an electron and a hole between the disorder region and the NS interface.

If no inter-channel mixing takes place, i. e., the matrices t_{ij} and r_{ii} are diagonal, the conductance $G_s(\epsilon, V)$ reduces to the quasi one-dimensional form

$$\frac{2e^2}{h} \sum_{\nu=1}^N \frac{(1 + |\Gamma(\epsilon)|^2) T_\nu(\epsilon, V) [1 - |\Gamma(\epsilon)|^2 R_\nu(-\epsilon, V)]}{1 + |\Gamma(\epsilon)|^4 R_\nu(\epsilon, V) R_\nu(-\epsilon, V) - 2\text{Re} [\Gamma(\epsilon)^2 r_\nu(\epsilon, V) r_\nu^*(-\epsilon, V)]}. \quad (2.13)$$

$r_\nu = (r_{22})_{\nu\nu}$ is the reflection amplitude for a state coming in from the right side of the scattering region (Fig. 2.1) and $R_\nu = |r_\nu|^2$ and $T_\nu = 1 - R_\nu$ denote the reflection and transmission probabilities of the ν -th channel.

For voltages well *above* the gap, $|\epsilon|, V \gg \Delta$ (still assuming $|\epsilon| \ll \mu$), the Andreev reflection is strongly suppressed and drops according to $\Gamma(\epsilon, V) \sim \Delta/2|\epsilon| \rightarrow 0$. The spectral conductance (2.12) asymptotically approaches the expression for a normal junction,

$$G_s(\epsilon, V) = \frac{2e^2}{h} \text{Tr} \left[t_{21}^\dagger(\epsilon, V) t_{21}(\epsilon, V) \right]. \quad (2.14)$$

At voltages *below* the gap, we make use of $|\Gamma(\epsilon)| = 1$ and $T_\nu = 1 - R_\nu$ and obtain the spectral conductance $G_s(\epsilon, V)$ in the form

$$\frac{4e^2}{h} \sum_{n=1}^N \frac{T_\nu(\epsilon, V) T_\nu(-\epsilon, V)}{1 + R_\nu(\epsilon, V) R_\nu(-\epsilon, V) - 2\text{Re} [\Gamma(\epsilon)^2 r_\nu(\epsilon, V) r_\nu^*(-\epsilon, V)]}. \quad (2.15)$$

The reflection and transmission coefficients at $\pm\epsilon$ are symmetrically involved in this formula, which results in the symmetry of the CVC discussed in the section above. In contrast, the spectral conductance (2.13) at voltages above the gap becomes increasingly asymmetric as it asymptotically approaches the Landauer expression. The sensitivity of (2.15) to the phase of the reflection amplitudes allows for the distinction of zero and finite bias peaks in the double barrier NS junction discussed below.

The linear response limit ($\epsilon, V \rightarrow 0$) of (2.15) can be determined using $\Gamma(0)^2 = 1$ and $R_\nu = 1 - T_\nu$ and takes the form [Beenakker 1992a]

$$G(0) = \frac{4e^2}{h} \sum_n \frac{T_\nu(0)^2}{[2 - T_\nu(0)]^2}. \quad (2.16)$$

2.1.3 Double barrier NINIS junction

In this section we apply the above results to a double barrier NINIS junction, which allows to study the interplay between normal- and Andreev- levels in a Fabry–Perot type I_1NI_2 interferometer. First, we discuss the structure in the conductance of a single channel NI_1NI_2S junction, which we trace back to the presence of Andreev resonances. Second, we present numerical results for a multichannel junction, showing that the typical resonance structure of a single channel survives the summation over the channels. This stability is a peculiarity of the superconducting system, absent in a normal NI_1NI_2N double barrier junction.

Since the channels separate in the double barrier problem, we can make use of the result (2.13) for the conductance G_s . G_s depends on the phases $\varphi(\pm\epsilon)$ of the reflection amplitudes $r(\pm\epsilon)$ as well as on the complex amplitude $\Gamma(\epsilon)$ of the Andreev reflection. We use the notation $T(\pm\epsilon) = T_\pm$, $R(\pm\epsilon) = R_\pm$, and $r(\pm\epsilon) = \sqrt{R_\pm} e^{i\varphi(\pm\epsilon)}$ for the reflection amplitude, the phase factors being determined by the potential barriers I_1 and I_2 and the propagation between them. We rewrite the amplitude of the Andreev reflection as $\Gamma(\epsilon) = |\Gamma| e^{-i\vartheta(\epsilon)}$ with the phase $\vartheta(\epsilon) = \arccos(\epsilon/\Delta)$ below the gap and vanishing above. The conductance $G_s(\epsilon)$ simplifies to

$$\frac{2(1 + |\Gamma|^2) e^2}{h} \frac{T_+ (1 - |\Gamma|^2 R_-)}{1 + |\Gamma|^4 R_+ R_- - 2|\Gamma|^2 \sqrt{R_+ R_-} \cos[\varphi(\epsilon) - \varphi(-\epsilon) - 2\vartheta(\epsilon)]}, \quad (2.17)$$

which is always less or equal to the universal value $4e^2/h$. Note that the Andreev reflection is suppressed above the gap ($|\Gamma| < 1$), while the phase $\vartheta(\epsilon)$ vanishes.

Below the gap the conductance exhibits resonances, which is maximal if R_\pm are equal and the scattering phase difference of the electrons and holes compensates for the phase of the Andreev reflection, according to the resonance condition

$$\cos[\varphi(\epsilon) - \varphi(-\epsilon) - 2\vartheta(\epsilon)] = 1. \quad (2.18)$$

Let us assume that the barrier at the NS interface vanishes, $I_2 = 0$, and denote the length of the interferometer by d . In the limit of a high potential barrier I_1 , R_+ and R_- are energy independent and equal, and $\varphi(\pm\epsilon) = \pi + 2k_{\pm}d$. Using the wave number $k_{\pm} = mv_{\nu} \pm \epsilon/v_{\nu}$ (v_{ν} is the Fermi velocity of channel ν), the resonance condition (2.18) yields the spectrum of Andreev levels,

$$\epsilon_{n,\nu} = \frac{v_{\nu}}{2d} \left(n\pi + \arccos \frac{\epsilon_{n,\nu}}{\Delta} \right), \quad n = 0, 1, \dots \quad (2.19)$$

which predicts resonances in the conductance of a typical width proportional to the transmission T of the barrier. The phase $\vartheta(\epsilon)$ varies between $-\pi/2$ and 0 from $\epsilon = 0$ to $\epsilon = \Delta$ and guarantees the existence of at least one Andreev resonance for arbitrarily small d . In the $d \rightarrow 0$ limit, the weight of this resonance lines up with the gap voltage and we recover the NIS junction, featuring a suppressed subgap conductivity and a peak in the differential conductance at the gap voltage. This peak can be understood in terms of the Andreev resonance which moves to the gap energy for $d \rightarrow 0$.

We now turn to double barrier $\text{NI}_1\text{NI}_2\text{S}$ junction with arbitrary barriers. Here $\varphi(\pm\epsilon)$ represent the phases for the reflection of electrons entering the double barrier scattering region from the right (superconducting side). The corresponding reflection amplitudes are given by

$$r(\pm\epsilon) = r_2 + \frac{t_2^2 r_1 e^{2ik_{\pm}d}}{1 - r_1 r_2 e^{2ik_{\pm}d}}, \quad (2.20)$$

where r_i, t_i are the amplitudes of the left ($i = 1$) and the right ($i = 2$) barrier. The phase of this reflection amplitude plays the major role in determining the structure of the conductance, as it controls the existence of resonances according to (2.18). Let us fix the barrier I_1 and increase I_2 slowly, keeping their strengths $I_1 > I_2$. In this situation, the INI interferometer develops pronounced Andreev resonances. For $r_1 \gg r_2$, the phase $\varphi(\pm\epsilon)$ of the reflection amplitude $r(\pm\epsilon) \approx t_2^2 r_1 e^{2ik_{\pm}d}$ produces a linear energy dependence of the phase $\varphi(\epsilon)$, which changes by 2π on the scale v_F/d and results in (nearly) equidistant resonances, in accordance with (2.19). As the strength of I_2 is increased, the resonances pair up as is illustrated in Figure 2.2. The phase function $\varphi(\epsilon)$, as displayed in Figure 2.2 (solid line), can be used to determine the location of the resonances by finding those combinations of energies $\pm\epsilon$, which have a phase difference⁴ $\Delta\varphi(\epsilon) = \varphi(\epsilon) - \varphi(-\epsilon) = \pi + 2n\pi$. The period of $\Delta\varphi(\epsilon)$ reduced by half with respect to the period of $\varphi(\epsilon)$ accounts for the pairing of the resonances.

When the strengths of the barriers become of the same order, $I_1 \sim I_2$, the spectral weight of the INI interferometer is shared by Andreev quasi-bound states of a mixed

⁴The energy dependence of the Andreev reflection amplitude produces slight deviations close to the gap energy.

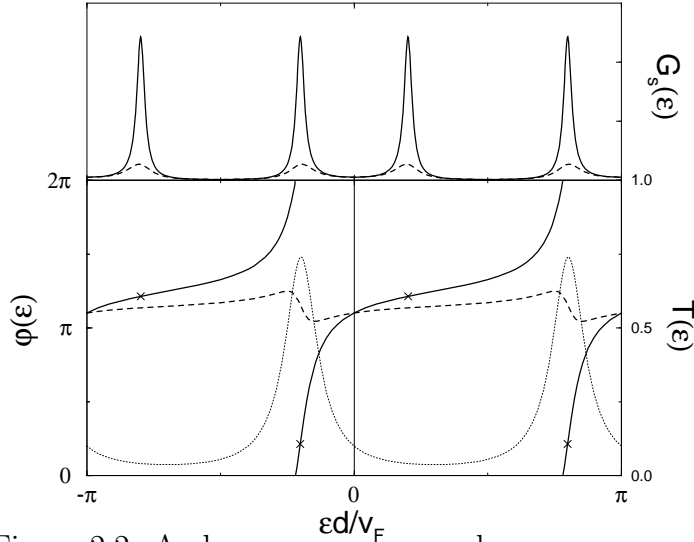


Figure 2.2: Andreev resonances and resonance condition for the phase φ . Bottom: phase $\varphi(\epsilon)$ of the reflection amplitude versus energy. The solid line represents the I_1NI_2 interferometer with barriers strengths $R_1 = 0.8$ and $R_2 = 0.5$, the dashed line stands for the inverse barrier sequence ($R_1 = 0.5$, $R_2 = 0.8$). The *Andreev* resonance condition for the phase is met for a pair of energies $\pm\epsilon_n$ with phase difference $\Delta\varphi(\epsilon_n) = \pi + 2n\pi$. This phase condition can be fulfilled only by the first barrier sequence ($R_1 > R_2$, solid line) at those energies indicated in the graph. The dotted line shows the transmission probability T as determined by the *normal* resonances. Top: conductance (arbitrary units) of the double barrier NS junction versus energy, the solid line again representing the barriers $R_1 = 0.8$, $R_2 = 0.5$, and the dashed line the barriers $R_1 = 0.5$, $R_2 = 0.8$. Note the symmetry of the resonances with respect to $\epsilon = 0$.

electron–hole character and normal electron quasi-bound states. Due to the large gradient of the phase close to the normal resonances, see Fig. 2.2, the Andreev resonances tend to be pinned to normal resonances at either $+\epsilon$ or $-\epsilon$. While the Andreev bound states contribute to the current, normal bound states do not couple to the superconductor and thus do not participate in the charge transport. This is reflected by the subgap symmetry of the $G_s(\epsilon)$ under reversal of voltage which is observed for all barrier strengths, see Fig. 2.2.

As the barrier strength is increased further to $I_2 > I_1$, the Andreev resonances are weakened and eventually disappear. Although the normal resonances dominate in the INI interferometer in this regime, only the weak Andreev resonances show up in the conductance, which thus exhibits only a weak subgap structure. The phase function $\varphi(\epsilon)$ in Figure 2.2 (dashed line) becomes nearly constant for $r_1 \ll r_2$, see

(2.20), and the phase condition for resonance (2.18) cannot be met.

A comparison of the double barrier systems $\text{NI}_1\text{NI}_2\text{S}$ and $\text{NI}_2\text{NI}_1\text{S}$, i.e., with inverse sequences of the barriers I_1 and I_2 , is given in Fig. 2.2. The transmission $T(\epsilon)$ (dotted line) is identical for both cases. Let us assume that $\text{I}_1 \gg \text{I}_2$. In this first barrier sequence, we have a strong energy dependence of the phase $\varphi(\epsilon)$ (solid line in Fig. 2.2), which implies the existence of Andreev type resonances at finite bias. The electrons entering the INI interferometer from the normal lead, are given enough time to build up an Andreev resonance and preferably leave into the superconductor. For the inverse barrier sequence, the barrier I_2 at the NS interface dominates. The weak energy dependence of the phase $\varphi(\epsilon)$ of reflection allows no sharp resonances to build up (dashed line in Fig. 2.2). This reflects the fact that the electrons which enter the INI region leave through I_1 into the normal lead before an Andreev resonance can build up. In summary, the spectral density in the INI interferometer changes radically with the coupling strengths of the normal and superconducting leads. Normal resonances dominate when the interferometer is coupled more strongly to the normal lead, whereas Andreev resonances take over in weight when the coupling to the superconductor is stronger. At any instant, however, only the Andreev states participate in the charge transport.

We turn to the numerical analysis of a multichannel NINIS junction. With Eq. (2.13) we extend the linear response study of Ref. [Melsen 1994] to finite voltage. We investigate an $\text{NI}_1\text{NI}_2\text{S}$ junction with two δ -function barriers of typical strength $H = \int V(x)dx \approx \hbar v_F$ and corresponding reflection probability $R = H^2 / (H^2 + \hbar^2 v_F^2)$ assuming values between $R = 0.2$ and $R = 1$. We vary the relative barrier strengths to cover the range between the two limits $\text{I}_1 > \text{I}_2$ and $\text{I}_1 < \text{I}_2$ discussed above. The distance between the barriers is chosen to be of the order of or larger than the coherence length of the superconductor, providing the forward channel with one to a few Andreev resonances. The number of resonances increases with the incidence angle of the channels. We chose leads with a cross section area of $(100/k_F)^2$, which amounts to about 800 transverse channels. The ratio of the energy gap to the Fermi energy is assumed to be $\Delta/\epsilon_F = 0.002$. Each channel features the typical conductance structure of paired Andreev resonances exposed above. Their positions and widths depend on the ratio of the barrier strengths I_1 and I_2 as well as the longitudinal kinetic energy of the single channels. Remarkably, the overall conductance, which is obtained through summation of single channel conductances, exhibits a characteristic subgap structure signaling the presence of Andreev resonances. In contrast, the overall conductance of the corresponding $\text{NI}_1\text{NI}_2\text{N}$ junction is practically constant, the normal resonances of the INI region having been averaged out.

The numerical study of a 3-dimensional NINS junction has shown that both the positions and the number of resonances in the overall conductance correspond

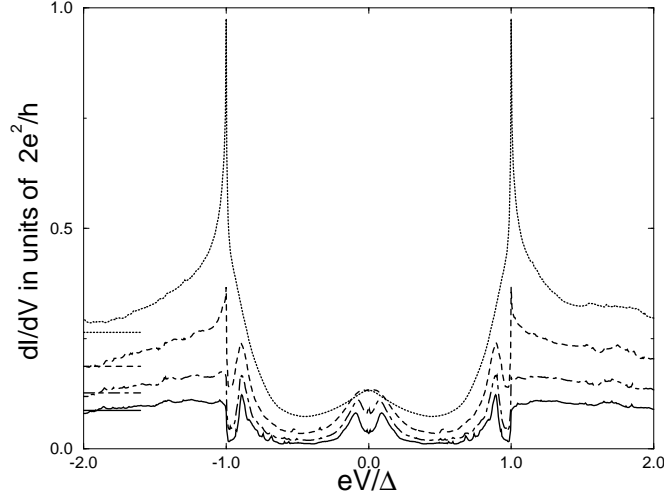


Figure 2.3: Differential conductance for a multichannel NINIS junction with interbarrier distance $d = 2v_F/\Delta = 2\pi\xi$. The average conductance per channel is plotted versus voltage at temperature $T = 0$. The barrier strengths are chosen to be $R_1 = 0.2$ (dotted line), 0.5 (dashed), 0.7 (dot-dashed), and 0.8 (solid) in the normal region, while $R_2 = 0.5$ at the NS interface. The normal state conductance, which is roughly independent over this voltage range, is indicated on the left. With increasing barrier strength R_1 the zero bias anomaly develops into a finite bias anomaly as the Andreev resonance is formed for $R_1 > R_2$.

to those in the forward channel [Chaudhuri 1995]⁵. In the NINIS junction, we do not find a direct correspondence of the resonances of the total conductance with the forward channel nor with any other specific channel, although a clear resonance structure still survives the summation over the channels.

Let us concentrate on the conductance formula (2.15), valid at subgap voltages, and on the properties of the CVC close to zero voltage. For $I_1 > I_2$, the denominator of (2.15) changes rapidly with the strong energy dependence of the phase of $r_\nu(\epsilon)$ which is responsible for the appearance of conductance peaks at finite voltage. The pronounced structure in the conductance survives the summation over the channels as displayed in Figures 2.3 and 2.4 (solid lines). The repulsion of the Andreev levels

⁵This is connected to the decrease of the transmission probability with increasing incidence angle, and the non-isotropic distribution of the channels over the incidence angles [Chaudhuri 1995], which is $\propto \sin(2\vartheta)$.

around zero voltage produces a minimum in dI/dV at zero voltage. For $I_1 < I_2$, the phase of the reflection amplitudes $r_\nu(\epsilon)$ has negligible energy dependence and the numerator of (2.15) dictates the features of the conductance. The expansion of the product $T_\nu(\epsilon)T_\nu(-\epsilon) = T_\nu^2 - \epsilon^2 T_\nu'^2$ about zero energy shows the existence of a zero bias maximum. The zero bias anomaly shows up as a characteristic property of the overall conductance, see Figures 2.3 and 2.4 (dotted lines). The zero bias maximum coincides with the maximum of the conductance product $G(\epsilon)G(-\epsilon)$ of the corresponding NININ junction at zero energy. Figs. 2.3 and 2.4 illustrate the crossover from zero to finite bias anomalies for two different interbarrier distances d as the strength of barrier I_1 is increased and I_2 is kept fixed. For an interbarrier distance larger than the coherence length of the superconductor, several Andreev resonances show up (see Fig. 2.4). Note that the inversion of the barrier sequence transforms the zero voltage conductance from a local minimum to a local maximum, while keeping the same zero voltage conductance.

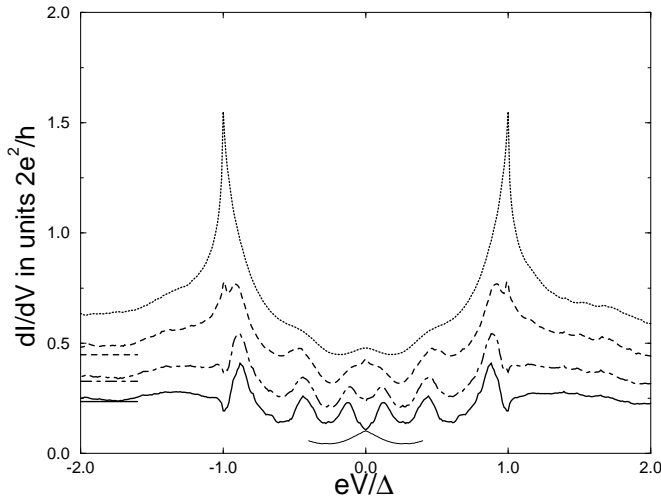


Figure 2.4: Differential conductance for a multichannel NINIS junction of width $d = 4v_F/\Delta = 4\pi\xi$. The average conductance per channel is plotted versus voltage for temperature $T = 0$. The barrier strengths are $R_1 = 0.04$ (dotted line), 0.2 (dashed), 0.4 (dot-dashed), and 0.54 (solid) in the normal region, and fixed at $R_2 = 0.2$ at the NS interface. The normal state conductivity is indicated on the left. As the strength R_1 is increased, the zero bias anomaly turn into an finite bias anomaly and several Andreev resonances appear. For the last choice of barriers we have interchanged the barrier sequence: the conductance at zero voltage remains the same while changing from a zero bias minimum to a zero bias maximum (short solid line).

The interference of multiple scattering processes between the scattering region and the NS interface thus produces an interesting structure in the differential conductance. Recently, experiments in disordered NS and SmS junctions [Kastalsky 1991, Nguyen 1992, Nitta 1994, Bakker 1994, Magnée 1994] have concentrated on the observation of zero and finite bias anomalies. It has been understood theoretically [Volkov 1993, Marmokos 1993, Yip 1995, van Wees 1992] that these features are due to the interplay between the barrier at the NS interface and disorder in the normal lead. At small disorder, the differential conductance exhibits a zero bias maximum, while at large enough disorder, a finite bias peak is expected [Yip 1995] at a voltage of the order of the Thouless energy E_c of the normal lead [Edwards 1972]. This has recently been confirmed in an experiment [Poirier 1997a, Poirier 1997b]. Here, we have found the existence of the analog features in a ballistic double barrier NS junction (in addition, the double barrier junction shows higher harmonics in the resonances of the conductance). The ballistic point of view applied to the disordered NS junction thus explains the finite bias anomaly as a superposition of resonances due to quasi-bound Andreev states between the superconductor and the disorder. This interpretation applies in the same way to recent experiments showing a low-temperature reentrance in the conductance [Petrashov 1995, Charlat 1996]. The non-monotonicity is again due to the resonance structure in the spectral conductance $G(\epsilon)$, which now appears as a function of temperature.

2.1.4 Discussion

We have described the current–voltage characteristics of NS junctions by the scattering matrix approach and expressed it through the spectral conductance, which takes into account the explicit voltage dependence of the scattering problem. The spectral conductance is symmetric under sign reversal of voltage in the in the subgap regime. We have derived Eq. (2.13) giving the spectral conductance in terms of the normal scattering amplitudes. This result has enabled us to carry out a study of a double barrier NINIS junction at finite voltage. As the ratio of the barrier strengths of the INI interferometer is changed, and we go over from normal to Andreev resonances, the conductance shows a cross-over from a zero bias to a finite bias peak.

2.2 Finite voltage shot noise in normal-metal – superconductor junctions

2.2.1 Introduction

Shot noise arises from the current fluctuations in transport as a consequence of the discrete nature of the carriers, first predicted by Schottky for the vacuum tube [Schottky 1918]. In a coherent conductor the quantum fluctuations, which follow from the probabilistic nature of the backscattering restricted by the Pauli principle, are reduced in comparison to the Schottky result [Lesovik 1989, Büttiker 1992]. In a disordered normal-metal–superconductor (NS) junction, the shot noise is produced by the normal scattering processes as well as the imperfect Andreev reflection [Khlus 1987, Muzykantskii 1994, de Jong 1994, Hessling 1996]. The Andreev reflection introduces fluctuations proportional to the double electron charge, which may be iteratively increased to give fluctuations of several charge quanta in biased SNS junctions [Averin 1996]. For a review, we refer the reader to [de Jong 1997]. In this chapter we study the shot noise at finite voltage in a disordered NS junction as well as its structure due to the iterative scattering processes between the disordered normal lead and the NS interface. We derive a formula which expresses the differential shot noise of the dirty NS junction in terms of the scattering matrix of the normal lead and the (scalar) amplitude of Andreev reflection. In the systems of a single barrier normal-metal–insulator–normal-metal–superconductor (NINS) junction and a double barrier NINIS junction, we explain the existence of a non-trivial resonance structure. The results of chapter 2.2 have been published in [Fauchère 1998].

We consider a disordered NXS junction, shown in the inset of Fig. 2.5, with an arbitrary elastic scattering region X in the normal lead, whose effect on the noise is to be determined. We restrict ourselves to voltages below the superconducting gap $eV \ll \Delta$. The low-frequency power spectrum of the current fluctuations is determined by the irreducible current–current correlator

$$P = \int dt e^{i\omega t} \langle\langle I(t) I(0) \rangle\rangle, \quad \omega \rightarrow 0 \quad (2.21)$$

($\langle\langle I(t) I(0) \rangle\rangle = \langle(I(t) - \langle I \rangle)(I(0) - \langle I \rangle)$ is the second cumulant in time). The time-dependence of the current operator is defined by

$$I(t) = \exp[i(H - \mu N)t] I \exp[-i(H - \mu N)t]. \quad (2.22)$$

In the mean field approximation for the Hamiltonian H we do not account for the fluctuations of the order parameter in the S region. The effective Hamiltonian is diagonalized by a Bogoliubov transformation [Niño 1984]. After integration over the

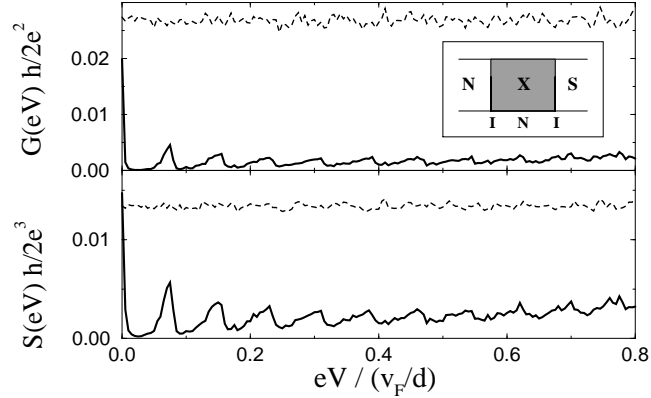


Figure 2.5: Differential conductance (top) and shot noise (bottom) in a multichannel NINIS junction (see inset, symmetrical barriers of strength $\int dx V(x) = 3\hbar v_F$, $T_1 = T_2 \approx 0.05$, interbarrier distance $d = 20 v_F/\Delta$, 8×10^4 channels). The average shot noise per channel [Eq. (2.28)] exhibits maxima at the resonances of the conductance (solid lines). Note the enhanced structure of the noise with respect to the conductance [Eq. (2.26)]. The dashed lines show the corresponding results for the normal state NININ junction. Inset: schematic NXS junction, e.g., X = INI.

cross-section, the net current operator can be expressed through the positive energy eigenfunctions,

$$I(t) = \frac{-e}{mi} \sum_{\epsilon_m, \epsilon_n > 0} \int dy dz (u_m^* \hat{\partial}_x u_n \gamma_m^\dagger \gamma_n - v_m^* \hat{\partial}_x v_n \gamma_n \gamma_m^\dagger) e^{i(\epsilon_m - \epsilon_n)t} \quad (2.23)$$

which may be evaluated in the normal lead. The operators γ_m belonging to the wavefunctions (u_m, v_m) annihilate the scattering states of the disordered NS junction (note $u \hat{\partial}_x v = u \partial_x v - v \partial_x u$). We note that the symmetry of the BdG eigenfunctions (u_n, v_n) , ϵ_n with respect to sign reversal of energy to $(-v_n^*, u_n^*)$, $-\epsilon_n$ is the consequence of spin degeneracy in Nambu space, allowing the the negative energy states to be eliminated in favor of the positive energy states, see Appendix A. At voltages below the superconducting gap ($eV < \Delta$), the quasi-particles are injected from the normal reservoir only, and the wavefunctions depend on the $N \times N$ global reflection matrices $r_{ee}(\epsilon)$, $r_{he}(\epsilon)$, $r_{eh}(\epsilon)$, and $r_{hh}(\epsilon)$ of the disordered NS junction, see Eq. (2.3). The scattering states indexed by $m = [{}_h^e, \mu, \epsilon]$ consist of an incident e (lectron) or h (ole) like quasi-particle in channel μ with energy ϵ superposed with the reflected electron and hole states. The occupation numbers are given by the Fermi-Dirac distribution $f_{e,h} = f(\epsilon \pm eV)$.

The noise power (2.21) is determined by the transitions induced by the current operator I from initial states $|n\rangle = |n_n = 1, n_m = 0\rangle$ to intermediate states $|m\rangle = |n_n = 0, n_m = 1\rangle$ and back, which differ only by their occupation with respect

to two single particle states with indices n and m . E.g., the transition between an incident electron $n = [e, \nu, \epsilon]$ and an incident hole state $m = [h, \mu, \epsilon]$ is produced by the matrix element between the reflected electrons and holes of the two scattering states with respect to the current operator, $\langle m|I|n\rangle \propto f_e(1-f_h)(r_{eh}^\dagger r_{ee} - r_{hh}^\dagger r_{he})_{\mu\nu}$. Summed over the channels, the transitions contribute to the fluctuations with the weight $\sum_{\mu,\nu} |\langle m|I|n\rangle|^2 \propto f_e(1-f_h) \text{Tr}\{(r_{ee}^\dagger r_{eh} - r_{he}^\dagger r_{hh})(r_{eh}^\dagger r_{ee} - r_{hh}^\dagger r_{he})\} = f_e(1-f_h) \text{Tr}\{r_{he}^\dagger r_{he}(1 - r_{he}^\dagger r_{he})\}$. Following the quantum mechanical formalism outlined, we obtain the low-frequency limit of the power spectrum [Anantram 1996, Martin 1996] valid for $T, eV < \Delta$,

$$P = \frac{4e^2}{h} \int_0^\Delta d\epsilon \left\{ [f_e(1-f_h) + f_h(1-f_e)] \text{Tr} \left[r_{he}^\dagger r_{he} \left(1 - r_{he}^\dagger r_{he} \right) \right] + [f_e(1-f_e) + f_h(1-f_h)] \text{Tr} \left[\left(r_{he}^\dagger r_{he} \right)^2 \right] \right\}. \quad (2.24)$$

The first term describes the transitions between states of opposite current sign, while the second represents the transitions between states of equal current sign. At zero temperature, the second term is suppressed by the Pauli principle and the first term produces the shot noise [Lesovik 1989, Lesovik 1994, Levitov 1996]. The thermal fluctuations describing the Johnson-Nyquist noise [Johnson 1927, Nyquist 1928] are due to both terms. Eq. (2.24) is manifestly invariant under sign reversal of voltage, see Chp. 2.1.

2.2.2 Interplay between normal scattering and Andreev reflection

We express the electron-hole reflection matrix $r_{he}(\epsilon)$ in Eq. (2.24) in terms of the normal reflection- and transmission matrices r_{ii} and t_{ij} of the scattering (X) region and the amplitude of Andreev reflection Γ at the XS interface,

$$r_{he}(\epsilon) = t_{12}^*(-\epsilon) [1 - \Gamma^2(\epsilon) r_{22}(\epsilon) r_{22}^*(-\epsilon)]^{-1} \Gamma(\epsilon) t_{21}(-\epsilon), \quad (2.25)$$

see Eqs. (2.4) and (2.10), recalling $\Gamma(\epsilon) = e^{i\vartheta(\epsilon)}$, $\vartheta(\epsilon) = \arccos(\epsilon/\Delta)$. Inserting $r_{he}(\epsilon)$ in Eq. (2.24) provides us with a general multichannel expression for the shot noise in a disordered NXS junction, explicit in the normal scattering matrix and the Andreev reflection amplitude.

Next we restrict ourselves to the situation of a junction with uniform transverse cross-section, which permits the separation of channels and will be used in the single and double barrier systems below. We recall that the differential conductances of the channels $\nu = 1 \dots N$ are given by

$$\frac{h}{4e^2} G_\nu(\epsilon) = \left(r_{he}^\dagger r_{he} \right)_{\nu\nu}, \quad (2.26)$$

see Eq. (2.15). At zero temperature, the shot noise (2.24) exhibits the noise power

$$P = \frac{1}{e} \int_0^{e|V|} d\epsilon \sum_{\nu} S_{\nu}(\epsilon), \quad (2.27)$$

with the differential (low-frequency) shot noise of channel ν ,

$$\begin{aligned} \frac{h}{2e^3} S_{\nu}(\epsilon) &= 4 \left(r_{he}^{\dagger} r_{he} \left(1 - r_{he}^{\dagger} r_{he} \right) \right)_{\nu\nu} \\ &= \frac{4T_{\nu}(\epsilon) T_{\nu}(-\epsilon) (R_{\nu}(\epsilon) + R_{\nu}(-\epsilon) - 2\text{Re} [\Gamma(\epsilon)^2 r_{\nu}(\epsilon) r_{\nu}^*(-\epsilon)])}{(T_{\nu}(\epsilon) T_{\nu}(-\epsilon) + R_{\nu}(\epsilon) + R_{\nu}(-\epsilon) - 2\text{Re} [\Gamma(\epsilon)^2 r_{\nu}(\epsilon) r_{\nu}^*(-\epsilon)])^2}. \end{aligned} \quad (2.28)$$

$r_{\nu}(\epsilon)$ is the reflection amplitude of channel ν in the matrix $r_{22}(\epsilon)$ describing the reflection from the *right*-hand side of the X region, $R_{\nu}(\epsilon) = |r_{\nu}(\epsilon)|^2$, and $T_{\nu}(\epsilon) = 1 - R_{\nu}(\epsilon)$. The two energy dependencies of the reflection probabilities $R_{\nu}(\epsilon)$ and (the phases of) the reflection amplitudes $r_{\nu}(\epsilon)$ translate into the voltage dependence of the shot noise. The term sensitive to the phases of the reflection amplitudes is due to the states multiply scattered between the disorder and the NS interface. Note the similarity of Eq. (2.28) to the conductance formula (2.13). In the limit $\epsilon \rightarrow 0$ ($\Gamma \rightarrow -i$) the phase dependencies drop out of Eq. (2.28) and we recover the linear response result [de Jong 1997],

$$\frac{h}{2e^2} S_{\nu}(0) = \frac{16T(0)^2[1 - T(0)]}{[2 - T(0)]^4}. \quad (2.29)$$

In order to describe the weak coupling of a normal lead to an NS proximity sandwich, we consider a normal-metal–insulator–normal-metal–superconducting (NINS) junction with a potential barrier of low transmission ($T \ll 1$) placed at a distance d away from the perfect NS interface. The NINS junction serves as a model system for a tunneling experiment from a metallic tip to a thin film NS layer structure, which has permitted the observation of the Rowell-McMillan oscillations [Rowell 1966]. In this elementary model, the reflection amplitudes $r_{\nu}(\epsilon) = \sqrt{R}e^{i\varphi_{\nu}(\epsilon)}$ have a roughly constant modulus R and an energy dependent phase $\varphi_{\nu}(\epsilon) \approx 2(k_{\nu} + \epsilon/v_{\nu})d + \varphi_0$, accumulated during the propagation between the potential barrier and the NS interface (k_{ν} , v_{ν} denote the Fermi wave number and velocity of channel ν). Consequently the shot noise (2.28) for the channel ν ,

$$\frac{h}{2e^3} S_{\nu}(\epsilon) = \frac{8T^2R[1 - \cos \alpha_{\nu}(\epsilon)]}{(T^2 + 2R[1 - \cos \alpha_{\nu}(\epsilon)])^2}, \quad (2.30)$$

depends only on the phase difference $\alpha_{\nu}(\epsilon) = \varphi_{\nu}(\epsilon) - \varphi_{\nu}(-\epsilon) - 2\vartheta(\epsilon)$ of electron and hole propagation through the X (=IN) region. The resonance structure of S_{ν} is

intimately connected to the voltage (energy $\epsilon = eV$) dependence of the differential conductance (2.15),

$$\frac{h}{4e^2}G_\nu(\epsilon) = \frac{T^2}{T^2 + 2R[1 - \cos \alpha_\nu(\epsilon)]}. \quad (2.31)$$

Figures 2.6(a) and 2.6(b) show their generic dependence on α_ν . The minima of the denominator [$\cos \alpha_\nu = 1 \Rightarrow \epsilon_{\nu,n} = v_\nu/2d(n\pi + \arccos \epsilon_{\nu,n}/\Delta)$] correspond to the resonances of the Andreev quasi-bound states. These conductance resonances are repelled from zero voltage, since the phase of the Andreev reflection $\vartheta(\epsilon \rightarrow 0) = \pi/2$ has to be compensated by the phase difference of electron and hole propagation $\varphi_\nu(\epsilon) - \varphi_\nu(-\epsilon)$. The shot noise (2.30) vanishes at these resonances ($S_\nu(\epsilon_{\nu,n}) = 0$). The noise maxima are found from $\cos \alpha_\nu = (2R - T^2)/2R$ at energies doubly peaked close to the resonances. The peak separation $\delta\epsilon \sim Tv_F/d$ coincides with the width of the resonances.

Interestingly, this non-trivial structure survives in the multichannel NINS junction, whose results are shown in Figs. 2.6(d) and 2.6(e). The stability of the resonance structure is due to its pinning to the Fermi energy. In contrast, the resonance structure of a potential well in a normal conductor is washed out in the multichannel limit. As Figures 2.6(b,e) show, the narrow double peak structure in the noise is smeared out in the multichannel limit, and the noise S takes a maximum rather than a minimum at the resonance, retracing the shape of the conductance.

At large voltages ($eV \gg v_F/d$), the shot noise approaches a constant as a consequence of the dephasing between the channels. The channel average may be evaluated by averaging over the phase α_ν in Eqs. (2.30) and (2.31) and we obtain the result ($\alpha_\nu (1/N \sum_n \rightarrow 1/2\pi \int_0^{2\pi} d\alpha)$),

$$\bar{S} = \frac{1}{2\pi} \int_0^{2\pi} d\alpha S_\nu(\alpha) = \frac{2e^3}{h}T, \quad \bar{G} = \frac{2e^2}{h}T. \quad (2.32)$$

It follows that both the shot noise and the conductance approach the normal state values at voltages $v_F/d \ll eV \ll \Delta$. This limiting behavior demonstrates that the NIN junction is effectively decoupled from the NS interface in the large voltage limit and dominates both noise and conductance due to its low transparency.

Let us concentrate on the overall ratio of noise power to current P/eI [$P = \int_0^{e|V|} d\epsilon S(\epsilon)$, $I = \int_0^{eV} d\epsilon G(\epsilon)$]. This ratio has already been used successfully in determining the unit of the charge carriers in the Fractional Quantum Hall Effect [Glattli 1997, de-Picciotto 1997]. While at small voltages ($P/eI = 2$) the noise carries the signature of the Cooper pairs created by the Andreev reflection, at large voltages ($v_F/d \ll eV \ll \Delta$) it decays to the normal state value ($P/eI = 1$). Interestingly, this decay is immediate at the first Andreev resonance, as is seen from Figs. 2(c) and (f). In fact, in a single channel, the energy integration is equivalent to

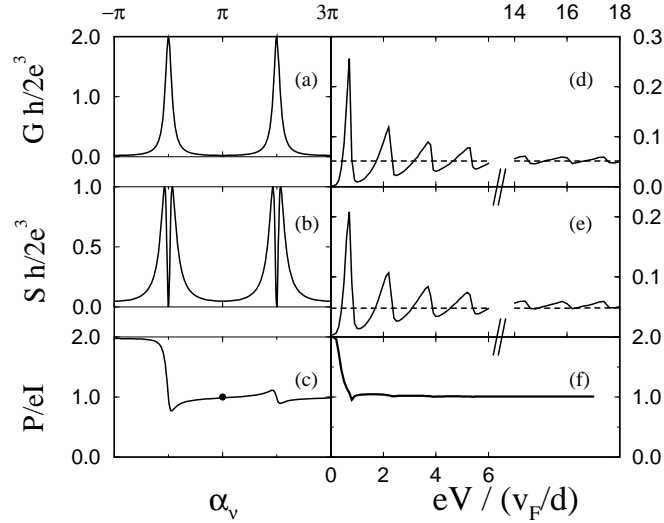


Figure 2.6: Zero temperature conductance (a,d), differential shot noise (b,e), and finite voltage noise power to current ratio (c,f) for a NINS junction with a barrier of strength $\int dx V(x) = 3\hbar v_F$, average transmission $T = 0.05$, $\epsilon_F = 500\Delta$, $d = 20 v_F/\Delta$ ($v_F/d \ll \Delta \ll \epsilon_F$). (a,b,c) follow from Eqs. (2.30) and (2.31) for one channel. (d,e,f) from Eqs. (2.15) and (2.28) are averaged over 8×10^4 channels. Note the pronounced resonance structure in both conductance (d) and noise (e), which approaches the values for the corresponding NIN junction at large voltages (dashed lines). The noise to current ratio (c,f) decays to the classical Schottky value $P/eI = 1$ above the Andreev minigap.

the integration over the phase α_ν , which at the midpoint between two resonances α_ν has covered the period 2π , thus producing $P/eI = 1$ at $\alpha_\nu = \pi$, see Fig. 2(c). In the transport through a normal lead weakly coupled to a NS sandwich, we thus find two characteristic regimes: At voltages below $eV < v_F/d$ the one-particle excitations in the NS structure are effectively gapped and we may only couple to the superconducting condensate which introduces the charge $2e$ in the noise power. At voltages above the first Andreev resonance, we may couple directly to a one-particle density of states in the normal layer and we lose the signature of the superconductor at once.

2.2.3 Double barrier junction

In the study of normal versus superconducting junctions, it is of interest to investigate the impact the quantum coherence has on the macroscopic limit of transport (limit of an infinite number of channels) and, in particular, to compare the behavior of a specific scattering region connected to either a normal or a superconducting

reservoir. We consider an insulator–normal-metal–insulator (X=INI) interferometer which we connect to normal leads in a NININ junction and to a superconducting lead in a NINIS junction. Besides the intrinsic interest in the double barrier system as a paradigm, now to be combined with a superconductor, it may also serve as a qualitative model for a disordered conductor, due to its strong similarity in the transmission distribution [Dorokhov 1982, Melsen 1994]. As we consider voltages below the superconducting gap, we typically chose the thickness of the interlayer to be $d \gg \hbar v_F / \Delta$.

The resonance structure of the INI interferometer results in a bimodal distribution of its (overall) transmission probabilities T . For symmetric barriers it takes the form (infinite channel limit, $T_1 = T_2 \ll 1$) [de Jong 1997],

$$\rho(T) = \frac{1}{\pi} \frac{T_1}{2} \frac{1}{\sqrt{T^3(1-T)}}, \quad T \in \left[\frac{T_1^2}{\pi^2}, 1 \right], \quad (2.33)$$

which has its analog in a disordered conductor [Dorokhov 1982, Melsen 1994]. We recall that, in a NININ junction, the rich structure of this distribution has no impact on the macroscopic transport properties. The (linear) conductance and shot noise may be evaluated from the bimodal distribution (2.33), $(h/2e^2)G = \int dT \rho(T) T = T_1/2$, $(h/2e^3)S = \int dT \rho(T) T(1-T) = T_1/4$, and show no characteristics of coherent transport [Chen 1991]. The conductance follows from the series resistance of the two barriers, and an incoherent model of a double barrier junction gives the same suppressed noise $S/eG = 1/2$ as a consequence of charge conservation [Beenakker 1992b]. When considering the INI interferometer in a NINIS junction instead, we find a non-trivial answer, both at small and large voltages. The *linear* response follows from Eqs. (2.15), (2.28), and (2.33),

$$\begin{aligned} \frac{h}{2e^2}G(0) &= \int dT \rho(T) \frac{2T^2}{(2-T)^2} = \frac{T_1}{2} \frac{1}{\sqrt{2}}, \\ \frac{h}{2e^3}S(0) &= \int dT \rho(T) \frac{16T^2(1-T)}{(2-T)^4} = \frac{T_1}{2} \frac{3}{4\sqrt{2}}. \end{aligned} \quad (2.34)$$

The ratio of shot noise to conductance is [de Jong 1997] $S(0)/eG(0) = 3/4$. A comparison of the shot noise to conductance ratios in a single barrier junction (X=I or X=IN) and a junction with disorder (X=D) is instructive, see Table 1. In the single barrier junction the distribution of transmissions is peaked at $T \ll 1$. The noise is due to the Schottky type fluctuations in nearly closed channels, and consequently the noise ratios $S_N/eG_N = 1$ in the NIN and $S_S/eG_S = 2$ in the NIS junction differ only by the charge quanta involved. In a junction with disorder, the noise-to-conductance ratio is also doubled for the NDS case, see Table 1. However, since in the bimodal distribution of the transmissions the noise is produced by the channels with intermediate transmission $0 < T < 1$ and the current by the open

channels with $T \rightarrow 1$, the doubling is a non-generic and thus yet unexplained feature. This is demonstrated by the noise-to-conductance ratio of $3/4$ in the NINIS as compared to $1/2$ in the NININ junction.

Table 2.1: Shot noise to conductance ratio S/eG of a NXN compared to a NXS junction; single barrier $X = I$, double barrier $X = INI$, disorder $X = D$. The results are valid for small transmissions $T \ll 1$, and many channels ($N \rightarrow \infty$) [Khlus 1987, de Jong 1997, Chen 1991, Beenakker 1992b].

	single barrier $T \ll 1$	double barrier $T_1 = T_2 \ll 1$	disorder
S_N/eG_N	1	$1/2$	$1/3$
S_S/eG_S	2	$3/4$	$2/3$

At *finite* voltage, the shot noise is described by Eq. (2.28) with the reflection amplitudes $r_\nu(\pm\epsilon) = r_2 + t_2^2 r_1 e^{2ik_\nu(\pm\epsilon)d} / (1 - r_1 r_2 e^{2ik_\nu(\pm\epsilon)d})$ of the double barrier interferometer. We have evaluated this expression for a symmetric double barrier junction ($T_1 = T_2 = 0.05$) and display the results in Fig. 2.5. At voltages of the order of the Andreev levels $eV \sim v_F/d$, we find a resonance structure independent of the number of channels. We observe again that the differential noise follows the resonance peaks of the conductance. At large voltages ($eV \gg v_F/d$), the resonances disappear as the electrons and holes dephase, and we approach the regime where the conductance and shot noise become indistinguishable from the incoherent addition of the NIN and NIS junctions.

2.2.4 Discussion

In conclusion, we have expressed the differential shot noise in a disordered NXS junction in Eq. (2.28) in terms of the normal and Andreev scattering amplitudes. We have described the resonance structure in the shot noise found at finite voltage in coherent transport. The robustness of the resonance structure in the multichannel limit is owed to its pinning to the Fermi energy. We have pointed out the possibility of a non-trivial normal versus superconducting noise ratio in the NINIS junction as as consequence of the bimodal distribution. Finally, we have found a rapid decay of double shot noise in a NINS junction above the Andreev minigap.

Chapter 3

Magnetic response of a normal-metal – superconductor structure: Nonlocality

3.1 Introduction

In this chapter we turn to the magnetic response of a normal metal in proximity to a superconductor. While the transport experiments discussed in Chapter 2 probe the Andreev quasi-particles in an out-of-equilibrium situation, which is kept up by the voltage difference across the leads, the magnetic screening is a thermodynamic property of the condensate wavefunction. Induced superconductivity, in fact, does not necessarily imply supercurrents. Though the Andreev reflection may enhance the conductance in a normal-metal – superconductor junction, the transport currents remain nevertheless dissipative. In the response to an applied magnetic field considered here, however, the Andreev quasi-particles produce diamagnetic supercurrents. The magnetism is a property of the $H - T$ phase diagram of the proximity system.

Here we study the linear current response to an applied magnetic field. Combined with the self-consistent solution of the Maxwell equation this allows to describe the diamagnetic phase of the $H - T$ phase diagram. To be specific, we consider an normal-metal slab of thickness d in contact with a bulk superconductor, as shown in Fig. 3.1. The pioneering works in the magnetic response of hybrid NS structures go back to the Orsay Group [de Gennes 1964, de Gennes 1966b]. Using the Ginsburg-Landau (GL) equations for superconductivity, see [de Gennes 1966b, Geshkenbein 1988], they gained a good understanding of the rich phenomenology of these mostly dirty thin film systems. The normal metal in proximity showed an increasingly diamagnetic response with decreasing temperature, eventually ap-

proaching a perfect Meissner-Ochsenfeld effect [Meissner 1933]. Although they obtained the correct qualitative picture, the GL equations were pushed beyond their strict domain of validity. The progress in the fabrication technology opened the way for interesting experiments on increasingly clean NS proximity systems in the last two decades [Oda 1980, Mota 1982, Bergmann 1987, Mota 1989, Visani 1990a, Mota 1994, Onoe 1995]. Their quantitative understanding requires a more accurate microscopic description. Most importantly for this thesis was an astonishing finding made by Mota and co-workers [Visani 1990a] in the low-temperature behavior of normal-metal coated superconducting cylinders. These Ag-Nb cylinders were shown to exhibit a paramagnetic signal on top of the diamagnetic susceptibility. Before a closer analysis of this fascinating experiment became possible — we will return to it in Chapter 5 — a quantitative analysis of their experimental data at higher temperature was needed for a characterization of the sample with respect to the proximity contact and the impurity concentration. In fact, the theory by [de Gennes 1966b] could not give an quantitative description of the usual diamagnetic behavior. The work described in this chapter has laid the basis for this understanding, tracing the screening behavior back to the non-locality of the current-field relations shown to be typical for the proximity effect.

A mile-stone in the theoretical development was the work by Zaikin [Zaikin 1982] on the magnetic response of a clean normal-metal proximity layer. Applying the quasi-classical Green's function technique to this problem, he demonstrated the power of this approach, which has been predominantly used since [Narikiyo 1989, Higashitani 1995, Belzig 1996a]. Section 3.2 is devoted to the quasi-classical technique in the proximity effect. Zaikin found a non-local current-field dependence in this system, which exhibits a similarity to the Pippard equation [Pippard 1953]. In section 3.3 we derive the general linear response kernel for a NS sandwich with an arbitrary impurity concentration. We find that the clean limit represents just one facet of the typical nonlocal constitutive relation in the proximity effect. The rich phenomenology is due to the self-consistency with the Maxwell equations required by the screening problem. In section 3.4, we study the sensitivity of the nonlocality to the presence of impurities. The superfluid density and the range of the current-field relations, both diminishing with decreasing mean free path, are shown to affect the screening ability in a contrary way and compete in the magnetic response.

3.2 Quasi-classical equations and proximity effect

3.2.1 Eilenberger equation

The basic set of equations appropriate for describing spatially inhomogeneous superconductors was developed by Eilenberger [Eilenberger 1968] and by Larkin and

Ovchinnikov [Larkin 1968]. Starting from the widely used field theoretic method for superconductivity, see [Abrikosov 1975, Rickayzen 1980, Mahan 1990], by averaging over the oscillations on the scale of the Fermi wavelength, a quasi-classical Green's function is obtained, which retains the full information on the length scales of interest: the coherence length and the field penetration depth. The 2×2 matrix Green's function $\hat{g} = \hat{g}_{\omega_n}(\mathbf{x}, \mathbf{v}_F)$,

$$\hat{g} = \begin{pmatrix} g & f \\ f^\dagger & -g \end{pmatrix}, \quad (3.1)$$

satisfies the Eilenberger equation¹

$$-(\mathbf{v}_F \cdot \nabla) \hat{g}_{\omega_n}(\mathbf{x}, \mathbf{v}_F) = [(\omega_n + ie\mathbf{v}_F \cdot \mathbf{A}(\mathbf{x})) \hat{\tau}_3 + \hat{\sigma}_{\omega_n}(\mathbf{x}), \hat{g}_{\omega_n}(\mathbf{x}, \mathbf{v}_F)], \quad (3.2)$$

with the normalization condition $\hat{g}^2 = 1$. Here $g = g_{\omega_n}(\mathbf{x}, \mathbf{v}_F)$ is the normal- and $f = f_{\omega_n}(\mathbf{x}, \mathbf{v}_F)$, $f^\dagger = f_{\omega_n}^\dagger(\mathbf{x}, \mathbf{v}_F)$ are the anomalous Green's functions, depending on the Matsubara frequency $\omega_n = (2n+1)\pi T$ ($n = 0, \pm 1, \dots$), the center-of-mass coordinate \mathbf{x} , and the direction of the Fermi velocity \mathbf{v}_F ($\hat{\tau}_i$ denote the Pauli matrices, $[\cdot, \cdot]$ is the commutator). The Eilenberger equation allows to describe spatially inhomogeneous superconductors in equilibrium. The self-energy $\hat{\sigma} = \hat{\sigma}^{(s)} + \hat{\sigma}^{(i)} + \dots$ contains the off-diagonal pair potential

$$\hat{\sigma}_{\omega_n}^{(s)}(\mathbf{x}) = \begin{pmatrix} 0 & \Delta(\mathbf{x}) \\ \Delta(\mathbf{x})^* & 0 \end{pmatrix}, \quad (3.3)$$

as well as other contributions from impurity scattering or higher order electron-electron interactions. The quasi-classical technique represents a self-contained formalism, i.e., the self-energies can be expressed through the quasi-classical Green's functions themselves. Below we use the impurity scattering self-energy in the Born limit,

$$\hat{\sigma}_{\omega_n}^{(i)}(\mathbf{x}) = \frac{1}{2\tau} \langle \hat{g}_{\omega_n}(\mathbf{x}, \mathbf{v}_F) \rangle, \quad (3.4)$$

where τ the scattering time and $\langle \dots \rangle$ denotes the angular average $\int d\Omega/4\pi(\dots)$ over \mathbf{v}_F . The order parameter is self-consistently determined by ($N_0 = mk_F/\hbar^2\pi^2$)

$$\Delta(\mathbf{x}) = -VN_0\pi T \sum_{\omega_n > 0} \langle f_{\omega_n}(\mathbf{x}, \mathbf{v}_F) \rangle, \quad (3.5)$$

where $V < 0$ describes the effective coupling constant for the attractive electron-electron interaction. The systems of Eqs. (3.2) and (3.5) are completed by the quasi-classical current expression,

$$\mathbf{j}(\mathbf{x}) = 2ieN_0\pi T \sum_{\omega_n > 0} \langle \mathbf{v}_F g_{\omega_n}(\mathbf{x}, \mathbf{v}_F) \rangle. \quad (3.6)$$

¹ $e = |e|$, $\hbar = k_B = c = 1$ throughout this thesis.

In the Gorkov formalism [Abrikosov 1975] the current is separated into a diamagnetic and a paramagnetic contribution. Eq. (3.6) contains both contributions, even if it is formally similar to the paramagnetic current in terms of the Gorkov-type Green's function. This is due to the renormalization procedure used in the quasi-classical theory and is explained in appendix B.

The Eilenberger equation is valid on all length scales ζ with $k_F\zeta \gg 1$, and for magnetic fields such that the Larmor radius $r_L = \hbar k_F c / eH$ exceeds the involved length scale $r_L \gg \zeta$ (r_L being the cyclotron radius of a particle with Fermi velocity). The quasi-classical Green's functions need to be supplemented by a set of boundary conditions [Zaitsev 1984, Kieselmann 1987, Hara 1993], because they are not continuous at the interfaces of different materials. For more details on the derivation, the symmetries and the validity of the Eilenberger equations, we refer the reader to appendix B and several reviews on the subject [Serene 1983, Shelankov 1985, Rammer 1986, Kopnin 1997].

Let us illustrate the use of the quasi-classical equations for the simple case of a homogeneous superconductor. The Green's function takes the form

$$\hat{g} = \frac{1}{\Omega_n} \begin{pmatrix} \omega_n & \Delta \\ \Delta & -\omega_n \end{pmatrix}, \quad (3.7)$$

where $\Omega_n = \sqrt{\omega_n^2 + \Delta^2}$ ($\omega_n > 0$). Eq. (3.5) yields the usual gap equation for the superconductor. Within a field $\mathbf{A}(\mathbf{x})$ the solution of (3.2) is found by substituting $\omega_n \rightarrow \omega_n + ie\mathbf{v}_F \cdot \mathbf{A}(\mathbf{x})$ in (3.7), assuming a slow variation of the field on the scale $\lambda \gg \xi_0$ larger than the superconducting coherence length $\xi_0 = \hbar v_F / 2\Delta$. The current-field relation that follows from Eq. (3.6),

$$\mathbf{j}(\mathbf{x}) = -\frac{n_s e^2}{mc} \mathbf{A}(\mathbf{x}), \quad (3.8)$$

is the local London relation with the superconducting density

$$n_s = \frac{k_F^3}{3\pi^2} \pi T \sum_{\omega_n > 0} \frac{\Delta^2}{(\Delta^2 + \omega_n^2)^{3/2}}, \quad (3.9)$$

approaching the full electron density $n = k_F^3 / 3\pi^2$ for $T \rightarrow 0$. In the limit of vanishing superconductivity $\Delta \rightarrow 0$ we recover the trivial Green's function for the normal metal $\hat{g} = \tau_3$, and the current expression vanishes. In the following section we apply the quasi-classical formalism to the proximity effect in a normal metal slab.

3.2.2 Clean NS slab

In this chapter, we consider a normal-metal slab in contact with a bulk superconductor, see Fig. 3.1. The normal layer ($0 < x < d$) is described within the

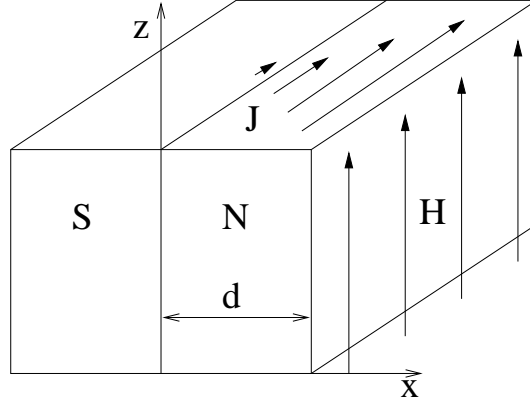


Figure 3.1: Normal-metal layer (thickness d) in proximity to a bulk superconductor. A magnetic field \mathbf{H} parallel to the surface is applied, driving screening current \mathbf{j} along the surface. Current and fields are inhomogeneous in x -direction.

free electron gas approximation. We assume a perfect contact between the metal and the superconductor as well as a specularly reflecting metal boundary. A magnetic field $(0, 0, H)$ is applied parallel to the metal surface, driving screening currents $(0, j_y(x), 0)$ along the surface. The magnetic induction is described by the vector potential $(0, A_y(x), 0)$. Taking a thickness $d \gg \xi_0$, we can neglect the self-consistency of the pair potential, and approximate the order parameter by a step function $\Delta(x) = \Delta\Theta(-x)$.

The relevant length scales in the system are given by the geometric thickness d , the thermal coherence length $\xi_N(T) = \hbar v_F / 2\pi T$, and the elastic mean free path $l = v_F \tau$. The thermal length describes the distance over which quasi-particle excitations in a typical energy interval given by the temperature T are mutually dephased. The above length scales correspond to the respective energy scales $T_A = \hbar v_F / d$ of the Andreev levels, the temperature T and the impurity self-energy \hbar / τ , all present in the Eilenberger equation (3.2). In the following we first consider a clean NS slab, i.e. the electrons propagate ballistically between the NS interface and the metal-vacuum boundary ($\tau \rightarrow \infty$). The Green's functions in the normal layer, in the low temperature limit $T_A \ll \Delta$ of interest, take the form [Zaikin 1982]

$$\begin{aligned} g &= \tanh \chi(d), \\ f &= \frac{\exp[\text{sgn}(v_x)\chi(d-x)]}{\cosh \chi(d)}, \end{aligned} \quad (3.10)$$

where $\text{sgn}(v_x) = v_x / |v_x|$

$$\chi(x) = \frac{2\omega_n x}{|v_x|} + i \frac{2ev_y}{|v_x|} \int_0^x dx' A_y(x'), \quad (3.11)$$

($\omega_n > 0$). The normal Green's function is constant as a signature of the extent of the quasi-particle over the whole normal layer. Carrying out the analytical continuation $\omega_n \rightarrow -iE + 0$ and determining the poles of $g(E)$ yields the energies of the Andreev states bound to the normal layer,

$$E_n = \frac{|v_x|\pi}{2d} \left(n + \frac{1}{2}\right) - e \frac{v_y}{d} \int_0^d dx' A_y(x'), \quad n = 0, 1, \dots \quad (3.12)$$

We recover the energies of Eq. (2.19) of the previous chapter (in the limit $T_A \ll \Delta$), which are split in direction $\pm v_y$ and shifted by the vector potential. Note the non-local field dependence of the bound state energies.

From the anomalous Green's function we can derive the pair correlation function $F(x) = i\langle \hat{\Psi}_\downarrow(x) \hat{\Psi}_\uparrow(x) \rangle$ which satisfies $\Delta(x) = -VF(x)$,

$$F(x) = N_0 \pi T \sum_{\omega_n > 0} \langle f_{\omega_n}(x, \mathbf{v}_F) \rangle. \quad (3.13)$$

We consider the case in the absence of fields $A_y = 0$ here. Neglecting the effect of the boundary at $x = d$ we find

$$F(x) \approx N_0 \frac{v_F}{x} e^{-x/\xi_N(T)}. \quad (3.14)$$

At high temperatures $T \gg T_A$, only the first Matsubara frequency $\omega_0 = \pi T$ contributes to the sum (3.13), $F \sim \exp -x/\xi_N(T)$, while at zero temperature, the decay shows no length scale, $F \sim 1/x$.

3.3 Magnetic screening

3.3.1 Linear response kernel

When studying the magnetic response, the task is to determine the current-field relation in the normal layer in functional dependence of the vector potential $\mathbf{j}[A(\mathbf{x})]$ and solve for the screening currents self-consistently with the Maxwell equation

$$-\partial_x^2 A_y(x) = 4\pi j_y(x). \quad (3.15)$$

In this chapter we focus on the magnetic response linear in the field. While the ground-state wavefunction experiences a weak perturbation that can be treated linearly, the screening of the magnetic induction is strong and requires the self-consistent solution of the Maxwell equation. Therefore the discussion of screening relies on the full knowledge of the *dispersive* response function $j(q) = K(q)A(q)$. While in a London superconductor the response $K(q) = K_0 = -c/4\pi\lambda_L^2$ is local,

implying a penetration depth $\lambda_{\text{eff}} = \lambda_L \equiv (mc^2/4\pi n_s e^2)^{1/2}$, in a Pippard superconductor with $\xi_0 > \lambda$ [Tinkham 1996] with $K(q) \approx K_0/(1+q\xi_0)$ the nonlocal response changes the penetration depth to $\lambda_{\text{eff}} = \sqrt[3]{\lambda_L^2 \xi_0} > \lambda_L$. Here we derive the current response in functional dependence of the field for the NS slab geometry. We find that the current response in the proximity effect is nonlocal in general.

The current functional linear in $A(x)$ takes the generic form

$$j_y(x) = - \int K(x, x') A_y(x') dx' \quad (3.16)$$

of a convolution with the response kernel $K(x, x')$. In the following we derive $K(x, x')$ for the NS sandwich shown in Fig. 3.1, expressing it through the Green's function in absence of fields \hat{g}_0 . Inserting the appropriate Green's function \hat{g}_0 , we are able to describe the current in a normal metal layer with arbitrary impurity concentration, ranging from the clean to the dirty limit. To calculate the linear diamagnetic response, we separate the Green's function into a (real) zeroth order part and an (imaginary) first order part in $A(x)$ (we drop the Matsubara index ω_n in the following),

$$\hat{g}(\mathbf{x}, \mathbf{v}_F) = \hat{g}_0(x, v_x) + i\hat{g}_1(x, v_x, v_y). \quad (3.17)$$

In the absence of external fields Eq. (3.2) reduces to

$$\begin{aligned} -v_x \partial_x g_0(x, v_x) &= \tilde{\Delta}(x) [f_0(x, v_x) - f_0^\dagger(x, v_x)] \\ -v_x \partial_x f_0(x, v_x) &= 2\tilde{\omega}(x) f_0(x, v_x) - 2\tilde{\Delta}(x) g_0(x, v_x) \\ v_x \partial_x f_0^\dagger(x, v_x) &= 2\tilde{\omega}(x) f_0^\dagger(x, v_x) - 2\tilde{\Delta}(x) g_0(x, v_x). \end{aligned} \quad (3.18)$$

We have introduced the effective frequency $\tilde{\omega}(x) = \omega + \langle g_0(x) \rangle / 2\tau$ and pair potential $\tilde{\Delta}(x) = \Delta(x) + \langle f_0(x) \rangle / 2\tau$ as diagonal and off-diagonal potentials, respectively. Equations (3.18) imply that $f_0(x, v_x) = f_0^\dagger(x, -v_x)$, as $\tilde{\Delta}$ has been chosen real. We consider the solution of Eqs. (3.18) as given in the following. The first-order parts obey the equations

$$\begin{aligned} -v_x \partial_x f_1(x, v_x, v_y) &= 2\tilde{\omega}(x) f_1(x, v_x, v_y) - 2\tilde{\Delta}(x) g_1(x, v_x, v_y) \\ &\quad + 2ev_y A_y(x) f_0(x, v_x), \end{aligned} \quad (3.19)$$

$$\begin{aligned} v_x \partial_x f_1^\dagger(x, v_x, v_y) &= 2\tilde{\omega}(x) f_1^\dagger(x, v_x, v_y) - 2\tilde{\Delta}(x) g_1(x, v_x, v_y) \\ &\quad + 2ev_y A_y(x) f_0^\dagger(x, v_x), \end{aligned} \quad (3.20)$$

where $g_1 = (f_0 f_1^\dagger + f_1 f_0^\dagger) / 2g_0$ follows from the normalization $\hat{g}^2 = 1$. Eqs. (3.19) and (3.20) can be mapped to two uncoupled Riccati equations and integrated out formally in terms of g_0 , f_0 , and f_0^\dagger . Determining the current (3.6) we have extracted

the kernel $K(x, x')$ appearing in (3.16). The derivation of the results given here is deferred to Appendix C, see also [Belzig 1998]. Introducing a 'propagator'

$$m(v_x, x, x') = \exp \left(\frac{2}{v_x} \int_x^{x'} \frac{\tilde{\Delta}(x'')}{f_0^\dagger(x'', v_x)} dx'' \right), \quad (3.21)$$

with the properties $m(v_x, x, x') = m(v_x, x', x)^{-1}$ and $m(v_x, x, x'')m(v_x, x'', x') = m(v_x, x, x')$, the linear response kernel takes the form

$$K(x, x') = e^2 v_F N_0 \pi T \sum_{\omega_n > 0} \int_0^{v_F} du \frac{1 - u^2/v_F^2}{u} [1 + g_0(x, u)] [1 - g_0(x', u)] \quad (3.22)$$

$$\left[\Theta(x - x') m(u, x, x') + \Theta(x' - x) m(-u, x, x') + m(-u, x, d) m(u, d, x') \right].$$

The propagator (3.21) determines the ratio of the current response at x to the field at x' , thus containing the range of the current-field relations. The inverse decay length of the propagator is proportional to the off-diagonal part of the self-energy $\tilde{\Delta}$. The factor $1 - g_0$ is a measure of the superfluid density, vanishing in the normal state $g_0 = 1$. The three summands in (3.22) stem from the quasi-particle trajectories connecting x and x' , either directly or by one reflection at the normal-metal boundary.

For illustration we reproduce the current response of a half-infinite superconductor. Setting $d = 0$ the solution of the Eilenberger equation (3.18) takes the simple form $g_0 = \omega_n/\Omega_n$, $f_0 = f_0^\dagger = \Delta/\Omega_n$, where $\Omega_n = (\Delta^2 + \omega_n^2)^{1/2}$, see (3.7). Inserting in (3.22) we obtain the linear-response kernel

$$K_S(x, x') = e^2 v_F N_0 \pi T \sum_{\omega_n > 0} \frac{\Delta^2}{\Omega_n^2} \int_0^{v_F} du \frac{1 - u^2/v_F^2}{u} \quad (3.23)$$

$$\left[e^{-(2\Omega_n + 1/\tau) \frac{|x - x'|}{u}} + e^{(2\Omega_n + 1/\tau) \frac{x + x'}{u}} \right],$$

which describes the current response of a superconductor with arbitrary impurity concentration [Abrikosov 1975], which here additionally includes the effect of the boundary. For fields varying rapidly spatially we arrive at a non-local current-field relation of the Pippard-type [Pippard 1953], while for slowly varying fields the kernel can be integrated out in Eq. (3.16), producing the local result (3.8). We recall here certain generic features of this kernel, which are of importance below. In a clean superconductor ($1/\tau \ll \Delta$), the range is given by the superconducting coherence length ξ_0 , while in a dirty superconductor ($\Delta \ll 1/\tau$) the range is given by the mean free path $l = v_F \tau$, and is thus in both cases (nearly) temperature independent. We discuss below how, in the proximity effect, the range of the kernel varies from infinity to l and $\xi_N(T)$, exhibiting a strong temperature dependence, which leads to non-trivial screening properties.

3.3.2 Clean limit

The linear response in the clean NS slab illustrates the nonlocality of the current–field relation in the proximity effect. Inserting the clean limit solution (3.10) (with $A = 0$) into (3.22), we obtain straightforwardly [Zaikin 1982],

$$j_y = -\frac{1}{4\pi\lambda^2(T)d} \int_0^d A(x) dx. \quad (3.24)$$

The temperature-dependent penetration depth that is given explicitly by

$$\frac{1}{\lambda_N^2(T)} = \begin{cases} \frac{4\pi e^2 n}{mc^2} \equiv \frac{1}{\lambda_N^2}, & T = 0 \\ \frac{6T_A}{\lambda_N^2 T} e^{-2T/T_A}, & T \gg T_A. \end{cases} \quad (3.25)$$

Here $n = k_F^3/3\pi^2$ is the normal electron density producing the London length typically $\lambda_N \ll d$. The propagator trivially becomes $m(v_x, x, x') = 1$ implying an infinite kernel range. Interestingly, the thermal length $\xi_N(T)$ does not enter the kernel, as one might expect from the analogy to a clean superconductor with range ξ_0 . The spatial extent of the current–field dependence is thus cut off by the geometry $0 < x < d$. Eq. (3.24) produces a constant current over the normal-metal layer, depending on the average vector potential. Solving Maxwell’s equation (3.15) with the boundary conditions $A_y(x=0) = 0$ (perfect superconductor) and $\partial_x A_y(x=d) = H$ (applied magnetic field), we easily find for $\lambda_N(T) \ll d$,

$$\begin{aligned} j_y(x) &\approx -\frac{3H}{8\pi d}, \\ B_z(x) &\approx \frac{3H}{2d}x - \frac{H}{2}, \\ A_y(x) &\approx -\frac{H}{2}x + \frac{3H}{4d}x^2. \end{aligned} \quad (3.26)$$

The current $j \sim H/d$ screens the applied field on the geometric scale d . The magnetic induction B changes sign inside the normal metal approaching $B(x=0) = -H/2$ at the NS interface: the field is overscreened. While the screening currents minimize the average vector potential to

$$\frac{1}{d} \int_0^d A(x') dx' \sim Hd \frac{\lambda_N^2(T)}{d^2}, \quad (3.27)$$

the average magnetization

$$4\pi M = \frac{A(d)}{d} - H \approx -\frac{3}{4}H, \quad (3.28)$$

makes up only 3/4 of the value for an ideal diamagnet. Thus the nonlocality results in a less efficient expulsion of the applied field, with overscreening as its signature. Overscreening is observed at low temperature, as long as $\lambda_N(T) \ll d$, the diamagnetic susceptibility leveling off at $4\pi\chi = M/H \approx -3/4$. At high temperatures the susceptibility is suppressed exponentially,

$$4\pi\chi = -\frac{d^2}{4\lambda_N^2(T)} \sim e^{-2T/T_A}, \quad (3.29)$$

see Fig. 3.2 (clean limit).

3.4 Sensitivity to impurities

For an arbitrary impurity concentration the screening problem has to be solved numerically. First the Green's function in the absence of fields \hat{g}_0 is determined, according to (3.18). For the discussion of a stable algorithm therefore we refer the reader to [Belzig 1999]. Second, the linear response kernel (3.22) is evaluated and solved self-consistently for $A(x)$ with Maxwell's equation. Depending on the relative size of the thermal length $\xi_N(T)$, the mean free path l , and the thickness d we distinguish various regimes of either ballistic or diffusive electron propagation which are shown in Fig. 3.3. Note that the dividing line between ballistic and diffusive behavior is not given by the simple relation $\xi_N(T) = l$ (dotted line). Rather, the range of the current-field relation $\xi_N(T)$, l , or ∞ is needed for an accurate characterization of the magnetic response. The numerical results for the magnetic susceptibility $4\pi\chi$ as a function of temperature are shown in Fig. 3.2. The different curves show the clean limit and the mean free paths $l/d = 10^4, 10, 1, 0.1$. Clearly, a finite impurity concentration has a strong influence on the susceptibility, even if $l > d$, and can either increase or decrease the diamagnetic screening, depending on temperature. In the following, we explain Figs. 3.2 and 3.3 in detail.

3.4.1 Ballistic regime

The ballistic regime is limited by $l \gg \min\{d, \xi_N(T)\}$, which ensures a ballistic propagation of the electrons over the thickness or the thermal length of the normal layer, respectively. As a limiting case, we have already considered the clean limit ($l \rightarrow \infty$).

An estimation using the zeroth order Eilenberger equation Eq. (3.18) easily shows that the clean-limit solution (3.10) remains valid in the absence of fields for

$$l \gg d \exp(2d/\xi_N(T)), \quad \text{if} \quad \xi_N(T) \ll d, \quad (3.30)$$

$$l \gg d, \quad \text{if} \quad \xi_N(T) \gg d, \quad (3.31)$$

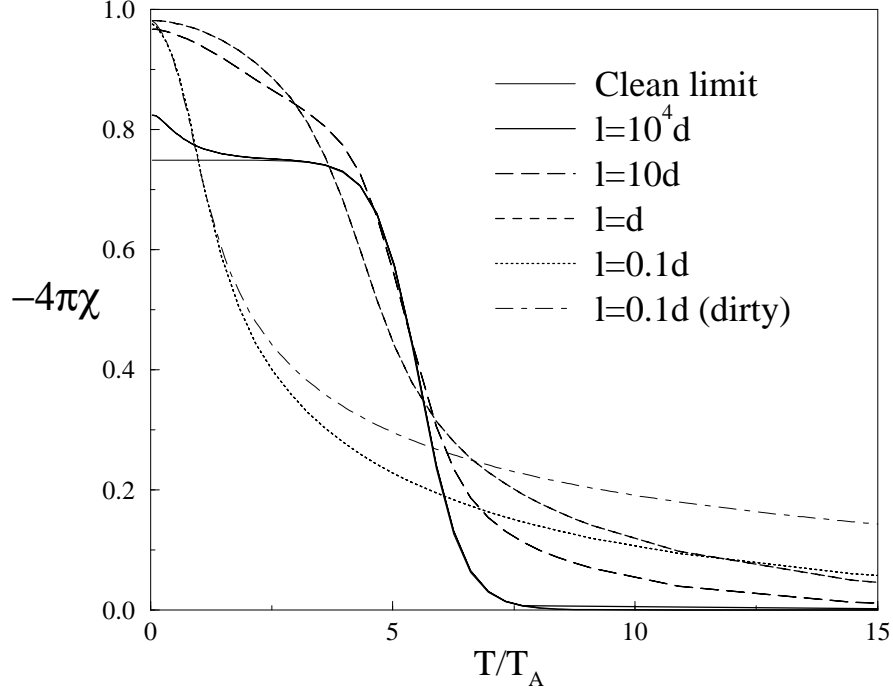


Figure 3.2: Numerical results for diamagnetic susceptibility $4\pi\chi$ of the normal metal layer ($\lambda_N = 0.003d$). The clean limit is indicated by a thin line saturating at $4\pi\chi = -0.75$ for $T < 5T_A$. The low temperature screening is enhanced by a finite mean free path $l > d$ by reducing the kernel range from ∞ to l . Similarly, the high temperature signal is enhanced with decreasing mean free path. As $l < d$, the superfluid (screening) density is reduced, suppressing the diamagnetic susceptibility at all temperatures. The dirty limit is shown to overestimate the screening at large temperature.

see Fig. 3.3. Note that this includes the region $d \ll l \ll \xi_N(T)$, the finite thickness preventing the small mean free path $l \ll \xi_N(T)$ from becoming effective. In the evaluation of the kernel, the off-diagonal potential $\tilde{\Delta} = \langle f_0 \rangle / 2\tau$ enters the propagator (3.21), yielding the kernel (3.22), which approximately takes the form

$$K(x, x') = \frac{1}{8\pi\lambda^2(T)d} \left[e^{-\frac{|x-x'|}{l}} + e^{-\frac{2d-x-x'}{l}} \right]. \quad (3.32)$$

Since $l \gg d$, the exponentials may be expanded to first order. As a result, we obtain two contributions to the current $j = j_{\text{clean}} + j_{\text{imp}}$

$$j_{\text{clean}} = \frac{-1}{4\pi\lambda^2(T)d} \int_0^d A(x) dx, \quad (3.33)$$

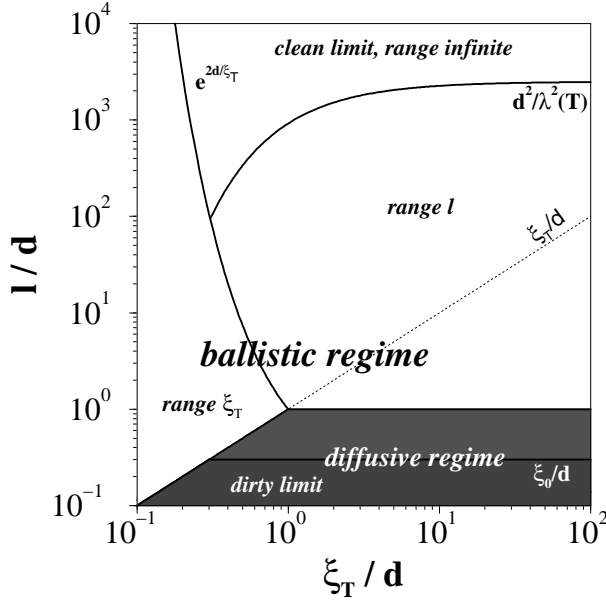


Figure 3.3: Dependence of the magnetic response on thermal length $\xi_N(T) = v_F/2\pi T$ and mean free path l . In the ballistic regime $l \gg \min\{d, \xi_N(T)\}$ we distinguish three regions: (a) the clean limit with infinite range of the kernel exhibiting a reduced diamagnetism (overscreening), (b) the quasi-ballistic limit with finite range $\xi_N(T)$ increasing screening at large temperatures, (c) the ballistic limit where the finite range l enhances the screening although $l \gg d$. In the diffusive regime $l \ll \xi_N(T), d$ the range of the kernel is given by l . The dirty limit with nearly isotropic Green's functions is restricted to $l \ll \xi_0, \xi_N(T), d$. Note that the current-field relations can still be local or non-local depending on the relative size of penetration depth and mean free path.

$$j_{\text{imp}}(x) = \frac{1}{8\pi\lambda^2(T)d} \int_0^d \frac{|x-x'| + 2d - x - x'}{l} A(x') dx'. \quad (3.34)$$

According to (3.27) solving the screening problem in the clean limit, we find $j_{\text{clean}} \sim H/d$. Taking (3.34) as a small perturbation, we obtain $j_{\text{imp}} \sim Hd^2/\lambda_N^2(T)l$, which becomes of the same order of magnitude as j_{clean} if

$$l \sim d \frac{d^2}{\lambda_N^2(T)}. \quad (3.35)$$

As long as $l \gg d^3/\lambda_N^2(T)$, the range of the kernel is effectively ∞ and the clean limit applies, see Fig. 3.3. As $l < d^3/\lambda_N^2(T)$ — which is the case for $l \gg d$ in general —

the mean free path l enters the kernel range, as shown in Fig. 3.3. The diamagnetic susceptibility is enhanced at low temperature ($\xi_N(T) \gg d$), as Fig. 3.2 ($l = 10^4 d$) illustrates. The screening currents are even sensitive to a mean free path $l \ll d$. The applied field is found to be screened on the effective penetration depth

$$\lambda_{\text{eff}} \equiv \sqrt[3]{\lambda^2(T)l} < d, \quad (3.36)$$

in analogy to the effective penetration depth of a Pippard superconductor $\lambda_{\text{eff}} = \sqrt[3]{\lambda_N^2(T)\xi_0}$, see e.g. [Tinkham 1996].

In the remaining part of the ballistic regime, see Fig. 3.3 (range $\xi_N(T)$), the full solution is not known analytically, but we may produce an approximate solution, which characterizes well the numerical results at high temperature ($\xi_N(T) \ll d$). Limiting ourselves to high temperature with $\xi_N(T) \ll d$ allows us to consider the Green's function for the first Matsubara frequency $\omega_0 = \pi T$ only. We restrict ourselves to the forward direction $v_x = +v_F$. From Eq. (3.18) we find that $f_0(v_F) \approx 2 \exp(-x/\xi_N(T))$ remains unchanged as in (3.10), and $f_0^\dagger(v_F) \ll 1$ and $1 - g_0(v_F) \ll 1$ obey the approximate equations,

$$\begin{aligned} \left(\frac{d}{dx} - \frac{1}{\xi_N(T)} \right) f_0^\dagger(x, v_F) &= -\frac{1}{l} \langle f_0(x) \rangle \\ \frac{d}{dx} (1 - g_0(x, v_F)) &= -\frac{1}{l} \langle f_0(x) \rangle f_0(x, v_F) \end{aligned} \quad (3.37)$$

with the solutions

$$f_0^\dagger(x, v_F) = \frac{\xi_N(T)}{2l} e^{-x/\xi_N(T)} \quad (3.38)$$

$$1 - g_0(x, v_F) = \frac{\xi_N(T)}{2l} e^{-2x/\xi_N(T)} \quad (3.39)$$

Here we have used $\langle f_0 \rangle \approx f_0(v_F)/2$. $f_0^\dagger(v_F)$ and $1 - g_0(v_F)$ are of order $\xi_N(T)/l$ rather than exponentially suppressed $f_0^\dagger \sim \exp -d/\xi_N(T)$, $1 - g_0 \sim \exp -2d/\xi_N(T)$ as in the clean limit (3.10). The correction to g_0 given by Eq. (3.39) increases the superfluid density in the vicinity of the superconductor via the factor $1 - g_0$ in the kernel. The range of the propagator is modified by the correction (3.38) to f^\dagger , leading to

$$m(v_F, x, x') \approx \exp \left(2 \frac{x' - x}{\xi_N(T)} \right). \quad (3.40)$$

The range of the kernel is now given by $\xi_N(T)$, which is strongly temperature dependent, and the current flows in a layer of thickness $\xi_N(T)$ close to the NS interface,

$$j(x) \approx -\frac{1}{\lambda_N^2 l} \int_0^d dx' e^{-2 \frac{x'+|x-x'|}{\xi_N(T)}} A(x'). \quad (3.41)$$

Thus in the high temperature limit of Fig. 3.2, as the mean free path l becomes smaller the diamagnetic susceptibility is enhanced.

3.4.2 Diffusive regime

If impurity scattering dominates, as described by $\langle g_0 \rangle / \tau \gg \omega$ and $\langle f_0 \rangle / \tau \gg \Delta$, Eq. (3.18) can be reduced to the Usadel equation [Usadel 1970] for the isotropic part $\langle f_0(x) \rangle$. Assuming $T \ll \Delta$ the solution in the normal metal takes the form

$$\langle f_0(x) \rangle = \cosh\left(\sqrt{\frac{2\omega}{D}}(d-x)\right) / \cosh\left(\sqrt{\frac{2\omega}{D}}d\right), \quad (3.42)$$

where $D = v_F^2 \tau / 3$ is the diffusion constant. Equation (3.42) shows that the important energy scale is the Thouless energy $E_c = D/2\pi d^2$ [Edwards 1972]. The f -function (3.42) features the decay length $\xi_D(T) = (D/2\pi T)^{1/2}$ reflecting the diffusive nature of the electron motion.

In the normal metal $l \ll \xi_N(T)$, d are necessary conditions for the Usadel theory to be valid. However, the numerical solution of (3.18) shows that the Usadel theory in the normal metal, which requires the Green's functions to be nearly isotropic, is only a good approximation for $l < \xi_0$: the dirty limit in Fig. 3.3.

Using the fact that the zeroth-order Green's function is nearly isotropic and varies on a scale $\xi_D(T) \gg l$, we find for the kernel (3.22)

$$K(x, x') = \frac{\tau}{\lambda_N^2} T \underbrace{\sum_{\omega_n > 0} \langle f_0(x) \rangle^2}_{\frac{1}{4\pi\lambda^2(x, T)}} \frac{3}{4l} \int_0^{v_F} du \frac{v_F^2 - u^2}{v_F^3 u} \left[e^{-\frac{|x-x'|}{lu}} + e^{-\frac{2d-x-x'}{lu}} \right]. \quad (3.43)$$

The prefactor contains the full temperature dependence here and defines a space dependent penetration depth $\lambda(x, T)$. Qualitatively, the range of the kernel retains the same length scale l as in the adjacent ballistic regime, while the screening density is suppressed by the impurities. In Fig. 3.2 we thus find that a small mean free path $l \ll d$ produces an overall reduction of the susceptibility.

For $\lambda(x, T) \gg l$ the vector potential may be taken out of the integral in Eq. (3.16) and after integration over the kernel we recover the well-known local current-vector potential relation used in the Usadel theory [Usadel 1970], with penetration depth $\lambda(x, T)$. We note that as long as $\lambda(x, T) < l$, although the Green's functions are nearly isotropic, and in absence of the field are given by the Usadel theory, the current response is nevertheless nonlocal. In Fig. 3.2 the magnetic susceptibility for $l = 0.1d$ is compared to the local Usadel result (dirty limit), showing that the latter overestimates the screening at high temperature.

The high temperature ($T \gg E_c$) behavior is characterized by screening limited to a layer of thickness $\xi_D(T)$ close to the superconductor, and consequently the diamagnetic susceptibility is given by

$$4\pi\chi \propto -\frac{\xi_D(T)}{d} \propto \frac{1}{\sqrt{T}}. \quad (3.44)$$

This estimate is in agreement with the Ginzburg-Landau theory [de Gennes 1966b] as well as the numerical Usadel results [Narikiyo 1989].

3.5 Discussion

There are two main differences in the observable properties of the induced screening between the clean and the dirty limit. First, the zero temperature value of the susceptibility $-4\pi\chi$ saturates at $3/4$ in the clean limit, while it reaches unity in the dirty limit. Second, the asymptotic behavior at high temperature differs: in the clean limit χ decays exponentially $\chi \propto \exp(-2T/T_A)$, while in the dirty limit it follows an algebraic law $\chi \propto T^{-1/2}$. The intermediate behavior illustrated in Fig. 3.2 is determined by the competition of the nonlocality range and the screening density. With increasing disorder, a reduction of the range from ∞ to $\xi_N(T)$ or l enhances the screening, while a reduction of the superfluid density weakens the diamagnetic currents. We have found several ballistic and diffusive regimes shown in Fig. 3.3 with different characteristics. Remarkably, due to the absence of the small scale ξ_0 in the proximity effect, the nonlocal kernel (3.22) is crucial to the understanding of all the regimes.

Our results imply a non-monotonic dependence of the diamagnetic susceptibility on the mean free path. Starting from a clean sample, with decreasing purity first the range of the linear response kernel is augmented and Meissner currents are enhanced, then the superfluid density is reduced and the screening currents are suppressed. Assuming a temperature-dependent scattering mechanism with decreasing mean free path as a function of temperature, such as electron-electron or electron-phonon interaction, we might speculate to observe a non-monotonic (i.e. re-entrant) behavior of the susceptibility (here the smallness of the scattering rate is compensated by the high sensitivity of the non-local current-field relation). However, as is evident from Eq. (3.21), the largest off-diagonal self-energy ($\tilde{\Delta}$) which includes e.g. impurity scattering will provide a (low-temperature) cutoff for this behavior.

Our results allows for a quantitative agreement with the experiments. The fit of the experimental data for the diamagnetic susceptibility gives an independent determination of the mean free path in these samples, which has been compared to the results of the resistivity measurements [Müller-Allinger 1999]. The magnetic susceptibility emerges as a sensitive indicator of the impurity concentration due to the nonlocality of the constitutive relation.

Chapter 4

Magnetic breakdown in a normal-metal – superconductor proximity structure

4.1 Introduction

In this Chapter we extend the study of magnetism from the linear response to the finite field regime. Recent experiments have demonstrated the non-trivial screening properties of hybrid normal-metal–superconductor structures, exhibiting a magnetic breakdown at finite fields [Oda 1980, Mota 1982, Bergmann 1987, Visani 1990b]. The investigated samples have typical dimensions comparable to the thermal length $\xi_N(T)$ in the normal metal, attributing a key role to the quantum coherence of the electrons coupled to the macroscopic phase of the superconductor.

We consider a clean normal-metal slab of thickness d in proximity with a superconductor, as shown in Fig. 3.1. The self-consistent study of the finite field effect in a dirty NS sandwich within the framework of the Ginsburg-Landau (GL) equation was carried out a long time ago by the Orsay group [de Gennes 1966b]. Their work has provided the first understanding of the magnetic breakdown, which denotes the breakdown of the full magnetic flux expulsion in the normal layer, in analogy to the critical field of the superconductor. A quantitative agreement of the GL results with recent experiments is not achieved, as is discussed in [Mota 1989]. This is not surprising considering the role of nonlocality in the proximity effect, the local current-field relation of the GL theory applying only to the dirty limit. The quasi-classical Green's function technique offers the possibility to describe the opposite clean limit using the Eilenberger equations [Eilenberger 1968], which we pursue here. In [Zaikin 1982] the nonlinear response in the clean limit has been obtained along these lines. Using numerical methods, in [Belzig 1996a] the non-linear

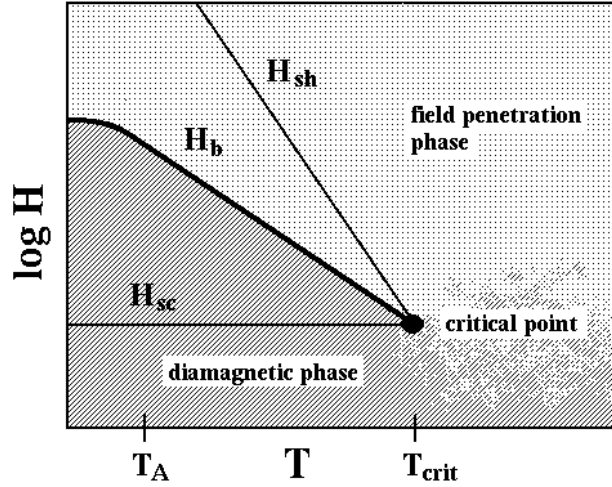


Figure 4.1: $H - T$ phase diagram of the normal metal slab of thickness d . The breakdown field $H_b(T) \sim \Phi_o/\lambda_N(T)d$ marks the first order transition between the diamagnetic and the field penetration phase ($\lambda_N(T)$ denotes the penetration depth, Φ_o the superconducting flux unit). The critical point at the intersection of the spinodals $H_{sc}(T) \sim \Phi_o/d^2$ and $H_{sh}(T) \sim \Phi_o/\lambda_N^2(T)$ separates the first order transition for $\lambda_N(T) \ll d$ from the continuous cross-over at large temperature ($\lambda_N(T) \gg d$).

field regime of the screening problem has been investigated, and the two (meta)-stable solutions in both the clean and the dirty limit have been determined (the dirty limit extends the GL results to low temperature using the Usadel equations [Usadel 1970]). In this chapter we determine the $H-T$ 'phase' diagram shown in Fig. 4.1 of the normal metal layer in the clean limit, where the bistable regime is particularly extended. In thermodynamic equilibrium, we find a magnetic breakdown at $H_b(T)$, which is a first order transition separating the phase of diamagnetic screening from the phase of magnetic field penetration. The results presented here have been published in [Fauchère 1997].

Recent experiments [Mota 1989, Mota 1994] have investigated the magnetic response of metallic cylinders with a superconducting core, finding data, which was claimed to be characteristic for the ballistic limit [Mota 1994]. This has motivated us to derive the analytic dependence of the clean limit expression for the breakdown field H_b on temperature T and thickness d of the normal layer and to compare it to the experiment. From the free energy of the normal layer, which allows us to identify the two (meta)-stable states, we determine the spinodals, the thermodynamic breakdown field $H_b(T)$ and find the jumps in magnetization and entropy at the transition. Furthermore, we obtain a critical temperature which marks the upper limit

of the bistable regime (see Fig. 4.1). Finally, we relate our results for the breakdown field to the signatures of the nonlocality in the ballistic regime as they show up in the magnetic susceptibility χ and compare them with the experimental data. The following discussion is divided into four sections: the analysis of the constitutive relations (Sec. 4.2), the solution of the magnetostatic problem (Sec. 4.3), the determination of the breakdown field from the free energy (Sec. thermodynamics), and finally the comparison with the experiment (Sec. 4.5).

4.2 Constitutive relations

The quasi-classical Green's function technique provides an appropriate description of a metal with nearly spherical Fermi surface. In a finite magnetic field, the vector potential $\mathbf{A}(\mathbf{x})$ can be included as a phase factor along unperturbed trajectories, provided the dimensions of the normal metal are smaller than the Larmor radius ($r_L = \hbar k_F c / eH$). In the ballistic limit, the quasi-classical 2×2 matrix Green's function $\hat{g}_{\omega_n}(\mathbf{x}, \mathbf{v}_F)$ satisfies the Eilenberger equation ($e = |e|$, $\hbar = k_B = c = 1$),

$$-(\mathbf{v}_F \cdot \nabla) \hat{g}_{\omega_n}(\mathbf{x}, \mathbf{v}_F) = [(\omega_n + ie\mathbf{v}_F \cdot \mathbf{A}(\mathbf{x})) \hat{\tau}_3 + \Delta(\mathbf{x}) \hat{\tau}_1, \hat{g}_{\omega_n}(\mathbf{x}, \mathbf{v}_F)], \quad (4.1)$$

discussed in Chapter 3. We exclude impurity scattering here by assuming $\tau \rightarrow \infty$.

We consider a normal metal slab of thickness d on top of a bulk superconductor as shown in the inset of Fig. 4.2. The vector potential $\mathbf{A} = (0, A(x), 0)$ describes a magnetic field $\mathbf{B} = (0, 0, B(x))$ applied parallel to the surface, which induces screening currents $\mathbf{j} = (0, j(x), 0)$. We make the usual idealizations in the description of the NS sandwich: The superconducting order parameter follows a step function $\Delta(x) = \Delta\theta(-x)$ (Δ real), no attractive interactions being present in the normal layer. We assume a perfect NS interface as well as specular reflection at the normal-metal boundary.

In the subsequent analysis we restrict our attention to the magnetic response of the normal layer. In the proximity effect, the macroscopic coherence of the superconducting condensate induces correlated electron-hole pairs in the normal layer through the process of Andreev reflection. The basic process consists of an electron traveling forward and a hole traveling backward along a quasi-classical trajectory as shown in Fig. 4.2 (at discrete energies, bound Andreev states are found along these trajectories). In the presence of a magnetic field, the area enclosed by the trajectory (see Fig. 4.2) is threaded by the flux

$$\Phi(a, \vartheta, \varphi) = \oint \mathbf{A}(\mathbf{x}) \cdot d\mathbf{x} = 2 \tan \vartheta \cos \varphi \int_0^d A(x) dx, \quad (4.2)$$

which can be expressed through the integral $a = \int_0^d A(x) dx$ times a geometric factor due to the inclination of the trajectory (the spherical angles ϑ and φ parameterize the

direction of the trajectory with respect to the x -axis). The current carried along a trajectory depends on the phase factor $\Phi(a, \vartheta, \varphi) / \Phi_0$ acquired by the propagation of both the electron and the hole along the Andreev loop, and we arrive at an intrinsic non-local current–field dependence $j(a)$. The total current is determined by the sum over the currents along the quasi-classical trajectories, see (3.6), from which we obtain the current expression for finite fields [Zaikin 1982],

$$j(a) = \int_0^{\pi/2} d\vartheta \int_0^{\pi/2} d\varphi j(\vartheta, \varphi, \Phi(a, \vartheta, \varphi)), \quad (4.3)$$

where ($\alpha_n = 2\omega_n d / v_F \cos \vartheta$)

$$j(\vartheta, \varphi, \Phi(a, \vartheta, \varphi)) = -2ev_F N_0 T \sum_{\omega_n > 0} \sin^2 \vartheta \cos \varphi \times \frac{\Delta^2 \sin 2\pi\Phi / \Phi_0}{\left(\omega_n \cosh \alpha_n + \sqrt{\omega_n^2 + \Delta^2} \sinh \alpha_n\right)^2 + \Delta^2 \cos^2 \pi\Phi / \Phi_0}. \quad (4.4)$$

The induced currents for each trajectory depend only on the flux Φ modulo the superconducting flux quantum $\Phi_0 = \pi \hbar c / e$, reflecting gauge invariance. At small fields ($a / \Phi_0 \ll 1$), the current response is diamagnetic for all trajectories and the proximity effect produces screening currents in the normal metal. As the field increases to $a / \Phi_0 \sim 1$, some of the more extended trajectories produce paramagnetic currents, since the reduced flux $\Phi \in [-\Phi_0/2, \Phi_0/2]$ they enclose becomes negative, and the net diamagnetic current response is reduced. As we reach large fields ($a / \Phi_0 \gg 1$), the Andreev loops become mutually dephased due to a uniform distribution of the reduced flux. The associated currents are randomly dia- or paramagnetic and the net current vanishes. Note that the proximity effect, i.e., the existence of the Andreev levels is not destroyed in this limit, leading to a finite kinetic energy of the currents induced by the magnetic field.

4.3 Magnetostatics

Owing to the independence of j on x , the Maxwell equation $-\partial_x^2 A(x) = 4\pi j$ and the constitutive equation (4.3) combined with the boundary conditions $A(x=0) = 0$ and $\partial_x A(x=d) = H$ can be given a formal solution. We arrive at a parabolic dependence for

$$A(x) = Hx + 4\pi j(a) x \left(d - \frac{x}{2}\right), \quad (4.5)$$

parameterized by $a = \int_0^d A(x) dx$, which in turn is determined through the self-consistency condition

$$a = \frac{Hd^2}{2} + \frac{4\pi}{3} j(a) d^3. \quad (4.6)$$

The total magnetization \mathcal{M} (per unit surface) is defined by

$$4\pi\mathcal{M} = \int_0^d dx (\partial_x A(x) - H) = 2\pi j(a) d^2. \quad (4.7)$$

Eq. (4.6) contains the essential physics of the problem: For small fields ($a \rightarrow 0$), the current $j \sim -H/d$ linearly suppresses the magnetic induction to the $B(0) \rightarrow -H/2$ at the NS boundary (overscreening). The current is given by the linear response expression in this limit,

$$j(a/\Phi_o \ll 1) \approx -\frac{1}{4\pi\lambda_N^2(T)d}a, \quad (4.8)$$

which depends on penetration depth $\lambda_N(T) \ll d$, see (Eq. (4.15)). When inserted back into (4.6), the vector potential is found to be strongly suppressed to $a \sim H\lambda_N^2(T)$, and we obtain a consistent diamagnetic solution (i.e., $a/\Phi_o \ll 1$) for fields up to $H < \Phi_o/\lambda_N^2$. At large fields, the current vanishes ($j \rightarrow 0$) and the magnetic field penetrates the normal layer. From Eq. (4.6) we find $a \approx Hd^2/2$, consequently this metallic behavior is expected down to magnetic fields $H > \Phi_o/d^2$, as follows from the condition $a/\Phi_o \gg 1$ for the Andreev levels to be dephased. With $\Phi_o/d^2 \ll \Phi_o/\lambda_N^2$ the diamagnetic and field penetration solution coexist in the regime $\Phi_o/d^2 < H < \Phi_o/\lambda_N^2$. These simple estimates for the limits of the bistable regime elucidate the numerical data given in [Belzig 1996a].

4.4 Thermodynamics

In the phase diagram of Fig. 4.1 the upper and lower bounds of the bistable regime found from the above mean-field analysis are identified with the spinodals of the transition, the super-cooled field $H_{sc} \sim \Phi_o/d^2$ and the super-heated field $H_{sh} \sim \Phi_o/\lambda_N^2(T)$. In the thermodynamic equilibrium, a magnetic breakdown occurs at an intermediate field, connecting the diamagnetic regime to the field penetration regime by a first order transition. In the following, we determine this breakdown field and the associated entropy and magnetization jump from the free energy.

The energy (per unit surface) of the currents $j(x) = -\delta F/\delta A(x)$ is obtained via an integration over the non-linear current expression,

$$\begin{aligned} F(a) &= -\int_0^a j(a') da' \\ &= \hbar v_F N_0 T \sum_{\omega_n > 0} \int_0^{\pi/2} d\vartheta \int_0^{\pi/2} d\varphi \sin \vartheta \cos \vartheta \\ &\quad \log \frac{\left(\omega_n \cosh \alpha_n + \sqrt{\omega_n^2 + \Delta^2} \sinh \alpha_n\right)^2 + \Delta^2}{\left(\omega_n \cosh \alpha_n + \sqrt{\omega_n^2 + \Delta^2} \sinh \alpha_n\right)^2 + \Delta^2 \cos^2 \pi\Phi/\Phi_o}. \end{aligned} \quad (4.9)$$

$F(a)$ describes the difference in free energy between the metal layer under proximity and in the normal state. $F(a)$ is a monotonous and strictly positive function, reflecting the absence of condensation energy in the normal layer, and expresses the cost of the induced proximity effect lying in the kinetic energy of the currents induced by the vector potential. The free energy $\mathcal{F}(T, \mathcal{M})$ is constructed by adding the electro-magnetic field energy and subtracting the vacuum field contribution,

$$\mathcal{F}(T, \mathcal{M}) = F(a) + \int_0^d dx \left(\frac{(\partial_x A(x))^2}{8\pi} - \frac{H^2}{8\pi} \right). \quad (4.10)$$

We do not include the condensation energy and the kinetic energy of the screening currents in the superconductor. The field dependent term of the condensation energy might in fact be of the order of the free energy in the normal layer and would be expected to produce numerical corrections in the results, which are not accounted for by our idealized choice of the order parameter $\Delta(x) = \Delta\theta(-x)$. The kinetic energy of the screening currents $\sim H^2\lambda$ may be neglected.

After a Legendre transformation, we obtain the Gibb's free energy

$$\begin{aligned} \mathcal{G}(T, H) &= F(T, \mathcal{M}) - \mathcal{M}H \\ &= F(a) + \int_0^d dx \frac{(\partial_x A(x) - H)^2}{8\pi}. \end{aligned} \quad (4.11)$$

The field term in Eq. (4.11) describes the work necessary to expel the magnetic field. The extrema of the free energy \mathcal{G} with respect to a reproduce the equation of state (4.6). Fig. 4.2 shows the free energy $\mathcal{G}(H)$ as obtained from the parameterization of \mathcal{G} and H through a . The breakdown field $H_b(T)$ is determined by the intersection of the free energies \mathcal{G} of the two (meta)-stable solutions. We note that this procedure is equivalent to the Maxwell construction in the magnetization curve $\mathcal{M} = -\partial\mathcal{G}/\partial H$ of Fig. 4.2.

In the following, we consider the free energy (4.9) in the two temperature limits $T = 0$ and $T_A \ll T \leq \Delta$ and obtain ($T_A = \hbar v_F/2\pi d$),

$$\begin{aligned} F_{T=0}(a) &= \frac{1}{2}v_F N_0 T_A \int_0^{\pi/2} d\vartheta \int_0^{\pi/2} d\varphi \sin\vartheta \cos^2\vartheta \{\arctan[\tan\pi\Phi/\Phi_0]\}^2, \\ F_{T \gg T_A}(a) &= 4v_F N_0 T \gamma^2(T, \Delta) \int_0^{\pi/2} d\vartheta \int_0^{\pi/2} d\varphi \sin\vartheta \cos\vartheta \\ &\quad \exp\left(-\frac{2T}{T_A \cos\vartheta}\right) \sin^2\pi\Phi/\Phi_0. \end{aligned} \quad (4.13)$$

The finite value of the superconducting gap Δ is accounted for by the dimensionless parameter $\gamma(T, \Delta) = \Delta / \left(\sqrt{\Delta^2 + (\pi T)^2} + \pi T \right) < 1$.

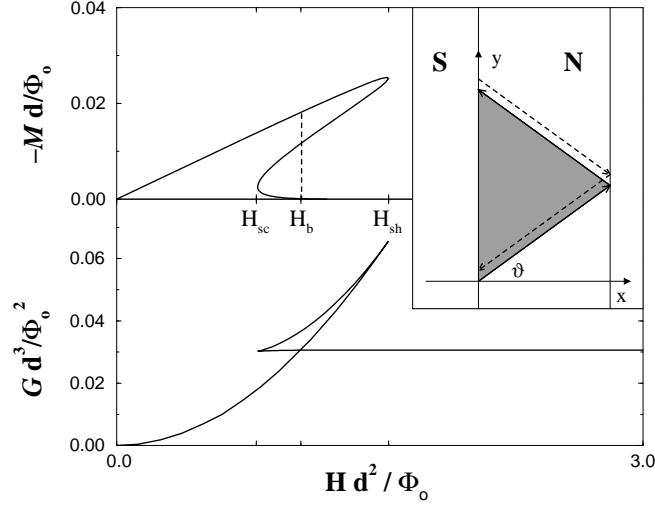


Figure 4.2: Magnetization $\mathcal{M}(H)$ and free energy $\mathcal{G}(T, H)$ at a temperature $T = 1.5 T_A$ ($T_A = v_F/2\pi d$). The representation is universal in the thickness d . The small and large field branches represent (meta)-stable solutions describing the diamagnetic and field penetration phases, which overlap in the field interval $H_{sc} < H < H_{sh}$. The Maxwell construction determines the first order transition between the phases at the breakdown field H_b (dashed line). Inset: Cross-section of the normal-metal slab in contact with the bulk superconductor. The flux enclosed by the quasi-classical electron-hole trajectory (Andreev loop) enters as a phase factor in the Green's function.

The free energies of the two (meta)-stable states can be approximated by their asymptotic forms in the limits $a \rightarrow 0$ and $a \rightarrow \infty$. In the diamagnetic regime, the expansion in a/Φ_0 up to quadratic order of (4.12) and (4.13) provide the result

$$F(a) \approx \frac{a^2}{8\pi\lambda_N^2(T)d}. \quad (4.14)$$

Eq. (4.14) is valid both in the low and high temperature limits using the penetration depth $1/\lambda_N^2(0) \equiv 1/\lambda_N^2 = (4\pi ne^2/m)$ at $T = 0$ and

$$\frac{1}{\lambda_N^2(T)} = \frac{1}{\lambda_N^2} \gamma^2(T, \Delta) \frac{6T_A}{T} e^{-2T/T_A} \quad (4.15)$$

for $T \gg T_A$. Note that the derivative $j = -\partial F/\partial a$ applied to Eq. (4.14) produces the linear response constitutive relation of Eq. (4.8). The Gibb's free energy follows from Eqs. (4.10) and (4.14), using the solution of the Maxwell equations,

$$\mathcal{G}(a \ll \Phi_0) \approx \frac{3}{32\pi} H^2 d. \quad (4.16)$$

Eq. (4.16) is dominated by the magnetization work necessary to expel the field, which is parametrically larger (by $(d/\lambda_N(T))^2$) than the kinetic energy of the currents. We note that the scaling in the free energy (4.16), $\mathcal{G} \sim H^2 d$, is parametrically independent of the nonlocality range of the constitutive relation (4.4).

In the field penetration regime we approximate the free energy by its asymptotic value at $a \rightarrow \infty$. In this limit we replace the strongly oscillating functions of Φ in (4.12) and (4.13) by their average value $\langle (\arctan \tan \Phi)^2 \rangle = \pi^2/12$ and $\langle \sin^2 \Phi \rangle = 1/2$ and obtain

$$\begin{aligned} \mathcal{G}_{T=0} (a \gg \Phi_o) &\approx \frac{1}{384\pi} \frac{\Phi_o^2}{\lambda_N^2 d}, \\ \mathcal{G}_{T \gg T_A} (a \gg \Phi_o) &\approx \frac{3}{16\pi^3} \gamma^2(T, \Delta) \frac{\Phi_o^2}{\lambda_N^2 d} e^{-2T/T_A}. \end{aligned} \quad (4.17)$$

The magnetization energy vanishes in this limit. The corrections to the free energy (4.17) are of relative order $(\Phi_o/a)^2$.

The magnetic breakdown field $H_b(T)$ is determined by the intersection of the two asymptotics of the free energy \mathcal{G} given by Eqs. (4.16) and (4.17),

$$\begin{aligned} H_b(T=0) &\approx \frac{1}{6} \frac{\Phi_o}{\lambda_N d}, \\ H_b(T \gg T_A) &\approx \frac{\sqrt{2}}{\pi} \gamma(T, \Delta) \frac{\Phi_o}{\lambda_N d} e^{-d/\xi_N(T)}. \end{aligned} \quad (4.18)$$

$$H_b(T \gg T_A) \approx \frac{\sqrt{2}}{\pi} \gamma(T, \Delta) \frac{\Phi_o}{\lambda_N d} e^{-d/\xi_N(T)}. \quad (4.19)$$

We note three important features of this result: The temperature dependence is a simple exponential with the exponent $d/\xi(T) = T/T_A$, where $\xi_N(T) = v_F/2\pi T$ denotes the thermal length. The amplitude of the breakdown field scales inversely proportional to the thickness of the normal layer, $H_b \sim 1/d$. In the limit $T \rightarrow 0$ the magnetic breakdown field saturates to a value which is suppressed by the factor $\pi/6\sqrt{2} \approx 0.37$ as compared to the extrapolation of the high temperature result. The formula for the breakdown field $H_b \sim \Phi_o/\lambda_N(T)d$ is similar to the critical field $H_c \sim \Phi_o/\lambda\xi_0$ of a Type I superconductor [Blatter 1994], the geometric scale d replacing the superconducting coherence length ξ_0 .

We arrive at the $H-T$ phase diagram shown in Fig. 4.1. The first order transition between the diamagnetic and the field penetration regime takes place between the spinodals $H_{sc} \sim \Phi_o/d^2 < H_b(T) < H_{sh} \sim \Phi_o/\lambda_N(T)^2$ which delimit the (meta)-stable regime. Their intersection marks the critical temperature

$$T_{crit} \approx T_A \log(d/\lambda_N), \quad (4.20)$$

where $\lambda_N(T_{crit}) \approx d$. Below T_{crit} the penetration depth is small, $\lambda_N(T_{crit}) < d$, and we observe a first order transition. Above the critical point T_{crit} , where $\lambda_N(T_{crit}) >$

d , a continuous and reversible cross-over between the diamagnetic and field penetration regime is expected.

The latent heat (at $T \gg T_A$) of the transition follows from Eqs. (4.16), (4.17), and (4.19) using $S = -\partial\mathcal{G}/\partial T$,

$$T\Delta S \approx \frac{3}{16\pi} \frac{T}{T_A} H_b^2(T) d, \quad (4.21)$$

and is related to the magnetization jump

$$4\pi\Delta\mathcal{M} \approx \frac{3}{4} H_b(T) d \quad (4.22)$$

via the Clausius-Clapeyron equation.

In the derivation of the breakdown field we have used the asymptotic expansions of the free energies in a/Φ_o and Φ_o/a , respectively. Their quality at the transition point is determined by the range of overlap between the diamagnetic and the field penetration regimes in Fig. 4.2, which is governed by the parameter $\lambda_N(T)/d$. In the diamagnetic phase, the corrections are of the order of $(a/\Phi_o)^2 \sim (H_b\lambda_N^2(T)/\Phi_o)^2 \sim (\lambda_N^2(T)/d)^2$, and similarly in the field penetration regime. The expansion thus breaks down at $\lambda_N(T) \approx d$, which is the critical point of the transition line. We note that the total magnetization changes from its diamagnetic value $\mathcal{M} \sim H_b d$ to the strongly suppressed value $\mathcal{M} \sim H_b d (\lambda_N(T)/d)^2$ at the transition, reflecting its strong first order character.

4.5 Experiment

The breakdown field has been measured in fairly clean Ag-Nb cylinders recently [Mota 1989, Mota 1994]. Let us compare our results from the clean limit theory with the experimental data. We neglect the difference in geometry, cylindrical for the sample and planar in the theoretical model.

In Fig. 4.3 we show the two data sets for the breakdown field data obtained on heating and cooling a sample of thickness $d = 5.5\mu\text{m}$ exhibiting hysteresis. We note that the theoretical values of the super-cooled and super-heated fields H_{sc} and H_{sh} are not reached in the experiments, as the phase transition is smoothed by the breakdown of local (Andreev) current loops, see Fig. 4.2. The data saturates at low temperatures, in qualitative agreement with our theoretical analysis. Given the electron density in Ag, $n = 5.8 \cdot 10^{22} \text{cm}^{-3}$ ($\Rightarrow \lambda_N = 2.2 \cdot 10^{-2} \mu\text{m}$) and $d = 5.5\mu\text{m}$, the breakdown field is determined by Eq. (4.18) and (4.19). Due to the idealization of our model, which assumes a step function for the order parameter, as well as the difference between the planar and cylindrical geometry, we expect a numerical factor correcting the amplitude of H_b . Making use of the scaling factor ≈ 0.56 in Eqs.

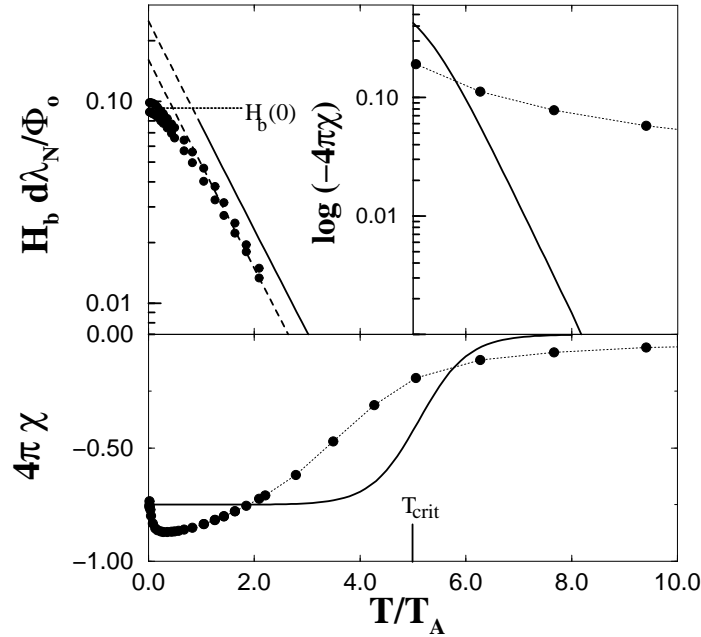


Figure 4.3: Breakdown field $H_b(T)$ and linear susceptibility $4\pi\chi$ from theory and experiment (the analysis applies to a Ag-Nb sample of thickness $d = 5.5\mu\text{m}$). Theory: results of Eqs. (4.19) and (4.24) shown as solid lines; $H_b(T)$ is rescaled to fit the zero temperature value $H_b(0)$ (horizontal line) to the experiment. Experiment: data shown as solid dots, the dotted line is a guide to the eye[Mota 1994]. Note that the logarithmic slope of the breakdown field is reproduced precisely (dashed line), while the one of the susceptibility is much smaller than expected.

(4.18) and (4.19), we calibrate the theoretical result to fit the zero temperature value $H_b(0)$, as shown in Fig. 4.3. The theoretical prediction for the high temperature behavior then follows from Eq. (4.19) and is shown as a solid line in Fig. 4.3. Eq. (4.19) accurately reproduces the logarithmic slope $-1/T_A$ of the experimental data, thus correctly tracing the signature of the Andreev levels. The amplitude of $H_b(T)$ deviates from the data by the constant ratio ≈ 0.64 , which can be attributed to the presence of a barrier at the NS interface, see below.

A further agreement between theory and experiment is found in the scaling of the breakdown field with sample thickness d , which was reported to be $\propto 1/d$, in accordance with Eq. (4.19) (the experimental study involved 10 samples [Mota 1994] with thicknesses ranging from $d = 2.9\mu\text{m}$ to $d = 28\mu\text{m}$ ¹). Similarly, the critical temperature determined in the experiment[Mota 1989] exhibits the same scaling $\propto 1/d$, in agreement with Eq. (4.20) ($T_A \propto 1/d$).

¹We acknowledge unpublished data provided by B. Müller-Allinger and A. Mota, ETH Zürich.

For comparison, we cite the dirty limit result, which follows from the GL equations [de Gennes 1966b],

$$H_D(T) \approx 1.9 \frac{\Phi_0}{\lambda_D \xi_D} \exp(-d/\xi_D), \quad (4.23)$$

where $\xi_D = \sqrt{v_F l / 6\pi T}$ and λ_D is a fitting parameter for the penetration depth at the NS interface. Both the exponential dependence on $d/\xi_D \propto \sqrt{T}$ and the independence of the overall amplitude on d clearly deviate from the experimental data.

The good agreement between the clean limit theory and experiment for the breakdown field does not trivially generalize to other physical quantities, however. In particular, the linear susceptibility $\chi = \mathcal{M}/H$ sensitively depends on the non-locality of the constitutive relation $j(a)$. From Eqs. (4.7) and (4.8) we obtain the susceptibility

$$4\pi\chi = \frac{4\pi\mathcal{M}}{H} = -\frac{3}{4} \frac{1}{1 + 3\lambda_N^2(T)/d^2}, \quad (4.24)$$

which exhibits a temperature dependence with the following characteristics: $4\pi\chi$ decays exponentially $\propto 1/\lambda_N^2(T)$ at large temperatures, twice as fast as the breakdown field. The susceptibility takes half its maximal value at $3\lambda_N^2(T_{1/2})/d^2 \sim 1$, which roughly coincides with the critical temperature T_{crit} . The logarithmic derivative at $T = T_{1/2}$ is predicted to be $\chi'(T_{1/2})/\chi(T_{1/2}) = 1/T_A$. Below the critical point, the susceptibility saturates as the penetration depth decreases below the sample thickness ($\lambda_N(T) < d$). Due to the non-locality, the penetration depth drops out of the expression for $4\pi\chi \approx -3/4$ and we are in the regime of over-screening. In Fig. 4.3 we show the linear susceptibility according to the clean limit predictions (4.24) (there is no fitting parameter). The experimental data fails to show the typical saturation of the susceptibility expected below the critical temperature. At low temperature the experimental value clearly exceeds the maximal diamagnetic value $-3/4$ found in the clean limit. The decay at large temperature is slower than the decay of the breakdown field, while Eq. (4.24) predicts a decay with twice the logarithmic slope, see Fig. 4.3. This discrepancy finds a natural explanation in the different sensitivity of $H_b(T)$ and $\chi(T)$ to the degree of nonlocality in the constitutive relation, as we discuss in the following section.

Let us consider the influence of an insulating barrier at the NS interface. The consequences of a finite reflectivity at the NS interface on the linear current response has been analyzed in [Higashitani 1995]. Their results allow for the reflection coefficient R to be included in the penetration depth $\lambda_N(T)$ by redefining the factor $\gamma_R(T_A \ll T \ll \Delta) = (1 - R)/(1 + R)$, in Eq. (4.15); $\lambda_N(0) \equiv \lambda_N$ remains unchanged. Inserting the modified penetration depth into Eq. (4.24) we obtain the linear susceptibility. The additional factor γ does not change the characteristic shape

of the susceptibility (saturation, logarithmic slope at $T_{1/2}$, exponential decay), but only lowers the position of the half-value of χ to $T_{1/2} \approx \log[d(1-R)/\lambda_N(1+R)]$. The finite reflection does not remedy the qualitative discrepancy between the susceptibility in theory and experiment, in consistency with the above considerations. Considering the structure of the equations we may expect the dependence on the reflection R to enter in a similar fashion into the breakdown field $H_b(T)$. Eq. (4.24) inserted in Eq. (4.19) gives the high temperature behavior, while the zero temperature result of Eq. (4.18) remains unchanged. We fit the breakdown field data by using first an overall scaling factor needed to adjust $H_b(0)$ and second, a finite reflectivity, which only enters at high temperatures. The fit of the high temperature behavior provides us with an estimate of the reflectivity $R \approx 0.21$ of the NS interface, see Fig. 4.3 (dashed line).

4.6 Discussion

We have calculated the clean limit expression for the breakdown field separating the diamagnetic phase and the field penetration phase by a first order transition. We have determined the spinodals, the critical temperature as well as the latent heat of the transition.

In Chapter 3 we found that the solution of the screening problem crucially depends on the nonlocality range. The high sensitivity to impurities is a consequence of the self-consistency problem with the Maxwell equations. In the ballistic regime $l > d$ the linear screening was found to be enhanced as compared to the clean limit, at low temperature due to the kernel range l and at high temperature due to the range $\xi_N(T)$. Here the clean limit result for the breakdown field has been found to be in good agreement with the experimental data on fairly clean samples ($l \gtrsim d$). We resolve this apparent discrepancy by showing the the self-consistent screening problem drops out of the derivation of the breakdown field: The breakdown field $H_b \sim \Phi_0/\lambda_N(T)d$ is obtained from matching the magnetization energy $\mathcal{G} \sim H_b^2 d$ in the diamagnetic phase with the kinetic energy in the penetrating field $\mathcal{G} \sim \Phi_0^2/\lambda_N^2(T)$. The magnetization energy overshadows the kinetic energy of the currents in the diamagnetic phase, which contain the solution of the screening problem. Thus the breakdown field is remarkably stable towards a finite impurity concentration. A correction to the breakdown field of order d/l is expected from the kinetic term in the field penetration phase at temperatures $T \sim T_A$. We note that the high temperature corrections, which are relevant beyond $T_{1/2}$ hardly affect the breakdown field, as T_c and $T_{1/2}$ coincide. The inclusion of a finite reflection at the NS interface permits an accurate fit of the breakdown field and gives an estimate for the quality of the NS interface.

Chapter 5

Paramagnetic instability of Andreev electrons

5.1 Introduction

A normal metal in contact with a superconductor exhibits the phenomenon of proximity — the superconductor exports its coherent state across the interface into the normal metal. On a microscopic level, this phenomenon is described through the Andreev reflection of the normal-metal quasi-particles at the NS interface, converting normal- to supercurrent. Proximity superconductivity exhibits a rich phenomenology and has attracted considerable interest recently [Kouwenhoven 1997]. A particularly puzzling finding is the ultra-low-temperature reentrance observed in normal-metal coated superconducting cylinders [Visani 1990a], where, contrary to expectation, the fully diamagnetic cylinder develops a paramagnetic response at low temperatures. Recently, it has been speculated that some novel kind of persistent current states circling the cylinder might be responsible for this phenomenon [Bruder 1998], but closer inspection of the experimentally measurable quantities reveals that the predicted effect is by orders of magnitude too small [Fauchère 1999a]. In this chapter, we demonstrate that the presence of a repulsive electron-electron interaction in the normal metal naturally leads to the appearance of a paramagnetic instability at very low temperature, offering a possible explanation of the reentrance effect in the NS cylinders.

For simplicity, we consider a clean normal-metal slab of thickness d ($0 < x < d$), in perfect contact with a bulk, conventional superconductor. The proximity effect is mediated by the Andreev reflection at the interface with the superconductor, which binds the quasi-particles states to the normal layer for $E < \Delta_S$. In the usual free electron gas description of the normal metal, the Andreev bound states are found at $E_n = \hbar v_x(2n + 1)\pi/4d$ ($n = 0, 1, \dots$; $v_x = v_F \cos \vartheta$) producing a linear suppression

of the DOS [de Gennes 1963, Saint-James 1964]

$$N(E) \sim N_0 E d / \hbar v_F, \quad (5.1)$$

close to the Fermi level $E = 0$ ($N_0 = m k_F / \hbar^2 \pi^2$). In the following we assume that the electron-electron interaction in the normal layer, which follows from the delicate balance between the phonon-mediated- and the Coulomb-interaction, is repulsive. As a consequence, a finite order parameter $\Delta(x)$ is induced in the metal, opposite in sign as compared to Δ_S in the superconductor, see Ref. [de Gennes 1964]. The NS junctions then behaves like a Josephson junction with a phase difference π , trapping quasi-particle states at the Fermi energy close to the NS interface. The local density of states $N(E, x)$ exhibits a peak at zero energy on top of the Andreev density of states, as shown in Fig. 5.1. This peak involves a macroscopic number of states with density $n_p \sim k_F^2 / d$, which in the following we call the π -states.

The change in the DOS crucially affects the response of the proximity metal. The linear current response $j[A]$ can be divided into two contributions $j = j_{\text{dia}} + j_{\text{para}}$, the diamagnetic current $j_{\text{dia}} = -(e^2 n / mc) A$ giving the rigid response of the bulk density $n = k_F^3 / 3\pi^2$ and the paramagnetic current j_{para} following from the deformation of the wavefunction at the Fermi surface [Schrieffer 1988],

$$j_{\text{para}} = \frac{e^2 n}{mc} A \int dE \left(-\frac{\partial f}{\partial E} \right) \frac{N(E)}{N_0} \quad (5.2)$$

for slowly varying fields A (f is the Fermi occupation number). While in a bulk superconductor the paramagnetic current is quenched by the energy gap at low temperatures producing a net diamagnetic response, the paramagnetic current of a bulk normal metal cancels the diamagnetic current exactly. In the non-interacting metal under proximity, the linear density of states suppression $N(E) \propto E$ is still sufficient to suppress the paramagnetic current at zero temperature [Zaikin 1982]. Including a repulsive interaction places the system in the opposite limit: The sharp DOS peak at the Fermi level produces a paramagnetic signal which *over*-compensates the diamagnetic response. Such a paramagnetic response naturally leads to an instability: The free energy $\delta F = -c j \delta A < 0$ can be lowered via a non-zero magnetic induction induced by spontaneous currents along the NS interface. The interface currents are associated with an orbital magnetization $M(T)$ producing a low-temperature reentrance in the magnetic susceptibility.

5.2 Zero energy bound states

In the following we present a quantitative analysis of the paramagnetic instability induced by the π -states. The magnetic induction $B_z(x)$ parallel to the surface is described by the vector potential $A_y(x)$ which drives the currents $j_y(x)$. The

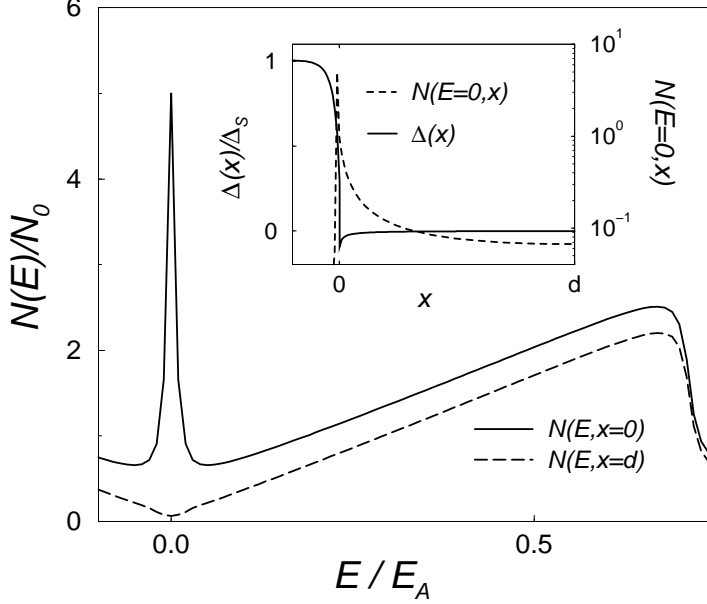


Figure 5.1: Local DOS $N(E, x)$ at the NS interface $x = 0$ and at the metal boundary $x = d$ ($E_A = \hbar v_F/d$), as it follows from the self-consistent solution of the Eilenberger equation, Eqs. (5.3) and (5.4), for a thickness $d = 10\hbar v_F/\Delta_S$ and the coupling constants $V_S = -0.3$ and $V_N = 0.1$. Inset: Spatial dependence of the order parameter $\Delta(x)$ and local DOS $N(E = 0, x)$ at the peak energy (S: $x < 0$, N: $x > 0$).

electron-electron interaction in the superconductor is accounted for by an effective coupling constant $V_S < 0$ and similarly $V_N > 0$ in the normal metal, see also [Zhou 1995, Nazarov 1996]. Two self-consistency problems have to be solved: First, we evaluate the order parameter $\Delta(x)$ accounting for the different coupling constants in the superconductor and the normal metal, and obtain the local DOS $N(E, x)$. Second, we determine the current functional $j[A]$ which we solve together with Maxwell's equation to find the spontaneous interface currents.

We use the quasi-classical description following from the Eilenberger equation, see (3.2),

$$-v_x \partial_x \hat{g} = [\{\omega_n + iev_y A_y(x)\} \hat{\tau}_3 + \Delta(x) \hat{\tau}_1, \hat{g}], \quad (5.3)$$

where the 2×2 matrix \hat{g} have been defined in Chp. 3.1. Eq. (5.3) is completed by the self-consistency relation for the pair potential ($\langle \dots \rangle$ is the angular average),

$$\Delta(x) = -VN_0\pi T \sum_{\omega_n > 0} \langle f_{\omega_n}(x, v_x) \rangle. \quad (5.4)$$

The self-consistent numerical solution of Eqs. (5.3) and (5.4) is shown in the inset of Fig. 5.1. The course of the order parameter in the normal layer is asymptotically given by $\Delta(x) \sim -V_N N_0 \hbar v_F / x$, as expected from the f -function in the non-interacting case $V_N = 0$ [Falk 1963]. $\Delta(x)$ decays from a value $\sim -|V_N/V_S| \Delta_S$ at the NS interface, to $\sim -V_N N_0 \hbar v_F / d$ at the outer boundary. Close to the NS interface, the local DOS

$$N(E, x) = N_0 \text{Re}[\langle g_{-iE+\delta}(x, v_x) \rangle], \quad (5.5)$$

exhibits a pronounced peak at zero energy, as shown in Fig. 5.1. At the outer metal boundary $x = d$ the DOS is suppressed linearly, as in the noninteracting case [de Gennes 1963]. Such a pseudogap is typical in proximity induced superconductivity [Hara 1993, Frahm 1996]. We note that a peak structure as a consequence of interactions could be related to one found for a Luttinger liquid in proximity with a superconductor [Fazio 1996].

In order to proceed with analytical results, we approximate the order parameter by a step function,

$$\Delta(x) = \begin{cases} \Delta_S, & x < 0, \\ -\Delta_N, & 0 < x < d, \end{cases}$$

where $\Delta_N \propto V_N$ enters as a parameter. The Green's function in the normal layer $x > 0$ can be determined exactly and takes the form

$$g_{\omega_n}(x, v_x) = \frac{\omega_n \sinh[\chi(d) - \gamma] + \Delta_N \cosh[\chi(d - x)]}{\Omega_n \cosh[\chi(d) - \gamma]}, \quad (5.6)$$

where $\chi(x) = 2\Omega_n x / v_x$, $\Omega_n^2 = \Delta_N^2 + \omega_n^2$, and $\tanh \gamma = \Delta_N / \Omega_n$ (we consider the limit $\Delta_S \gg \Delta_N, T$). The second term in (5.6) describes the π -states at the NS interface. The poles of the Green's function at $\omega_n \rightarrow -iE + 0$ yield the bound state energies. For $E > \Delta_N$ the bound states given by

$$\sqrt{E^2 - \Delta_N^2} = \frac{\hbar v_x}{2d} \left(n\pi + \arccos \frac{E}{\Delta_N} \right), \quad (n = 0, 1, \dots), \quad (5.7)$$

down-shifted by $\delta E_n \approx -2\Delta_N / (2n + 1)\pi$ with respect to the Andreev states of the free electron gas. Below the gap $E < \Delta_N$ we find the π -states at

$$E = \Delta_N / \cosh \frac{2\sqrt{\Delta_N^2 - E^2}d}{v_x} \sim \Delta_N e^{-2\Delta_N d / v_x}, \quad (5.8)$$

exponentially close to Fermi energy. All trajectories with $v_x = v_F \cos \vartheta \ll \Delta_N d /$ possess a bound state at $E \approx 0$, thus producing the macroscopic weight of the zero energy DOS peak: For $\Delta_N > v_F / d$ the number of π -states per unit surface N_{surf} is equal to the number of transverse levels $N_{\text{surf}} \sim k_F^2$, while for $\Delta_N < v_F / d$ it is reduced to $N_{\text{surf}} \sim k_F^2 (\Delta_N d / v_F)^2$ via the reduction of the available solid angle $\cos \vartheta < \Delta_N d / v_F$.

5.3 Spontaneous currents and magnetization

We derive the current-field relations at low temperatures, assuming $T \ll v_F/d, \Delta_N$. This implies a thermal length $\xi_N(T) = \hbar v_F/2\pi T$ larger than the thickness d and no thermal smearing on the scale Δ_N . Only the trajectories with $\cos\vartheta < \Delta_N d/v_F$ contribute to the current at low temperatures. We describe them in the limit $v_x/\Delta_N d \rightarrow 0$ by

$$g_{\omega_n}(x, v_x) = \frac{\omega_n}{\Omega_n} + \frac{\omega_n \Delta_N}{\Omega_n (\Omega_n - \Delta_N)} e^{-\chi(x)}. \quad (5.9)$$

The current in the presence of a slowly varying vector potential A , follows from Eq. (5.9) after replacing ω_n by $\omega_n + iev_y A$ and inserting it into the quasi-classical current expression, see (3.6). In addition to the diamagnetic current

$$j_{\text{dia}} = -(c/4\pi\lambda_N^2) A, \quad (5.10)$$

[$\lambda_N = (mc^2/4\pi ne^2)^{-1/2}$ denotes the London length], we obtain the paramagnetic current

$$j_{\text{para}} \approx \frac{c}{4\pi\lambda_N^2} e^{-x/\alpha\xi_N^0} \alpha \frac{3\Phi_0}{2\pi\xi_N^0} \arctan \frac{ev_F A}{\pi T}, \quad (5.11)$$

in the limit $ev_F A/c, T \ll \Delta_N$. Here, $\Phi_0 = \pi\hbar c/e$ denotes the flux quantum, and the coherence length in the normal metal

$$\xi_N^0 = \hbar v_F/2\Delta_N, \quad (5.12)$$

gives the extent of the π -states. Under the assumption $\Delta_N > v_F/d$ we set $\alpha = 1$. At temperatures $T \gg ev_F A/c$ the paramagnetic current $j_{\text{para}} \sim (1/\lambda_N^2)(\Delta_N/T)A$ is linear in A and $\propto 1/T$, a signature of the thermally smeared zero energy DOS peak, and competes with the diamagnetic current on the scale ξ_N^0 . At $T \rightarrow 0$, Eq. (5.11) is nonlinear in the field and generates the spontaneous paramagnetic current. This paramagnetic interface current results from the energy splitting of the π -states in the field, $E \approx \pm ev_F A$, allowing the system to gain energy by shifting the DOS below the Fermi surface¹. For $\Delta_N < \hbar v_F/d$, the paramagnetic current is reduced by the factor $\alpha = (\Delta_N d/\hbar v_F) < 1$ in Eq. (5.11). The surface current $I = \int j dx \sim \alpha^2 c\Phi_0/\lambda_N^2$ is in agreement with the current estimate $I_\pi \sim N_{\text{surf}} ev_F$ based on the number of π -states at zero energy. Eq. (5.11) thus always produces a net paramagnetic response at low temperature and fields.

The evaluation of the induced magnetization requires the self-consistent solution of Maxwell's equation $-\partial_x^2 A(x) = 4\pi j(x)/c$ together with the current functional

¹A similar mechanism producing spontaneous currents is discussed by Honerkamp *et al.* [Honerkamp 1998]

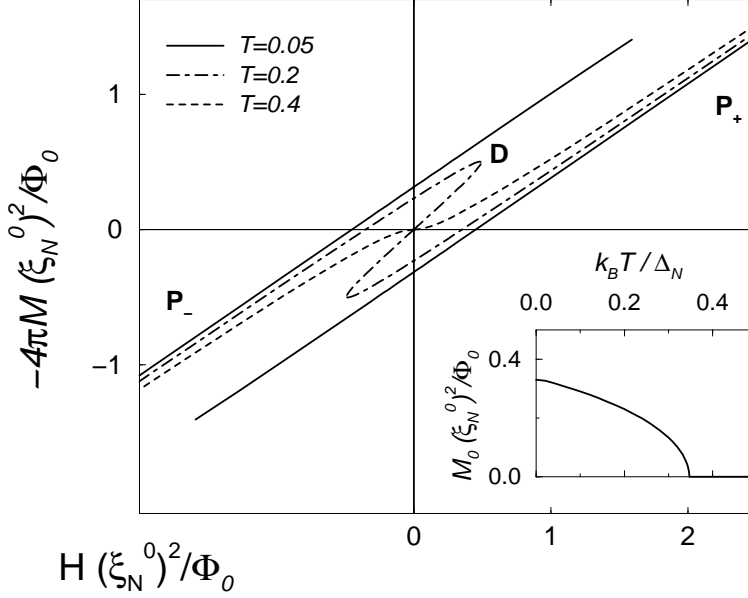


Figure 5.2: Magnetization $M(T, H)$ curve at various temperatures (in units of Δ_N), for $\lambda_N = 0.3d$ and $\xi_N^0 = d$. The two meta-stable branches P_{\pm} exhibit a spontaneous magnetization in zero field, the diamagnetic branch D is unstable. Inset: Zero field magnetization $M_0(T)$.

$j[A(x)]$. The solution of the screening problem requires the full dispersive relation between $j(q)$ and $A(q)$. According to the study of Chp. 3, the coherence length in the normal metal ξ_0 gives the nonlocality range, as Δ_N is the off-diagonal self-energy in (3.2). Eq. (5.11) represents the long wavelength limit $q \rightarrow 0$. For simplicity, here we use Eq. (5.11) under the assumption of local response. Including the nonlocality in the constitutive relations does not alter the spontaneous interface currents qualitatively.

The magnetization curves $M(T, H)$, which follow from Eq. (5.11) are shown in Fig. 5.2. Approaching from large fields, Fig. 5.2 shows two paramagnetic branches P_{\pm} with a linear diamagnetic slope exhibiting a spontaneous magnetization in zero field. They result from the superposition of the paramagnetic magnetization $M_0(T)$ and the Meissner response to the applied field H . As the field is decreased (increased) past $H = 0$, the branch P_+ (P_-) becomes meta-stable. The spontaneous magnetization $M_0(T)$ appears below a second order transition point T_c^M and saturates at low temperatures, as shown in the inset of Fig. 5.2. The magnetization

curve includes a diamagnetic branch D , which arises from the competition between the paramagnetic instability and the thermal smearing and is thermodynamically unstable.

In the following we give a semi-quantitative analysis of the magnetization $M = \int dx M(x)/d$, first at zero temperature and field [M_0], proceeding to finite temperatures [$M_0(T)$], and finally including an applied magnetic field H [$M(T, H)$]. The boundary conditions are given by $A(0) = 0$ and $\partial_x A(d) = H$. We concentrate on the most relevant limit where $\xi_N^0, d \gg \lambda_N$. At $T = 0$, according to Eq. (5.11), the paramagnetic interface current $j \sim \alpha\Phi_0/\lambda_N^2\xi_N^0$ remains unscreened until being matched by $j_{\text{dia}} \sim -A/\lambda_N^2$, producing a vector potential $A \sim \alpha\Phi_0/\xi_N^0$ on the scale λ_N . The vector potential A saturates beyond λ_N , as the para- and diamagnetic currents cancel each other. Assuming that the π -states extend up to the outer metal surface ($\alpha < 1$), the induced magnetization $M = A(d)/4\pi d$ is given by

$$M_0 \sim \alpha \frac{\Phi_0}{\xi_N^0 d} \sim \frac{\Phi_0}{(\xi_N^0)^2}. \quad (5.13)$$

We note that although the spontaneous currents increase as $\Delta_N > \hbar v_F/d$ ($\alpha = 1$) they are screened exponentially beyond the extent of the π -states in this limit, giving a magnetization $M_0 \sim (\Phi_0/\xi_N^0 d) \exp[-(d - \xi_N^0)/\lambda_N]$. We assume $\alpha < 1$ in the following.

At finite temperature, the spontaneous magnetization is suppressed by the factor $\arctan(\epsilon v_F A/\pi T)$, which itself depends on the magnetization via $A \sim Md$, implying the implicit equation

$$\frac{M_0(T)}{M_0} \sim \arctan \frac{M_0(T)\alpha\Delta_N}{M_0 T}. \quad (5.14)$$

The spontaneous magnetization appears below a second order transition at $T_c^M \sim \alpha\Delta_N$, saturating at low temperatures, as shown in the inset of Fig. 5.2. The transition temperature is equal in magnitude to the energy splitting of the DOS peak $E \sim \epsilon v_F A/c \sim \alpha\Delta_N$.

Under an applied magnetic field H , the Meissner current j_{dia} screens both the spontaneous interface current and the applied field. At zero temperature we deal with a linear problem and the magnetization is given by the superposition $M(H) = M_0 + \chi H$ of the spontaneous magnetic moment M_0 and the Meissner response χH . As the temperature increases, $M_0(T)$ decreases and the meta-stable regime shrinks. At $T > T_c^M$ the spontaneous magnetization in zero field has disappeared, the signature of the paramagnetic currents remains, however, reducing the diamagnetic susceptibility χ at small fields. At large temperature $T \gg T_c^M$ we recover the pure Meissner response.

Note that the two meta-stable branches P_+ and P_- in the magnetization curve, see Fig. 5.2, imply a first order transition with changing field at $H = 0$. The

first order transition is similar to the magnetic breakdown occurring in the same system at large fields between the fully diamagnetic phase and a field penetration phase [Fauchère 1997]. The rotation of the magnetic moments to the energetically more favorable polarization will show the hysteretic behavior typical for a first order transition. The transition from P_+ to P_- implies a paramagnetic slope in the thermodynamic dc -magnetization $\langle M(T, H) \rangle$, which will link the meta-stable solutions P_{\pm} in Fig. 5.2 and cross the origin at $M(H = 0) = 0$. In summary, we find that on approaching T_c^M from above, the diamagnetic susceptibility $\chi_{dc} = \langle M(T, H) \rangle / H$ is reduced, exhibiting a low-temperature reentrance. Below T_c^M , the spontaneous interface currents produce a net paramagnetic susceptibility χ_{dc} .

5.4 Discussion

In the following we discuss our results in the context of the experiments by Mota and co-workers, who have measured the magnetic response of normal-metal coated superconducting cylinders at low temperatures [Visani 1990a, Mota 1989]. In the previous chapters 3 and 4 we have established a quantitative understanding of the magnetic response of these samples at higher temperatures, studying the screening at small impurity concentration and the magnetic breakdown at finite field. The samples are typically characterized by a mean free path $l \sim d$ and an interface transparency of order unity. The Nb-Ag and Nb-Cu cylinders show an anomalous paramagnetic signal in the magnetic response in the low-temperature – low-field corner of the $H - T$ phase diagram [Visani 1990a, Mota 1994]. A direct comparison with our theory requires the magnetization curve $\langle M(T, H) \rangle$ which has not yet been measured. The observed dc -susceptibility $\chi_{dc}(T)$ as a function of temperature shows an increase at low temperature [Mota 1997]. The measured ac -susceptibilities $\chi_{ac}(T)$ and $\chi_{ac}(H)$ exhibit a reentrance both as a function of temperature and field [Visani 1990a]. The reentrance is accompanied by an out-of-phase response signaling dissipation and by hysteresis in the field dependence. These features are in qualitative agreement with our results for the magnetization curve. We find that theory and experiment agree in order of magnitude for $\alpha^2 \sim 0.1$, implying a transition temperature $T_c^M \sim 100\text{mK}$ and a spontaneous magnetization $M_0 \sim 1\text{G}$. A more quantitative comparison with experiment requires a self-consistent treatment of the spontaneous currents with the pair potential, accounting for the nonlocality of the current-field relation and its sensitivity to disorder.

In conclusion, we have demonstrated that the inclusion of a finite electron-electron repulsion in a proximity coupled normal-metal layer naturally produces spontaneous interface currents leading to a paramagnetic reentrance in the magnetic response: The sign change in the coupling across the NS interface leads to the trapping of π -states at the Fermi energy. The frustrated NS junction relaxes

through the generation of spontaneous interface currents, inducing a paramagnetic moment. The spontaneous magnetization implies a first order transition in zero field in the low-temperature sector of the $H - T$ phase diagram. A non-trivial issue remains the requirement that the electron-electron interaction be repulsive at the low energy scales involved. Interesting consequences of this assumption have been discussed in the context of the proximity effect [de Gennes 1964] and most recently in relation to the low temperature transport in mesoscopic NS structures [Petrashov 1995, Nazarov 1996]. In fact, the noble metal coatings used in the experiments of Mota and co-workers [Visani 1990a] appear to be the most plausible candidates for a repulsive electron-electron interaction. Turning the argument around, in the light of our findings the experimental observation of a paramagnetic reentrance can be taken as an indication of the presence of a repulsive interaction in these materials.

Chapter 6

Nonlocality in Josephson junctions: Anomalous current – flux periodicity

6.1 Introduction

The equilibrium transport in Josephson junctions is caused by the quantum interference of the two overlapping reservoir wavefunctions [Josephson 1962]. The supercurrent is driven by the nonlocal phase difference between the superconducting leads. This is of particular interest in superconductor–normal-metal–superconductor (SNS) junctions, where the thickness of the interlayer can be much larger than the superconducting coherence length ξ_0 , without suppressing the Josephson current. The transport relies on the coherence of the quasi-particle population between the superconductors, on the mesoscopic scale of the thermal and phase coherence lengths of the normal metal [Likharev 1979].

In early studies on SNS junctions [Kulik 1970] the supercurrents were already expressed in terms of the quasi-particles which are bound to the interlayer due to the Andreev reflection. These bound states consist of a forward propagating electron and a back propagating hole and carry the current of the double electron charge $2e$, which is converted from an to supercurrent at the NS interfaces. Recently, there has been a renewed interest in those states as they can be brought out of equilibrium in a controlled fashion [Octavio 1983, Averin 1995, Gorelik 1998, Lehnert 1999]. Due to the advances in nanofabrication technology, which have achieved a good coupling of a two-dimensional electron gas (2DEG) to superconducting reservoirs [Takayanagi 1995a, Takayanagi 1995b], ballistic properties of these quasi-particles like the quantization of supercurrent [Beenakker 1991] have been observed.

In the present chapter we determine the critical-current–flux relation in a ballistic

SNS junction. The current-carrying quasi-particles traversing the weak link are sensitive to the Aharonov-Bohm phase, producing a nonlocal dependence of the current density on the magnetic induction in the junction and the superconducting phase difference. As a consequence, the nonlocality and the finite size junction produce an anomalous doubling of the critical-current-flux periodicity $I_c(\Phi)$.

The motivation for our work is drawn from an experiment on S-2DEG-S junctions [Heida 1998] of width w comparable to length d , where the a $2\Phi_0$ periodicity was found instead of the usual Φ_0 . A first attempt to explain this finding is due to [Barzykin 1998]; considering the point-contact geometry of Fig. 1(a) with open boundary condition in the metal, they indeed recover a $2\Phi_0$ periodicity for a geometric ratio $w/d \rightarrow 0$. However, the experiment in [Heida 1998] is carried out in the strip geometry of Fig. 1(b) and involves dimensions $w \sim d$ of the same order. Here we determine the critical current I_c as a function of flux, taking proper account of the reflecting boundaries in the normal-metal characteristic for the strip geometry of Fig. 6.1(b). We find that the periodicity of the critical current changes from Φ_0 to $2\Phi_0$ as the flux through the junction increases, i.e., as a function of field. At low temperatures the crossover to the $2\Phi_0$ periodic current appears at a flux $\sim \Phi_0 w/d$, thus explaining the result of Heida *et al.* [Heida 1998], who found a $2\Phi_0$ periodic pattern for all fields in devices with $w/d \sim 1$. The results of this chapter have been accepted for publication [Ledermann 1999].

6.2 Current density pattern

In our study, we neglect the screening of the applied fields by the supercurrent in the normal-metal layer, which is justified for a small critical current j_c . The scale over which the fields can be screened is given by the Josephson length

$$\lambda_J \sim \sqrt{c\Phi_0/j_c}, \quad (6.1)$$

where $\tilde{d} = d + 2\lambda_S$ is the effective length of the junction, extended by the penetration depth λ_S in the superconductors. We assume that the Josephson vortex distance [Tinkham 1996],

$$a_0 = \Phi_0/\tilde{d}, \quad (6.2)$$

is the smaller length scale, $a_0 \ll \lambda_J$. Expressing the critical current by the screening density $n \propto 1/\lambda_N(T)^2$ introduced in Chp. 3, $j_c \sim c\Phi_0/\lambda_N^2(T)d$, we find that the field regime of interest lies above the 'critical field' of the normal interlayer, $H \gg \Phi_0/\lambda_N(T)d$. We consider the SNS-junction sketched in Fig. 6.1. In the quasi-classical Green's function technique, the current density (3.6) in a point P results from the contributions over all quasi-particle *trajectories* connecting the two NS interfaces through P . In a junction of infinite width, the trajectories involve no

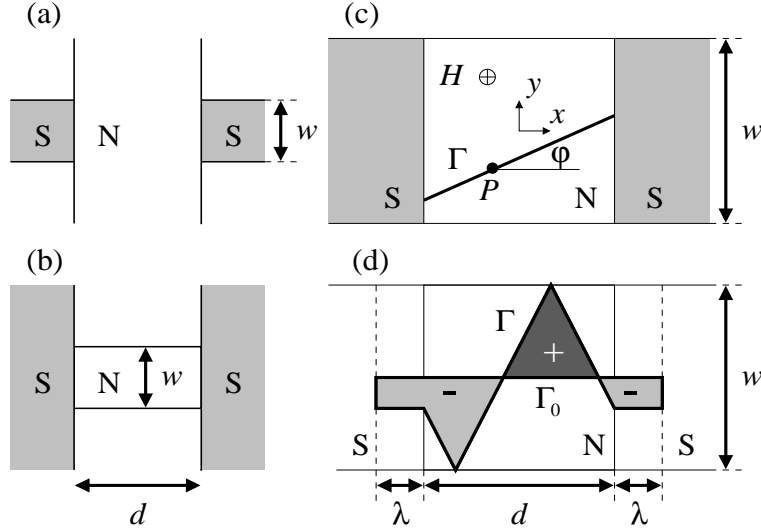


Figure 6.1: (a) Junction with a point-contact (open) geometry as discussed in [10], where w is the width of the two *superconductors*. (b) The junction studied here has a strip geometry with w the width of the *normal* conductor. (c) The magnetic field H is applied in the z -direction and the coordinate system is chosen symmetric with respect to the junction center. The current density in the point P involves contributions from all trajectories Γ parameterized by the angle φ . (d) The phase difference γ along the trajectory Γ can be expressed through the enclosed flux ϕ ; using the trajectory Γ_0 as our reference, the flux through the areas above (below) Γ_0 contributes with a positive (negative) sign.

reflection at the boundaries. In the case of a finite junction, boundary conditions at the normal-metal–vacuum boundary have to be applied, which we idealize through the assumption of specular reflections. Furthermore, we adopt the usual approximations: perfect Andreev reflections at the SN-interfaces and a coherence length ξ_0 in the two superconductors with $\xi_0 \ll d$, allowing for a step-like approximation of the order parameter Δ [Kulik 1970]. The quasi-classical Green function is calculated by matching the partial solutions in N and S at the interfaces. For the current density \mathbf{j} , we arrive at a generalization of the results given by Svidzinskii and co-workers [Antsygina 1975]. For finite temperatures with $d \gg \xi_N$, the current \mathbf{j} takes the form,

$$\frac{\mathbf{j}(x, y)}{j_{c,0}} = -\frac{6}{\pi} \sqrt{\frac{2}{\pi}} \int_{-\pi/2}^{\pi/2} d\varphi \hat{\mathbf{p}} \sin(\gamma) \frac{d}{\sqrt{\xi_N l(\varphi)}} \exp\left(-\frac{l(\varphi)}{\xi_N}\right), \quad (6.3)$$

while in the low temperature limit, $d \ll \xi_N$,

$$\frac{\mathbf{j}(x, y)}{j_{c,0}} = \frac{4}{\pi^2} \sum_{k=1}^{\infty} \frac{(-1)^k}{k} \int_{-\pi/2}^{\pi/2} d\varphi \hat{\mathbf{p}} \sin(k\gamma) \frac{d}{l(\varphi)}, \quad (6.4)$$

where $\hat{\mathbf{p}} = (\cos(\varphi), \sin(\varphi), 0)$, $l(\varphi) = d/\cos(\varphi)$ is the length of a trajectory with slope φ , and the zero temperature critical current density is

$$j_{c,0} = \frac{ne^2 \Phi_0}{mc 2d}. \quad (6.5)$$

In (6.5), n denotes the electron density in the normal metal, and we have assumed $T \ll \Delta$ as usual. While in the low temperature limit all harmonics $\sin(k\gamma)$ ($k = 1, 2, \dots$) contribute to the current density [Ishii 1970], at finite temperatures, the thermal smearing of the Andreev levels leads to a suppression of the higher harmonics $\propto \exp(-kd/\xi_N)$ and only the first term $\propto \sin(\gamma)$ survives. An individual trajectory contributes with a weight $\propto \exp(-l/\xi_N)$ at finite- and $\propto d/l$ in the low temperature limit. In a wide junction, γ takes the form¹ [Antsygina 1975],

$$\gamma(x, y; \varphi) = \gamma_0 - \frac{2\pi}{\Phi_0} H\tilde{d} [y - x \tan(\varphi)]. \quad (6.6)$$

In the more general result derived here, γ is given by the gauge invariant phase difference

$$\gamma(x, y; \varphi) = \Delta\varphi - \frac{2\pi}{\Phi_0} \int_{\Gamma} \mathbf{A} \cdot d\mathbf{s}, \quad (6.7)$$

where $\Delta\varphi$ denotes the phase difference between the two superconductors and Γ is the path which goes through the point (x, y) with slope φ . Combining the current expressions (6.3) or (6.4) and (6.7) with the Maxwell equation $\nabla^2 \mathbf{A} = -4\pi\mathbf{j}[\mathbf{A}, \Delta\varphi]/c$, we obtain the transverse vector-potential \mathbf{A} allowing to solve the full screening problem. The solution of the screening problem has only been carried out for a tunnel junction so far [Owen 1967].

In the following, we neglect screening and concentrate on junctions with the strip geometry of Fig. 6.1(b), including the (reflecting) trajectories Γ in (6.3) and (6.4). We express the gauge invariant phase difference (6.7) in terms of the flux ϕ enclosed by Γ and the reference path Γ_0 and obtain,

$$\gamma(x, y; \varphi) = \gamma_0 - \frac{2\pi\phi(x, y; \varphi)}{\Phi_0}, \quad (6.8)$$

¹ In the discussion of the point-contact geometry, Barzykin and Zagoskin make use of the above results, but limit the integration in (6.3) and (6.4) to those trajectories connecting the superconducting contacts [Barzykin 1998].

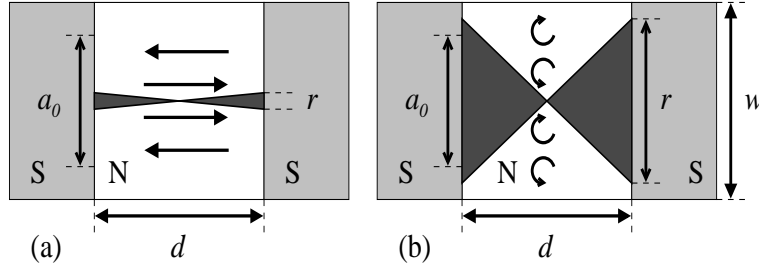


Figure 6.2: The ‘bow ties’ of width r display the ensemble of trajectories contributing to the current density in a given point. The arrows indicate the current flow. (a) For weak nonlocality, $r < a_0$, the current flows straight through the junction. (b) The strong nonlocality, $r > a_0$, leads to the formation of vortex-like domains of circular flow.

where for negligible screening $\phi(x, y; \varphi) = HS(x, y; \varphi)$ and S is the properly weighted enclosed area, see Fig. 6.1(d). Note the analogy of this result to the Aharonov-Bohm phase picked up by an Andreev loop in a SN structure, see Fig. 4.2. The surface S is calculated as a function of the number of reflections the trajectory Γ undergoes (in the following called the ‘order’ of the trajectory). The point-contact geometry of Fig. 6.1(a) then is described by the order-zero trajectories alone [Barzykin 1998], while in the strip geometry of Fig. 6.1(b), higher orders have to be included.

The geometrical pattern in the current density \mathbf{j} depends strongly on the sample dimensions d and w , the normal metal coherence length ξ_N , and the applied field H . At finite temperature, the current density in P draws its weight from trajectories with $\varphi < \sqrt{\xi_N/d}$, allowing us to introduce the transverse nonlocality range $r = \sqrt{\xi_N d}$ (in the low temperature limit, $\varphi \sim 1$ and we define $r = d$). This range of nonlocality has to be compared to the scale $a_0 = \Phi_0/H\tilde{d}$ of transverse variations in \mathbf{j} (see Fig. 6.2): For *weak* nonlocality, $r < a_0$, the flow is uniform along x with amplitude j_c and changes direction on a distance $a_0/2$ along the y -axis. This contrasts with the *strongly* nonlocal case $r > a_0$ which is found with increasing field, where the current density forms domains of left- and right-going circular flow. While the local case is similar to that in a tunnel junction, the pattern in the *nonlocal* situation reminds of the usual vortex structure in a superconductor, see Fig. 6.3. For finite temperatures with $d \gg \xi_N$, the current density of the order-zero trajectories is given by

$$\begin{aligned} \frac{j_x(x, y)}{j_{c,0}} &= -\frac{12}{\pi} \sin\left(\gamma_0 - \frac{2\pi y}{a_0}\right) \exp[-\alpha(x)], \\ \frac{j_y(x, y)}{j_{c,0}} &= -\frac{12}{\pi} \cos\left(\gamma_0 - \frac{2\pi y}{a_0}\right) \frac{\xi_N}{d} \frac{2\pi x}{a_0} \exp[-\alpha(x)], \end{aligned} \quad (6.9)$$

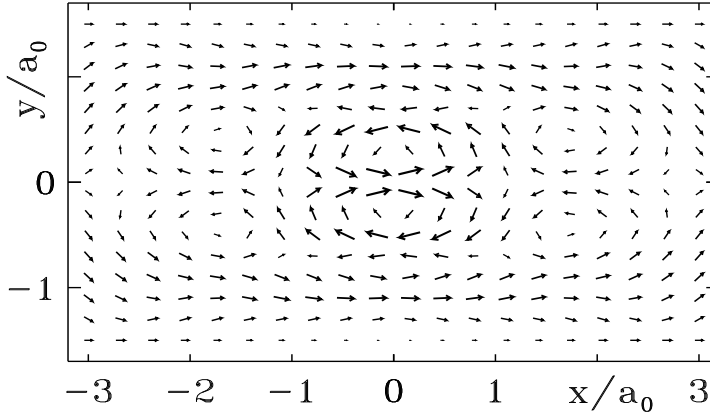


Figure 6.3: The current density for $d/\xi_N = 3$, $r/a_0 \approx 3.5$, and $\Phi/\Phi_0 = 3$. Apart from the vortex-like domains in the middle produced by order-zero trajectories, additional circular flow is set up by the order-one trajectories.

where

$$\alpha(x) = \sqrt{\left(\frac{d}{\xi_N}\right)^2 + \left(\frac{2\pi x}{a_0}\right)^2}. \quad (6.10)$$

For weak nonlocality, $a_0 < r$, the exponent remains approximately constant in the normal part, $\alpha(x) \approx \alpha(0)$, leading to a uniform current flow, while for strong nonlocality, $a_0 > r$, $\alpha(x)$ grows as x approaches the interfaces, $\alpha(\pm d/2) \gg \alpha(0)$, such that the current concentrates in the middle of the junction. For $a_0 > r$, the higher order trajectories lead to a refinement of the current pattern, see Fig. 6.3. Similar results are obtained in the low temperature limit, see [Ledermann 1998].

6.3 Critical current – flux dependence

The ratio r/a_0 and its associated characteristic current pattern manifest themselves in the (pseudo)-periodicity of the critical current,

$$I_c(\Phi) = \max_{\gamma_0} \int_{-w/2}^{w/2} dy j_x(0, y; \gamma_0, \Phi), \quad (6.11)$$

versus flux $\Phi = H\tilde{d}w$ in the junction. In the case of weak nonlocality, $r < a_0$, the relevant contribution to the critical current comes from the order-zero trajectories resulting in a Φ_0 periodicity. For strong nonlocality, $r > a_0$, higher orders are relevant and *lift* the order-zero result as shown in Fig. 6.4 — the periodicity of the

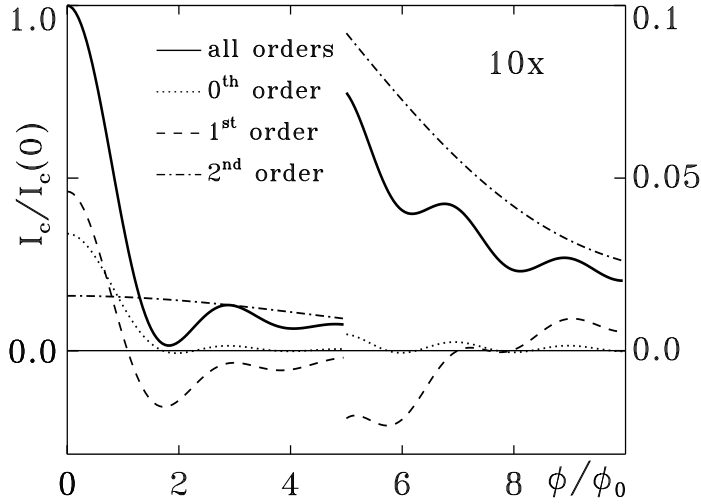


Figure 6.4: The critical current for $d/\xi_N = 5$ and $w/d = 1/3$. The solid curve shows the full critical current and the dashed curves are the contributions from the orders 0, 1, and 2. The orders 0 and 1 oscillate with periodicity $2\Phi_0$, while the second order decreases monotonically, remaining always positive. The current pattern produced by the orders 0 and 1 is lifted by the order 2 contributions, and the critical current attains the periodicity $2\Phi_0$.

critical current changes to $2\Phi_0$. For a critical current $j_c < \Phi_0/cd$ the cross-over $a_0 \sim r$ lies within the negligible screening regime. To be specific, we discuss in detail the orders 0, 1, and 2 for the case of finite temperatures with $d \gg \xi_N$ (the qualitative arguments for $d \ll \xi_N$ are similar).

For $w > r > a_0$, the critical current due to the order-zero trajectories takes the form

$$I_c^{(0)}(\Phi) = -\frac{\sqrt{2}I_{c,T}}{\sqrt{\pi}} \frac{w}{r} \frac{\cos(\pi\Phi/\Phi_0)}{(\pi\Phi/\Phi_0)^2}, \quad (6.12)$$

where $I_{c,T} = w(12/\pi)j_{c,0} \exp[-d/\xi_N(T)]$. For the first-order trajectories, we numerically find a $2\Phi_0$ (pseudo-) periodic contribution as well. Both components vanish with field $\propto 1/\Phi^2$. The second- and all following even-order trajectories exhibit a large current amplitude of order j_c on a scale $a_0 \propto 1/\Phi$ in the junction center $(0, 0)$, a consequence of the φ -independence of the gauge invariant phase difference γ along trajectories through $(0, 0)$. Their contribution scales $\propto 1/\Phi$ and therefore dominates over the zeroth- and first-order terms at large enough fields — as the strongly non-local limit with $a_0 < r$ is reached, the periodicity changes to $2\Phi_0$. Samples with a small width $w < r$ are always in the strongly nonlocal limit and their current pattern

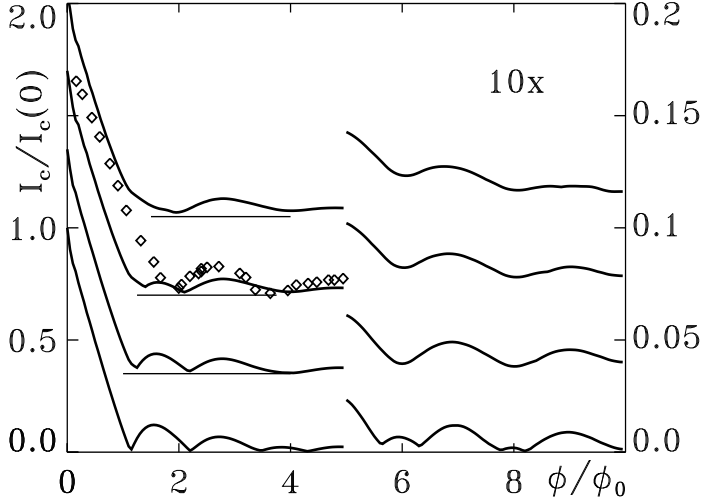


Figure 6.5: The critical current in the low temperature limit, $d \ll \xi_N$, for $w/d = 0.8, 0.9, 1.1, 1.5$ (from top to bottom). Successive plots have been offset by 0.35. Measured data ([9], diamonds) is shown for the case $w/d = 0.9$.

is $2\Phi_0$ periodic throughout the entire field axis. At low temperatures, the condition $w < r$ transforms into the geometric requirement $w < d$. The same arguments apply for the $r > w > a_0$, where the zero-order current is given by [Heida 1998]

$$I_c^{(0)}(\Phi) = -\frac{I_{c,T}}{2\sqrt{\pi}} \frac{w}{r} \left(\frac{\sin(\pi\Phi/2\Phi_0)}{\pi\Phi/2\Phi_0} \right)^2. \quad (6.13)$$

While Eq. (6.13) trivially implies a $2\Phi_0$ periodicity when taking the absolute value, more generally Eq. (6.12) only produces a $2\Phi_0$ periodicity when accounting for the lifting by the higher order contributions. We give a complete classification of the regimes of simple or double flux periodicity, depending on the nonlocality range r , and the Josephson vortex distance a_0 in Table 6.1.

6.4 Discussion

We have demonstrated that the current density and the critical current in a clean SNS-junction with strip geometry depend on the ratio r/a_0 between the nonlocality range r and the vortex distance a_0 . The period of the critical current changes with increasing field from a Φ_0 periodicity for $a_0 > r$ to a $2\Phi_0$ pseudo-periodicity for strong nonlocality $a_0 < r$.

Recently, Heida *et al.* [Heida 1998] observed such a $2\Phi_0$ periodicity in strip like ($w \sim d$) S-2DEG-S junctions made from Nb electrodes in contact with InAs

operating at low temperatures $T = 0.1$ K. As the total flux through the junction is difficult to determine in the experiment, Heida *et al.* had to infer their $2\Phi_0$ periodic structure from a fit on four samples with different ratios w/d ranging from 0.9 to 2.2. In Fig. 6.5, we present the results of our numerical calculations for the strip geometry, where we have properly taken into account the finite penetration depth of the flux into the superconducting banks. While geometries with $w/d < 1$ clearly exhibit a $2\Phi_0$ periodicity throughout the entire field region, a Φ_0 -component starts to develop at low fields in wide junctions. The comparison with the data of Heida *et al.* ($w/d = 0.9$) gives a satisfactory description of the pseudo-periodic structure.

For further experimental studies on wider junctions, we predict a crossover from a Φ_0 - to a $2\Phi_0$ -periodicity with increasing fields. The cross-over is accompanied by the detachment of the current pattern from the superconducting leads, which form a vortex structure shown in Fig. 6.3.

Table 6.1: The periodicity of the critical current is controlled by the parameters w/r , and r/a_0 . The table has to be read as a flow chart, starting at the top row and selecting the proper condition proceeding down the rows. The nonlocality range is given by $r = \sqrt{\xi_N(T)d}$ for $\xi_N(T) \ll d$ and $r = d$ for $\xi_N(T) \gg d$.

ratio	value	
w/r	> 1	< 1
r/a_0	< 1	> 1
period	Φ_0	$2\Phi_0$

Chapter 7

Quiet SDS Josephson junctions for quantum computing

7.1 Introduction

Quantum computers take advantage of the inherent parallelism of the quantum state propagation, allowing them to outperform classical computers in a qualitative manner. Although the concept of quantum computation has been introduced quite a while ago [Feynman 1996], wide spread interest has developed only recently when specific algorithms exploiting the character of coherent state propagation have been proposed [Ekert 1996]. Here we deal with the device aspect of quantum computers, which is flourishing in the wake of the recent successes achieved on the algorithmic side. Two conflicting difficulties have to be faced by all hardware implementations of quantum computation: while the computer must be scalable and controllable, the device should be almost completely detached from the environment during operation in order to maximize phase coherence. The most advanced propositions are based on trapped ions [Cirac 1995, Monroe 1995], photons in cavities [Turchette 1995], NMR spectroscopy of molecules [Gershenfeld 1997], and various solid state implementations based on electrons trapped in quantum dots [Loss 1998, Burkard 1999], the Coulomb blockade in superconducting junction arrays [Shnirman 1997, Shnirman 1998, Averin 1998], or the flux dynamics in Superconducting Quantum Interference Devices (SQUIDs) [Bocko 1997]. Nanostructured solid state quantum gates offer the attractive feature of large scale integrability, once the limitations due to decoherence can be overcome [Haroche 1996].

In this chapter we propose a new device concept for a (quantum) logic gate exploiting the unusual symmetry properties of unconventional superconductors. The basic idea is sketched in Fig. 1: connecting the positive (100) and negative (010) lobes of a d -wave superconductor with a s -wave material produces the famous

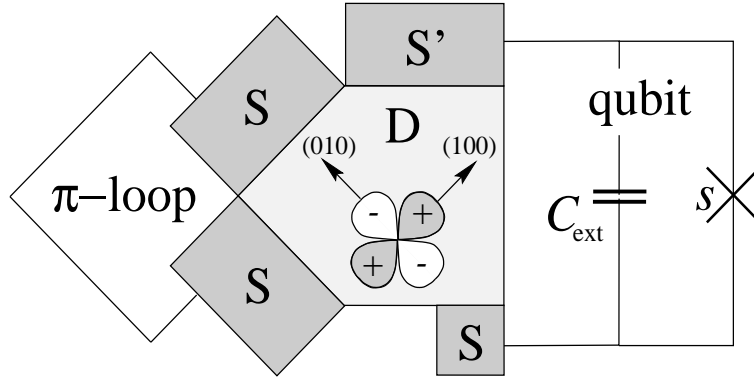


Figure 7.1: Geometrical arrangements between s -wave and d -wave superconductors producing a π -loop (used in the phase sensitive experiment by Wollman *et al.* [1]) and a qubit, the basic building block of a quantum computer.

π -loop with a current carrying ground state characteristic of d -wave symmetry [Wollman 1993, Sigrist 1995]. We make use of an alternative geometry and match the s -wave superconductors (S) to the (110) boundaries of the d -wave (D) material. As a consequence, the usual Josephson coupling $\propto (1 - \cos \phi)$ vanishes due to symmetry reasons and we arrive at a bistable device, where the leading term in the coupling takes the form $E_d \cos 2\phi$ with minima at $\phi = \pm\pi/2$ (ϕ denotes the gauge invariant phase drop across the junction). In our design we need the minima at the positions $\phi = 0, \pi$ — the necessary shift is achieved by going over to an asymmetric SDS' junction with a large DS' coupling, see Fig. 1. The static DS' junction shifts the minima of the active SD junction by the desired amount $\phi = \pm\pi/2$. A similar double-periodic junction has recently been realized by combining two d -wave superconductors oriented at a 45° angle [Il'ichev 1998]. The ground states of our SDS' junction are degenerate and carry no current, while still being distinguishable from one another: e.g., connecting the junction to a large inductance loop, the π state is easily identified through the induced current. It is this double-periodicity and the associated degeneracy in the ground state of the SDS' junction which we want to exploit here for quantum computation: combining the SDS' junction, a capacitor, and a conventional s -wave junction into a SDS' SQUID loop, we construct a bistable element which satisfies all the requirements for a qubit, the basic building block of a quantum computer. This work has been submitted for publication [Ioffe 1998].

7.2 Device functionality

In the following we give a detailed account of the operational features of our device. Consider a small-inductance (L) SQUID loop with $I_J L \ll \Phi_0$, where I_J denotes the (Josephson) critical current of the loop and $\Phi_0 = hc/2e$ is the quantum unit of flux. Such a loop cannot trap magnetic flux ($\Phi = 0$) and the gauge invariant phase differences ϕ_1 and ϕ_2 across the two junctions are slaved to each other, as the uniqueness of the wave function requires that $\phi_1 - \phi_2 = 2\pi\Phi/\Phi_0$. Combining a SDS' junction with a coupling energy E_d and a conventional s -wave junction (coupling E_s) into a SDS' SQUID loop, we obtain a potential energy

$$V(\phi) = E_d(1 - \cos 2\phi) + E_s(1 - \cos \phi), \quad (7.1)$$

exhibiting two minima at $\phi = 0, \pi$, see Fig. 2. The switch s allows us to manipulate their energy separation, choosing between minima which are either degenerate or separated by $2E_s$.

In the quantum case, the phase fluctuates as a consequence of the particle–phase duality [Tinkham 1996]. The phase fluctuations are driven by the electrostatic energy required to move a Cooper pair across the junction and are described by the kinetic energy

$$T(\dot{\phi}) = (\hbar/2e)^2 C \dot{\phi}^2 / 2, \quad (7.2)$$

where C denotes the loop capacitance. The dynamics of ϕ is manipulated by inserting a large switchable (switch c) capacitance C_{ext} into the loop acting in parallel with the capacitances C_d and C_s of the d - and s -wave junctions. Note that the Lagrangian $L = T - V$ of our loop is formally equivalent to that of a particle with ‘mass’ $m \propto C$ moving in the potential $V(\phi)$.

With the switch settings c on and s off, see Fig. 2(a), the loop capacitance is large and the junction exhibits a doubly degenerate ground state which we characterize via the phase coordinate ϕ , $|0\rangle$ and $|\pi\rangle$. Closing the switch s , see Fig. 2(b), the degeneracy is lifted and while $|0\rangle$ becomes the new ground state, the $|\pi\rangle$ -state is shifted upwards by the energy $2E_s$ of the s -wave junction, the latter being frustrated when $\phi = \pi$. On the other hand, opening the switch c , see Fig. 2(c), completely isolates the d -wave junction and leads to the new ground and excited states $|\pm\rangle = [|0\rangle \pm |\pi\rangle]/\sqrt{2}$ separated by the tunneling gap $2\Delta_d$. The latter relates to the barrier $2E_d$ and the capacitance C_d of the d -wave junction via [Tinkham 1996]

$$\Delta_d \propto E_d \exp(-2\sqrt{C_d E_d / e^2}). \quad (7.3)$$

Closing the switch c , the capacitance is increased by C_{ext} and the tunneling gap is exponentially suppressed. Using the above three settings, we can perform all the necessary single qubit operations:

Idle-state: The switch settings *c-on* and *s-off* define the qubit's idle-state. While the large capacitance C_{ext} inhibits tunneling, the degeneracy of $|0\rangle$ and $|\pi\rangle$ guarantees a parallel time evolution of the two states. This idle-state is superior to other designs, where the two states of the qubit have *different* energies and one has to keep track of the relative phase accumulated between the basis states.

Phase shifter: Closing the switch *s* separates the energies of the basis states $|0\rangle$ and $|\pi\rangle$ by an amount $2E_s$. Using a spinor notation for the two-level system, the relative time evolution of the two states is described by the Hamiltonian $\mathcal{H}_s = -E_s\sigma_z$, with σ_z a Pauli matrix. Keeping the switch *s on* during the time t , the time evolution of the two states is given by the unitary rotation $u_z(\varphi) = \exp(-i\sigma_z\varphi/2)$ with $\varphi = -2E_s t/\hbar$.

Amplitude shifter: Assume we have prepared the loop in the ground state $|0\rangle$ and wish to produce a superposition by shifting some weight to the $|\pi\rangle$ state. Opening the switch *c* in the loop, see Fig. 2(c), the time evolution generated by the Hamiltonian $\mathcal{H}_d = \Delta_d\sigma_x$ of the open loop induces the rotation $u_x(\vartheta) = \exp(-i\sigma_x\vartheta/2)$ with $\vartheta = 2\Delta_d t/\hbar$. The system then oscillates back and forth between $|0\rangle$ and $|\pi\rangle$ with frequency $\omega = \Delta_d/\hbar$ and keeping the switch *c* open for an appropriate time interval t we obtain the desired shift in amplitude (note that the qubit remains isolated from the environment during these Rabi oscillations).

Imposing the condition $E_d \gg E_s, \Delta_d$ on the coupling energies, we make sure that the two states $|0\rangle$ and $|\pi\rangle$ are well defined while simultaneously involving only the low energy states $|0\rangle$ and $|\pi\rangle$ of the system. Furthermore, all times involved should be smaller than the decoherence time τ_{dec} , requiring $E_s, \Delta_d \gg \hbar/\tau_{\text{dec}}$.

The present setup differs significantly from the conventional (large inductance) SQUID loop design, where the low-lying states are distinguished via the different amount of trapped flux and their manipulation involves external magnetic fields H or biasing currents I citeblatter:qtunneling. SQUID loops of this type are being used in the design of classical Josephson junction computers [Likharev 1991] and have been proposed for the realization of quantum computers, too, see [Bocko 1997]. However, this setup suffers from the generic problem that the flux moving between the loops leads to a magnetic field mediated long-ranged interaction between the individual loops and further produces an unwanted coupling to the environment. By contrast, our device remains decoupled from the environment, the operating states do not involve currents, and switching between states can be triggered with a minimal contact to the external world — we therefore call our qubit implementation a ‘*quiet*’ one.

Next, we discuss how to perform two-qubit operations within an array of SDS' SQUID loops. A two-qubit state is a coherent superposition of single qubit states and can be expressed in the basis $\{|xy\rangle\}$, where $x, y \in \{0, \pi\}$ denote the phases on the *d*-wave junctions of the first (x) and second (y) qubit, respectively. Unitary operations acting on these states are represented as 4×4 unitary matrices. Single-

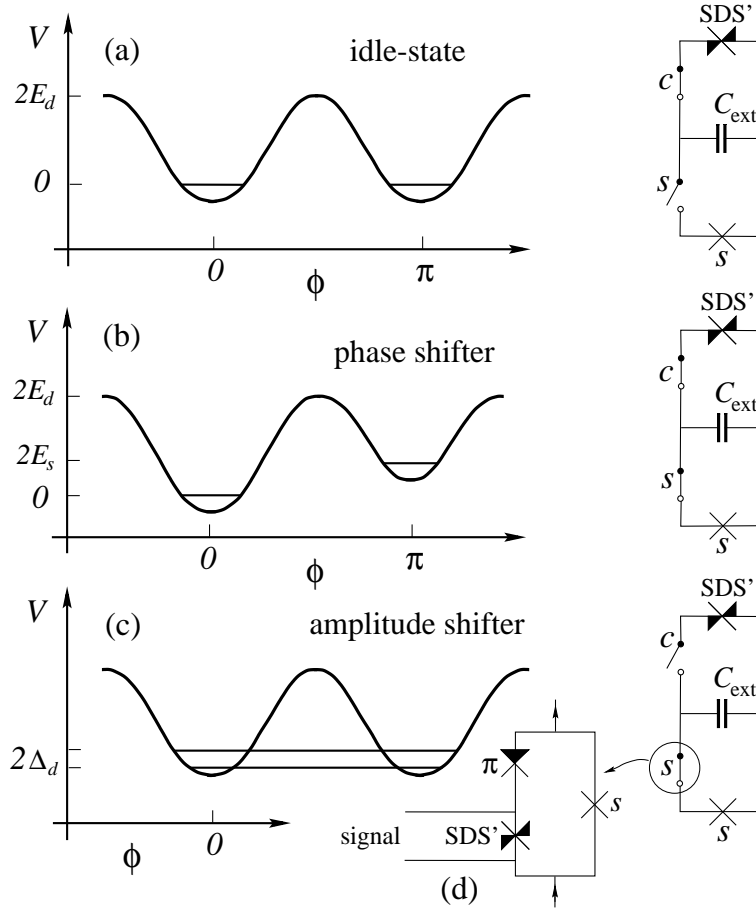


Figure 7.2: Energy–phase diagrams for the SDS' SQUID loop. (a) Idle-state: The switches are set to *c-on* and *s-off* — the relative dynamics is quenched, leaving the state unchanged. (b) Phase-shifter: With the switch settings *c-on* and *s-on* the relative phase between $|0\rangle$ and $|\pi\rangle$ increases linearly with time. (c) Amplitude-shifter: The switch setting *c-off* isolates the *d*-wave junction. An initial state $|0\rangle$ oscillates back and forth between $|0\rangle$ and $|\pi\rangle$, allowing for a shift of amplitude. (d) A SDS' junction, a π junction, and a *s*-wave junction combined into a SQUID loop and serving as a switch.

qubit operations u acting on the second qubit take the block-matrix form

$$\mathcal{U}_2 = \begin{pmatrix} u & 0 \\ 0 & u \end{pmatrix}, \quad (7.4)$$

and a similar block form selecting odd and even rows and columns defines the single-qubit operations on the first qubit. As all logic operations on two qubits can be

constructed from combinations of single-qubit operations and the Controlled-NOT gate [Ekert 1996] it is sufficient to define the operational realization of the latter. The Controlled NOT gate performs the following action on two qubits: with the first (controller) qubit in state $|x\rangle$ and the second (target qubit) in state $|y\rangle$ the operation shall leave the target qubit unchanged if $x = 0$, while flipping it between 0 and π when $x = \pi$, in matrix notation

$$\mathcal{U}_{\text{CNOT}} = \begin{pmatrix} 1 & 0 \\ 0 & \sigma_x \end{pmatrix}. \quad (7.5)$$

The above Controlled NOT operation can easily be constructed from the two-qubit ‘phase shifter’: Connecting two individual qubits in their idle-state over a s -wave junction into a SQUID loop, the states $|00\rangle$ and $|\pi\pi\rangle$ become separated from the states $|0\pi\rangle$ and $|\pi 0\rangle$ by the energy $2E_{s_b}$ of the s -wave junction. Keeping the two qubits connected during the time t introduces a phase shift $\chi = -2E_{s_b}t/\hbar$ between the two pairs of states,

$$\mathcal{U}_{\text{ps}}(\chi) = \begin{pmatrix} u_z(\chi) & 0 \\ 0 & u_z(-\chi) \end{pmatrix}. \quad (7.6)$$

The Controlled NOT gate (7.5) then can be constructed from the phase-shifter (7.6) via the following sequence of single- and two-qubit operations (see [Loss 1998] for a similar realization of the CNOT gate),

$$\mathcal{U}_{\text{CNOT}} = \exp(-i\pi/4)\mathcal{U}_{2y}(\pi/2)\mathcal{U}_{1z}(-\pi/2)\mathcal{U}_{2z}(-\pi/2)\mathcal{U}_{\text{ps}}(\pi/2)\mathcal{U}_{2y}(-\pi/2), \quad (7.7)$$

where the single qubit operations $\mathcal{U}_{i\mu}(\theta)$ rotate the qubit i by an angle θ around the axis μ ($u_\mu(\theta) = \exp(-i\sigma_\mu\theta/2)$ acting on i) while leaving the other qubit unchanged.

A key element in our design are the switches and a valid suggestion is the single electron transistor discussed in the literature [Joyez 1994]. Here we propose a quiet switch design optimally adapted to our SDS’ qubits. The underlying idea is to insert a SQUID loop which allows to either stiffen or relax the phase, thus producing a phase switch. Combining a SDS’ junction with energy E_d , a π -junction with $E_\pi \ll E_d$, and a s -wave junction with $E_s = E_\pi$ into a (small inductance) SQUID loop, see Fig. 2(d), we obtain the following switching behavior: The phase $\phi = 0$ on the SDS’ junction frustrates the remaining junctions, the loop’s energy-phase relation is a constant, $E_{\text{sw}}(\phi_\pi = \phi_s - \pi) \equiv 0$, and the switch is open. A voltage pulse coming down the signal lines and switching the SDS’ junction into the $|\pi\rangle$ state changes the phase relation between the π - and the s -wave junctions and closes the switch: the energy $E_{\text{sw}}(\phi_\pi = \phi_s) = 2E_\pi(1 - \cos\phi_\pi)$ implies the current-phase relation $I = (2e/\hbar)\partial_{\phi_\pi}E_{\text{sw}}$ that stiffens the phase. The appropriate voltage pulses can be generated by driving an external SDS’ SQUID loop unstable.

7.3 Discussion

The quiet device concept proposed above heavily relies on the double periodicity of the SD junction. As the second harmonic is strongly suppressed in a SID tunnel junction, a more feasible suggestion for the realization of a $\cos 2\phi$ junction is the SND sandwich, where the superconductors are separated by a thin metallic layer N. For a clean metallic layer, the coupling energies for the n -th harmonic are large and of order $E_J \sim k_F^2 \mathcal{A} \hbar v_F / d$, producing the well known saw-tooth shape in the current-phase relation [Ishii 1970] (v_F denotes the Fermi velocity in the N layer while d and \mathcal{A} are its width and area). In reality, it seems difficult to deposit a *clean* metallic film on top of a d -wave superconductor and we have to account for the reduction in the coupling E_J due the finite scattering length l in the metal layer. Using quasi-classical techniques to describe a dirty SN_DD junction, we obtain a second harmonic coupling energy $E_d \sim k_F^2 \mathcal{A} (\hbar v_F / d) (l/d)^3 \sim (R_Q/R) (l/d) E_T$, where l denotes the scattering length in the normal metal, $R_Q = \hbar/e^2$ is the quantum resistance, and $E_T \sim (\hbar v_F / d) (l/d)$ is the Thouless energy.

The second important device parameter is the tunneling gap Δ_d , which depends quite sensitively on the coupling to the environment. The usual reduction in the tunneling probability produced by the environment [Caldeira 1983] is modified if the system is effectively gapped at low energies [Ambegaokar 1982]. This is the case for our SNDN'S' junction where the low-energy quasi-particle excitations in the metal are gapped over the Thouless energy E_T [Golubov 1988]. The dynamics of the junction is only affected by the presence of virtual processes involving energies larger than E_T , leading to a renormalized capacitance $C_{\text{ren}} \sim \hbar / R E_T$ (cf. [Schön 1990]) and resulting in the reduced tunneling gap

$$\Delta_d \propto E_d \exp[-\nu (R_Q/R) \sqrt{l/d}], \quad (7.8)$$

with ν of order unity. Consistency requires that the tunneling process is ‘massive’ and hence slow, $\hbar/\tau < E_T$. With a tunneling time $\tau \sim S/E_d$ ($S \sim \hbar (R_Q/R) \sqrt{l/d}$ = tunneling action) we find that the constraint $\hbar/\tau E_T \sim \sqrt{l/d} < 1$ is satisfied. The condition $\Delta_d \ll E_d$ requires the tunneling gap Δ_d to be small, but large enough in order to allow for reasonable switching times, requiring $(R_Q/R) \sqrt{l/d}$ to be of order 10. With typical device dimensions $d \sim 1000 \text{ \AA}$, $l \sim 10 \text{ \AA}$, and $R/R_Q \sim (d/l)(1/\mathcal{A}k_F^2) \sim 1/100$, this condition can be realized. Finally, the operating temperature T is limited by the constraint $S/\hbar > E_d/T$, guaranteeing that our device operates in the quantum regime, and the requirement $T < E_T$ that thermal quasi-particle excitations be absent. The first condition takes the form $T \ll \hbar/\tau \sim \sqrt{l/d} E_T$ and is the more stringent one. Using the above parameters and a typical value $v_F \sim 10^8 \text{ cm/s}$, we obtain a Thouless energy $E_T \sim 1 \text{ K}$ and hence $T \ll 0.1 \text{ K}$.

In conclusion, we have discussed a novel device concept for logic gates in superconducting computers. The SDS' SQUID loop realizes a number of attractive features which are potentially relevant both in classical Josephson computers based on RSFQ logics as well as in superconducting quantum computers. The most obvious advantage over previous designs is the quietness of the device: The SDS' SQUID loop is a naturally bistable device and does not involve external bias currents or magnetic fields. Second, the basic states of the loop do not involve currents or trapped flux, hence long-range interactions between various elements of the computer are eliminated. Third, the qubits do not accumulate phase differences during idle time. And fourth, all operations can be carried out via simple switching processes.

Chapter 8

Conclusions and Outlook

In this thesis, we have discovered the variety of facets of mesoscopic superconductivity induced by proximity, ranging from the non-equilibrium transport to the thermodynamic screening properties. A tremendous progress in nanofabrication technology and the perfection of low-temperature cryostats in the last two decades have made the small scales of the Andreev or Thouless energies accessible to experiment. Proximity induced superconductivity combines the macroscopic phase of the superconductor to the quantum coherence of the microscopic electron wavefunctions, allowing for the observation of single-particle properties on a macroscopic scale. The term 'mesoscopic' coins the importance of the phase coherence of the involved quasi-particles preserving quantum interference effects.

The study of mesoscopic superconductivity has repeatedly lead us to the microscopic process of the Andreev reflection (AR) governing the quasi-particle exchange across the normal-metal–superconductor contact. The AR pins the single-particle physics to the Fermi level, combining electrons above and holes below symmetrically. The non-trivial AR phase-shift $\pi/2$ translates into the suppression of the quasi-particle spectrum at the Fermi energy, the resonance structure in transport and the diamagnetic response in magnetism. These phenomena are understood in the idealized free electron gas description of the proximity metal, in good quantitative agreement with experiments.

In this concluding chapter, we give a perspective on open questions and future work on Andreev physics. On one hand we discuss some specific problems that can be addressed based on the framework provided in this thesis and are of direct relevance to experiments. On the other hand, we focus on some questions which appear of long term interest, in connection to our work and the present developments in the field of mesoscopic superconductivity.

(i) The scattering matrix approach used in chapter 2 gives a direct theoretical access to the finite voltage shot noise in NS junctions. The numerical realization of disorder average based on the shot noise expression would allow for a quantita-

tive comparison with shot noise experiments on diffusive NS junctions presently in progress [Jehl 1999, Kozhevnikov 1999].

(ii) In chapters 3 and 6 we have found several signatures of non-locality in the proximity effect, which have just started to be traced experimentally [Heida 1998]. We predicted a finite field cross-over from a Φ_0 to a $2\Phi_0$ current-flux periodicity in ballistic SNS junctions, and the detachment of the current pattern as we reach the non-local regime. Future experiments on more extended ballistic junctions will require the self-consistent solution of the screening problem, where the over-screening and the sensitivity to impurity or boundary scattering crystallizes in the critical-current-flux relation. Non-locality is also an issue in High- T_c superconductors, where the quasi-particle gap vanishes due to the d-wave symmetry of the order parameter, see [Kogan 1996].

(iii) The experimental feasibility of ballistic SNS weak links provides an access to non-equilibrium phenomena: The superconducting reservoirs act as a confining potential on the Andreev quasi-particle population which can be driven out of equilibrium in a controlled fashion [Scheer 1998]. This allows for the observation of supercurrents at large temperatures [Lehnert 1999] or the manipulation of the Josephson relation by a repopulation of the Andreev levels [Baselmans 1999]. The study of phase relaxation processes in this system are within experimental reach.

(iv) The rapidly developing area of quantum computing relies on the existence of phase coherent devices as it exploits the time evolution of a quantum two-level system (qubit). The Josephson junctions offer themselves as a scalable, solid state implementation of a qubit, by making use of the quantization of the charge [Shnirman 1997] or of the phase in mesoscopic weak links, see chapter 7. Before speculating on the efficient use of quantum algorithms, the near future challenge lies in the experimental realization of single- and two-qubit operations and in the theoretical investigation of the phase coherence problem, as it arises from the coupling with the environment.

(v) In chapters 4 and 5 we have addressed the nonlinear magnetic response in proximity structures, revealing a rich behavior in the low-temperature low-field corner of the $H - T$ phase diagram. The breakdown of the diamagnetic state studied in Chp. 4 was found to agree quantitatively with experimental data [Mota 1989]. The polarization of the spontaneous moments discussed in Chp. 5 (see also below) imply a similar phase boundary at zero field. We predict a latent heat as a signature of both first order transitions.

Much of the underlying motivation for the detailed study of the orbital magnetism in this thesis was provided by the paramagnetic reentrance observed in the susceptibility of normal-metal coated superconducting cylinders [Visani 1990a]. While the studies within the free electron gas approximation of Chps. 3 and 4 could not account for the low-temperature anomaly, they allowed a good characteriza-

tion of the typical mean free path and the quality of the NS interface, see also [Müller-Allinger 1999]. The effect of the cylindrical topology had already been previously considered in [Belzig 1995] using the quasi-classical technique, as well as more recently in [Bruder 1998], failing to produce either a non-monotonic temperature dependence or the order of magnitude observed in experiment. This prompted us to consider the possibility of a repulsive electron-electron interaction in the normal metal in Chp. 5. We found that a repulsive coupling constant in the normal metal layer frustrates the NS contact by a phase difference π across it. A density of states peak is accumulated at the Fermi energy due to the π -states trapped at the NS interface. This peak induces a paramagnetic instability towards spontaneous interface currents which naturally give rise to magnetic moments. The experimentally observed signatures being the paramagnetic reentrance in the susceptibility, a hysteretic behavior, dissipative response and creep qualitatively support our interpretation in terms of spontaneous magnetic moments and indicate the presence of repulsive electron-electron interactions in these materials (Ag, Cu). In order to test our ideas, the following points merit consideration.

(vi) The local spectroscopy of the NS contact by means of a (scanning) tunneling microscope should reveal a (split) density of states peak at the chemical potential.

(vii) The experimental measurement of the *dc*-magnetization curve would provide a direct evidence for our findings. For a quantitative comparison, the numerical solution of the Eilenberger equation is required, accounting for the self-consistency of the pair potential, the non-locality of the current-field relations that enter the Maxwell equation, and the presence of impurity scattering.

(ix) Recent theoretical work also addresses the low-temperature corrections to the proximity effect due to interactions [Zhou 1995, Nazarov 1996]. First experiments on ferromagnet–superconductor junctions show non-trivial behavior [Giroud 1998] challenging our understanding within the free electron gas approximation. A density of states peak at the Fermi level may affect the transport properties beyond the perturbative level that has been considered so far.

As experiments progress to ultra-low temperatures we unravel new facets of Andreev physics. The correlations induced by the proximity to a bulk superconductor could allow for the observation of metallic electron-electron interaction effects on a macroscopic scale. The low-temperature anomalies provide the opportunity to determine both the size and the sign of the coupling in these materials.

Appendix A

Bogoliubov-de Gennes equations

We diagonalize the BCS-Hamiltonian for superconductivity by a Bogoliubov transformation, considering a spatially inhomogeneous system. The transformation is carried out by determining the quasiparticle wavefunctions that fulfill the Bogoliubov-de Gennes (BdG) equations. We show that the symmetry in the solutions of the (BdG) equations with respect to reversing the energies $\epsilon_\alpha \rightarrow -\epsilon_\alpha$ is a consequence of the spin degeneracy. Making use of the spin-reversal symmetry, we express the Hamiltonian, the density, and the current operators in terms of the quasiparticle operators γ_α , and arrive at the current expression used in chapter 2.

The mean-field, spin singlet BCS Hamiltonian for superconductivity can be expressed in the form ($h_0 = (-i\nabla + e\mathbf{A})^2/2m$)

$$\mathcal{H} = \int d^3x : \hat{\Psi}^\dagger(\mathbf{x}) \begin{pmatrix} h_0 - \mu & \Delta \\ \Delta^* & -h_0^* + \mu \end{pmatrix} \hat{\Psi}(\mathbf{x}) : \quad (\text{A.1})$$

using the Nambu spin-up annihilation operator

$$\hat{\Psi}(\mathbf{x}) = \begin{pmatrix} \hat{\Psi}_\uparrow(\mathbf{x}) \\ \hat{\Psi}_\downarrow(\mathbf{x}) \end{pmatrix}. \quad (\text{A.2})$$

The pair potential is given by $\Delta(\mathbf{x}) = \lambda \langle \hat{\Psi}_\downarrow(\mathbf{x}) \hat{\Psi}_\uparrow(\mathbf{x}) \rangle$ (coupling constant λ), the colon ($:$) denoting normal ordering with respect to $\hat{\Psi}_\uparrow$ and $\hat{\Psi}_\downarrow$. The Hamiltonian (A.1) can be diagonalized by a basis transformation,

$$\hat{\Psi}(\mathbf{x}) = \sum_\alpha \Phi_\alpha(\mathbf{x}) \gamma_\alpha, \quad (\text{A.3})$$

$$\gamma_\alpha = \int d^3x \Phi_\alpha^\dagger(\mathbf{x}) \hat{\Psi}(\mathbf{x}), \quad (\text{A.4})$$

with the eigenfunctions $\Phi_\alpha(\mathbf{x})$ of the BdG equations (which follow from the insertion of the Hamiltonian (A.1) into $[\mathcal{H}, \gamma_\alpha] = -\epsilon_\alpha \gamma_\alpha$),

$$\begin{pmatrix} h_0 - \mu & \Delta \\ \Delta^* & -h_0^* + \mu \end{pmatrix} \Phi_\alpha(\mathbf{x}) = \epsilon_\alpha \Phi_\alpha(\mathbf{x}), \quad (\text{A.5})$$

$$\Phi_\alpha(\mathbf{x}) = \begin{pmatrix} u_\alpha \\ v_\alpha \end{pmatrix}.$$

Note that γ_α are annihilation operators of spin-up states and thus the excitations are all described in terms of spin-up quasi-particles. In order to preserve the (fermionic) commutation relations we need a complete orthonormal set of wavefunctions of the hermitian operator in (A.5),

$$\sum_\alpha \Phi_\alpha(\mathbf{x}) \Phi_\alpha^\dagger(\mathbf{x}') = \mathbf{1} \delta(\mathbf{x} - \mathbf{x}'), \quad (\text{A.6})$$

$$\int d^3x \Phi_\alpha^\dagger(\mathbf{x}) \Phi_{\alpha'}(\mathbf{x}) = \delta_{\alpha, \alpha'} \quad (\text{A.7})$$

(involving both positive and negative energy eigenstates)[Niño 1984].

Consider the spin-reversal transformation \mathcal{S} ,

$$\mathcal{S} \hat{\Psi} \mathcal{S}^{-1} = \begin{pmatrix} 0 & 1 \\ -1 & 0 \end{pmatrix} (\hat{\Psi}^\dagger)^\top, \quad (\text{A.8})$$

\mathcal{S} linear ($\mathcal{S} \hat{\psi}_\uparrow \mathcal{S}^{-1} = \hat{\psi}_\downarrow$, $\mathcal{S} \hat{\psi}_\downarrow \mathcal{S}^{-1} = -\hat{\psi}_\uparrow$). Noting that the order parameter $\Delta(\mathbf{x})$ is invariant under the transformation (A.8), it is easily seen that the Hamiltonian (A.1) is spin-reversal symmetric, $[\mathcal{H}, \mathcal{S}] = 0$ (this symmetry extends also to finite magnetic field, if the Zeeman splitting is neglected). By means of spin-reversal we may attribute to each quasi-particle operator γ_α a linearly independent operator $\gamma_{\bar{\alpha}}$ through

$$\gamma_{\bar{\alpha}}^\dagger = \mathcal{S} \gamma_\alpha \mathcal{S}^{-1} = \int d^3x \hat{\Psi}^\dagger(\mathbf{x}) \begin{pmatrix} 0 & -1 \\ 1 & 0 \end{pmatrix} \Phi_\alpha^*(\mathbf{x}). \quad (\text{A.9})$$

$\gamma_{\bar{\alpha}}$ describes an excitation with opposite energy $\epsilon_{\bar{\alpha}} = -\epsilon_\alpha$ (according to $[\mathcal{H}, \gamma_{\bar{\alpha}}] = \epsilon_\alpha \gamma_{\bar{\alpha}}$). From Eqs. (A.9) and (A.4) we infer the effect of spin-reversal on the electron-hole wavefunction,

$$\Phi_{\bar{\alpha}}(\mathbf{x}) = \begin{pmatrix} 0 & -1 \\ 1 & 0 \end{pmatrix} \Phi_\alpha^*(\mathbf{x}) = \begin{pmatrix} -v_\alpha^* \\ u_\alpha^* \end{pmatrix}. \quad (\text{A.10})$$

We arrive at a complete set of quasi-particle excitations in spin-up space, which are grouped into pairs $\gamma_\alpha, \gamma_{\bar{\alpha}}$ with energies $\pm\epsilon_\alpha$, as a direct consequence of spin degeneracy. Note that within the Nambu picture, all quasi-particles carry spin up

[spin $\uparrow e$ and spin $\uparrow h$ (instead of spin $\downarrow e$)], explaining the opposite energy of the related wavefunction (A.10). The Hamiltonian (A.1) takes the form,

$$\mathcal{H} = \sum_{\epsilon_\alpha > 0} \epsilon_\alpha \left(\gamma_\alpha^\dagger \gamma_\alpha + \gamma_{\bar{\alpha}} \gamma_{\bar{\alpha}}^\dagger - 2 \int d^3x |v_\alpha|^2 \right). \quad (\text{A.11})$$

The ground state is realized by filling all the negative energy quasi-particle states.

The spin-reversal symmetry allows us to express all equations using only half of the eigenstates, i.e., one representative Φ_n from each pair of states $\{\Phi_\alpha, \Phi_{\bar{\alpha}}\}$. In the following we choose the positive energy eigenstates, expressing the negative energy eigenstates through (A.10). We keep the positive energy states for the spin-up quasi-particles ($\gamma_n = \gamma_{n\uparrow}$), and reinterpret the related quasi-particle states of opposite (negative) energy as spin-down excitations ($\gamma_{\bar{n}} = \gamma_{\bar{n}\downarrow}^\dagger$). The Bogoliubov transformation (A.3) then takes the well-known form

$$\hat{\Psi}(\mathbf{x}) = \sum_n \begin{pmatrix} u_n \\ v_n \end{pmatrix} \gamma_{n\uparrow} + \begin{pmatrix} -v_n^* \\ u_n^* \end{pmatrix} \gamma_{\bar{n}\downarrow}^\dagger, \quad (\text{A.12})$$

and the Hamilton operator is expressed by $\mathcal{H} = \sum_{\epsilon_n > 0} \epsilon_n (\gamma_{n\uparrow}^\dagger \gamma_{n\uparrow} + \gamma_{\bar{n}\downarrow}^\dagger \gamma_{\bar{n}\downarrow} - 2 \int d^3x |v_n|^2)$, displaying the spin degeneracy in the usual fashion. In the same way, we give the density and current operators in both representations, using all (indexed by α) or only the positive energy eigenstates (indexed by n), respectively ($u \overset{\leftrightarrow}{\nabla} v = u \nabla v - (\nabla u)v$),

$$\begin{aligned} \rho(\mathbf{x}) &= -e : \hat{\Psi}^\dagger(\mathbf{x}) \begin{pmatrix} 1 & 0 \\ 0 & -1 \end{pmatrix} \hat{\Psi}(\mathbf{x}) : \\ &= -e \sum_{\alpha, \alpha'} (u_\alpha^*(\mathbf{x}) u_{\alpha'}(\mathbf{x}) \gamma_\alpha^\dagger \gamma_{\alpha'} + v_\alpha^*(\mathbf{x}) v_{\alpha'}(\mathbf{x}) \gamma_{\alpha'} \gamma_\alpha^\dagger) \end{aligned} \quad (\text{A.13})$$

$$\begin{aligned} &= -e \sum_{\epsilon_m, \epsilon_n > 0} [u_m^*(\mathbf{x}) u_n(\mathbf{x}) - v_m^*(\mathbf{x}) v_n(\mathbf{x})] (\gamma_{m\uparrow}^\dagger \gamma_{n\uparrow} + \gamma_{\bar{m}\downarrow}^\dagger \gamma_{\bar{n}\downarrow}) \\ &\quad - 2e \sum_{\epsilon_n > 0} |v_n(\mathbf{x})|^2 \\ &= -e \sum_{\epsilon_m, \epsilon_n > 0} \{ [u_m(\mathbf{x}) v_n(\mathbf{x}) + v_m(\mathbf{x}) u_n(\mathbf{x})] \gamma_{m\uparrow} \gamma_{\bar{n}\downarrow} + \text{h.c.} \}, \end{aligned} \quad (\text{A.14})$$

$$\begin{aligned} \mathbf{j}(\mathbf{x}) &= -\frac{e}{2mi} : \hat{\Psi}^\dagger(\mathbf{x}) \overset{\leftrightarrow}{\nabla} \hat{\Psi}(\mathbf{x}) : \\ &= -\frac{e}{2mi} \sum_{\alpha, \alpha'} u_\alpha^*(\mathbf{x}) \overset{\leftrightarrow}{\nabla} u_{\alpha'}(\mathbf{x}) \gamma_\alpha^\dagger \gamma_{\alpha'} - v_\alpha^*(\mathbf{x}) \overset{\leftrightarrow}{\nabla} v_{\alpha'}(\mathbf{x}) \gamma_{\alpha'} \gamma_\alpha^\dagger \\ &= -\frac{e}{2mi} \left\{ \sum_{\epsilon_m, \epsilon_n > 0} (u_m^*(\mathbf{x}) \overset{\leftrightarrow}{\nabla} u_n(\mathbf{x}) + v_m^*(\mathbf{x}) \overset{\leftrightarrow}{\nabla} v_n(\mathbf{x})) (\gamma_{m\uparrow}^\dagger \gamma_{n\uparrow} + \gamma_{\bar{m}\downarrow}^\dagger \gamma_{\bar{n}\downarrow}) \right\} \end{aligned} \quad (\text{A.15})$$

$$\begin{aligned}
& -2 \sum_{\epsilon_n > 0} v_n^*(\mathbf{x}) \overleftrightarrow{\nabla} v_n(\mathbf{x}) \\
& + \sum_{\epsilon_m, \epsilon_n > 0} \left[\left(-u_m(\mathbf{x}) \overleftrightarrow{\nabla} v_n(\mathbf{x}) + v_m(\mathbf{x}) \overleftrightarrow{\nabla} u_n(\mathbf{x}) \right) \gamma_{m\uparrow} \gamma_{\bar{n}\downarrow} - \text{h.c.} \right] \Bigg\}.
\end{aligned} \tag{A.16}$$

The current operator is easily generalized to finite magnetic field. We note that current and density operators obey the continuity equation

$$\frac{\partial \rho(\mathbf{x})}{\partial t} + \nabla \cdot \mathbf{j}(\mathbf{x}) = 2ie \hat{\Psi}^\dagger(\mathbf{x}) \begin{pmatrix} 0 & \Delta(\mathbf{x}) \\ -\Delta^*(\mathbf{x}) & 0 \end{pmatrix} \hat{\Psi}(\mathbf{x}). \tag{A.17}$$

Clearly, in the presence of the pair potential Δ the single quasi-particle currents are not conserved. However, as the right hand side of (A.17) vanishes when taking the self-consistent expectation value, the total current is conserved, the quasi-particle currents being balanced by the current of the condensate. The Andreev reflection represents a good example, where the quasi-particle current of $2e$ entering the superconductor decays and is converted to supercurrent.

Appendix B

Quasi-classical Green's function technique

Here we give a short, but self-contained derivation of the Eilenberger equation (3.2) and the corresponding quasi-classical current expression (3.6). We show how the renormalization procedure takes care of the cancellation of bulk diamagnetic and Fermi surface paramagnetic currents in the normal metal. Eq. (3.6) depends on the quasi-classical Green's function at the Fermi surface and its deviation from the normal state. The treatment given here follows the spirit of [Kopnin 1997].

B.1 Eilenberger equations

We define the 2×2 matrix Green's function in imaginary time [$x = (\mathbf{x}, \tau)$]

$$\hat{G}(x_1, x_2) = -\langle T_\tau \hat{\Psi}(x_1) \hat{\Psi}^\dagger(x_2) \rangle = \begin{pmatrix} G(x_1, x_2) & F(x_1, x_2) \\ F^\dagger(x_1, x_2) & -G(x_2, x_1) \end{pmatrix}, \quad (\text{B.1})$$

by the Nambu-space operator (A.2) in the Heisenberg picture with respect to the spin-symmetric Hamiltonian (A.1). \hat{G} fulfills the equation of motion

$$\hat{G}^{-1} * \hat{G}(x_1, x_2) = \delta(x_1 - x_2). \quad (\text{B.2})$$

where \hat{G}^{-1} is the matrix operator

$$\hat{G}^{-1}(x_1, x_2) = - \begin{pmatrix} \frac{\partial}{\partial \tau_1} + h_0 - \mu & \Delta(x_1) \\ \Delta^*(x_1) & \frac{\partial}{\partial \tau_1} - h_0^* + \mu \end{pmatrix} \delta(x_1 - x_2), \quad (\text{B.3})$$

$h_0 = -\frac{1}{2m}(\nabla_1 + ie\mathbf{A}(x_1))^2$, and the contraction is defined by $A * B(x_1, x_2) = \int dx' A(x_1, x') B(x', x_2)$. Similarly, the conjugate equation of motion takes the form

$$\hat{G} * \hat{G}^{-1}(x_1, x_2) = \delta(x_1 - x_2). \quad (\text{B.4})$$

In the following we assume homogeneity in time $\partial_{\tau_1} = -\partial_{\tau_2}$. We also want to neglect the \mathbf{A}^2 term in (B.3). While the Green's function \hat{G} varies on the Fermi wavelength $1/k_F$, the vector potential varies on a much larger scale, which we denote by ζ . With

$$(\nabla + ie\mathbf{A}(x))^2 = \nabla^2 + ie(\nabla \cdot \mathbf{A}(x)) + 2ie\mathbf{A}(x) \cdot \nabla - e^2\mathbf{A}(x)^2, \quad (\text{B.5})$$

and typically $\nabla \sim k_F$, we find that the term $e^2\mathbf{A}^2 \sim e^2H^2\zeta^2$ is negligible in comparison to $2e\mathbf{A} \cdot \nabla \sim eHk_F\zeta$ under the condition

$$\zeta \ll \frac{k_F c}{eH} \equiv r_L, \quad (\text{B.6})$$

where r_L denotes the Larmor radius, which is the cyclotron radius of an electron traveling at Fermi velocity v_F .

The quasi-classical approximation is best done in the Fourier representation

$$\tilde{G}(\mathbf{p}_1, \mathbf{p}_2; \tau) = \int d^3x_1 d^3x_2 G(\mathbf{x}_1, \mathbf{x}_2; \tau) e^{-i\mathbf{p}_1 \cdot \mathbf{x}_1 + i\mathbf{p}_2 \cdot \mathbf{x}_2}, \quad (\text{B.7})$$

where the equation of motion for the first Gorkov Green's function in (B.1) takes the form

$$\begin{aligned} \left(-\frac{\partial}{\partial \tau} - \frac{\mathbf{p}_1^2}{2m} + \mu \right) \tilde{G}(\mathbf{p}_1, \mathbf{p}_2; \tau) - \int d^3k' \Delta(\mathbf{k}') \tilde{F}^\dagger(\mathbf{p}_1 - \mathbf{k}', \mathbf{p}_2; \tau) \\ - \frac{e}{2m} \int d^3k' \mathbf{k}' \cdot \mathbf{A}(\mathbf{k}') \tilde{G}(\mathbf{p}_1 - \mathbf{k}', \mathbf{p}_2; \tau) \\ - \frac{e}{m} \int d^3k' \mathbf{A}(\mathbf{k}') \cdot (\mathbf{p}_1 - \mathbf{k}') \tilde{G}(\mathbf{p}_1 - \mathbf{k}', \mathbf{p}_2; \tau) = (2\pi)^3 \delta(\mathbf{p}_1 - \mathbf{p}_2) \delta(\tau). \end{aligned} \quad (\text{B.8})$$

Introducing the center-of-mass and relative coordinates

$$\mathbf{x} = \frac{1}{2}(\mathbf{x}_1 + \mathbf{x}_2), \quad \mathbf{r} = \mathbf{x}_1 - \mathbf{x}_2, \quad (\text{B.9})$$

and their conjugate momenta

$$\mathbf{k} = \mathbf{p}_1 - \mathbf{p}_2, \quad \mathbf{p} = \frac{1}{2}(\mathbf{p}_1 + \mathbf{p}_2), \quad (\text{B.10})$$

we find that \mathbf{r} varies on scale $1/k_F$, while \mathbf{x} varies on the much larger scale ζ . Eq. (B.8) translates to $[G(\mathbf{k}, \mathbf{p}; \tau) = \tilde{G}(\mathbf{p}_1, \mathbf{p}_2; \tau)]$

$$\begin{aligned} \left(-\frac{\partial}{\partial \tau} - \frac{(\mathbf{p} + \frac{\mathbf{k}}{2})^2}{2m} + \mu \right) G(\mathbf{k}, \mathbf{p}; \tau) - \int d^3k' \Delta(\mathbf{k}') F^\dagger(\mathbf{k} - \mathbf{k}', \mathbf{p} - \frac{\mathbf{k}'}{2}; \tau) \\ - \frac{e}{2m} \int d^3k' (2\mathbf{p} + \mathbf{k} - \mathbf{k}') \cdot \mathbf{A}(\mathbf{k}') G(\mathbf{k} - \mathbf{k}', \mathbf{p} - \frac{\mathbf{k}'}{2}; \tau) = (2\pi)^3 \delta(\mathbf{k}) \delta(\tau). \end{aligned} \quad (\text{B.11})$$

In the quasi-classical approximation, we retain only contributions for $k' \ll k_F$, assuming a smooth variation of Δ and \mathbf{A} on Fermi wavelength ($k_F \zeta \ll 1$), and obtain

$$\left(-\frac{\partial}{\partial \tau} - \frac{\mathbf{p}^2 + \mathbf{p} \cdot \mathbf{k}}{2m} + \mu \right) G(\mathbf{k}, \mathbf{p}; \tau) - \int d^3 k' \Delta(\mathbf{k}') F^\dagger(\mathbf{k} - \mathbf{k}', \mathbf{p}; \tau) \quad (\text{B.12})$$

$$- \frac{e}{m} \int d^3 k' \mathbf{p} \cdot \mathbf{A}(\mathbf{k}') G(\mathbf{k} - \mathbf{k}', \mathbf{p}; \tau) = (2\pi)^3 \delta(\mathbf{k}) \delta(\tau),$$

Transforming back to the real space center-of-mass coordinate and carrying out a Fourier expansion in time, we arrive at

$$\left(i\omega_n - \frac{\mathbf{p}^2 - i\mathbf{p} \cdot \nabla}{2m} + \mu - \frac{e}{m} \mathbf{p} \cdot \mathbf{A}(\mathbf{x}) \right) G(\mathbf{x}, \mathbf{p}; \omega_n) - \Delta(\mathbf{x}) F^\dagger(\mathbf{x}, \mathbf{p}; \omega_n) = 1. \quad (\text{B.13})$$

The fast oscillations of G on Fermi wavelength are described by the \mathbf{p}^2 term. The above procedure is carried out similarly for the Green's functions F and F^\dagger , obtaining the quasi-classical equation of motion for the matrix Green's function \hat{G} and its conjugate

$$\hat{G}^{-1}(\mathbf{x}, \mathbf{p}; \omega_n) \hat{G}(\mathbf{x}, \mathbf{p}; \omega_n) = 1, \quad (\text{B.14})$$

$$\hat{G}(\mathbf{x}, \mathbf{p}; \omega_n) \hat{G}^{-1}(\mathbf{x}, \mathbf{p}; \omega_n) = 1, \quad (\text{B.15})$$

where $(\xi_p = p^2/2m - \mu)$

$$\hat{G}^{-1}(\mathbf{x}, \mathbf{p}; \omega_n) = i\omega_n - \frac{e}{mc} \mathbf{p} \cdot \mathbf{A} + \left(-\xi_p + i \frac{\mathbf{p} \cdot \nabla}{2m} \right) \hat{\tau}_3 - \text{Re} \Delta \hat{\tau}_1 + \text{Im} \Delta \hat{\tau}_2, \quad (\text{B.16})$$

and the gradient ∇ is to be taken with a negative sign when acting to the left in (B.15). We have thus arrived at first-order differential equations with respect to the center-of-mass coordinate \mathbf{x} , the dependence of which accounts for the inhomogeneity of the slowly varying potential and field. The momentum dependence of \hat{G} lies at the Fermi surface $|\mathbf{p}| = k_F$.

We are now ready to define the quasi-classical Green's function by the integral over the momentum energy $= \xi_p$,

$$\hat{g}_{\omega_n}(\mathbf{x}, \mathbf{v}_F) = \frac{i}{\pi} \hat{\tau}_3 \int_{\gamma_0} d\xi_p \hat{G}(\mathbf{x}, \mathbf{p}; \omega_n), \quad (\text{B.17})$$

keeping the dependence on the momentum direction as denoted by the Fermi velocity \mathbf{v}_F . To provide a cutoff for the high energy contributions at E_C , we use the integration path γ_0 shown in Fig. B.1 ($T, \Delta \ll E_C \ll E_F$). From the subtraction of the equation of motion (B.14) and its conjugate (B.15), appropriately multiplied

with $\hat{\tau}_3$, we eliminate the ξ_p term in (B.16) and after integration over the momentum energy we find the Eilenberger equation

$$-(\mathbf{v}_F \cdot \nabla) \hat{g}_{\omega_n}(\mathbf{x}, \mathbf{v}_F) = \left[\{\omega_n + ie\mathbf{v}_F \cdot \mathbf{A}(\mathbf{x})\} \hat{\tau}_3 + \text{Re}\Delta(\mathbf{x}) \hat{\tau}_2 + \text{Im}\Delta(\mathbf{x}) \hat{\tau}_1, \hat{g}_{\omega_n}(\mathbf{x}, \mathbf{v}_F) \right]. \quad (\text{B.18})$$

The quasi-classical equations need to be complemented by a normalization condition, as the source term on the right hand side of (B.14) and (B.15) has been canceled by the subtraction. The normalization is provided by

$$\hat{g}^2 = 1, \quad (\text{B.19})$$

as follows from the homogeneous solution and the fact that \hat{g}^2 is a constant of motion of (B.19). The following symmetry relations for the quasi-classical Green's functions

$$g(\omega_n)^* = -g(-\omega_n), \quad f(\omega_n)^* = f^\dagger(-\omega_n), \quad (\text{B.20})$$

and

$$g(\mathbf{v}_F)^* = g(-\mathbf{v}_F), \quad f(\mathbf{v}_F)^* = f^\dagger(-\mathbf{v}_F), \quad (\text{B.21})$$

simplify the solution of (B.19). Eq. (B.20) follows from the definition (B.17) and Eq. (B.21) directly from the equation of motion (B.19). The quasi-classical Green's function takes the form

$$\hat{g} = \begin{pmatrix} g & f \\ f^\dagger & -g \end{pmatrix}. \quad (\text{B.22})$$

For convenience, we redefine the pair potential $\Delta \rightarrow i\Delta$ and obtain the form of the equations used in this thesis, see (3.2),

$$-(\mathbf{v}_F \cdot \nabla) \hat{g} = \left[\{\omega_n + ie\mathbf{v}_F \cdot \mathbf{A}(\mathbf{x})\} \hat{\tau}_3 + \text{Re}\Delta(\mathbf{x}) \hat{\tau}_1 - \text{Im}\Delta(\mathbf{x}) \hat{\tau}_2, \hat{g} \right]. \quad (\text{B.23})$$

B.2 Quasi-classical current expression

The current density in terms of the usual Green's function (with respect to center-of-mass and relative momentum) is given by

$$\mathbf{j}(\mathbf{k}) = -\frac{2e}{m} \int \frac{d^3p}{(2\pi)^3} \mathbf{p} G(\mathbf{k}, \mathbf{p}; 0-) - \frac{ne^2}{m} \mathbf{A}(\mathbf{k}). \quad (\text{B.24})$$

The first term in (B.24) gives the paramagnetic current which is induced by the perturbation of the Green's function G in the presence of an applied field and lives at the Fermi surface. The second term in (B.24) gives the diamagnetic current giving

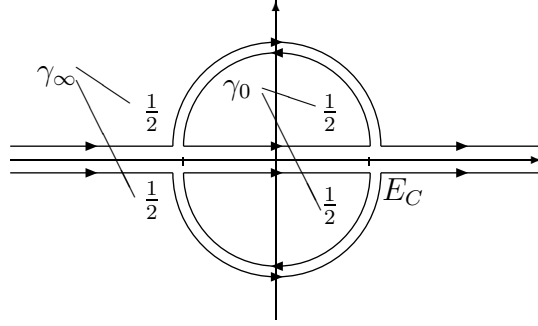


Figure B.1: Integration paths: γ_0 denotes the two inner half circles, γ_∞ the two outer high energy contributions. Together γ_0 and γ_∞ reduce to the integration over the real line.

the rigid response of the bulk density n to the vector potential. In the normal state $G = G^{(n)}$, the paramagnetic current is known to cancel the diamagnetic current up to small correction of the order of Landau diamagnetism, see e.g. [Tinkham 1996]. Using this fact, we easily find that the current

$$\mathbf{j}(\mathbf{k}) = -\frac{e}{m} \int_{-\infty}^{+\infty} d\xi_p N(\xi_p) \int \frac{d\Omega_p}{4\pi} \mathbf{p} (G(\mathbf{k}, \mathbf{p}; 0-) - G^{(n)}(\mathbf{k}, \mathbf{p}; 0-)), \quad (\text{B.25})$$

can be expressed by the deviation of the Green's function from the normal state value ($N(\xi_p)$ is the density of states). Splitting the integration of the momentum energy ξ_p along the paths γ_0 and γ_∞ , we obtain

$$\mathbf{j}(\mathbf{k}) = -eN_0 \int \frac{d\Omega_p}{4\pi} \frac{\mathbf{p}_F}{m} \int_{\gamma_0} d\xi_p (G(\mathbf{k}, \mathbf{p}; 0-) - G^{(n)}(\mathbf{k}, \mathbf{p}; 0-)) \quad (\text{B.26})$$

$$-\frac{e}{m} \int_{\gamma_\infty} d\xi_p N(\xi_p) \int \frac{d\Omega_p}{4\pi} \mathbf{p} (G - G^{(n)}). \quad (\text{B.27})$$

The high energy contribution in (B.27) vanishes as the Green's function G only deviates from $G^{(n)}$ at energies of the order $\xi_p \sim T, \Delta \ll E_C$. Inserting the Fourier expansion in time into the first we find

$$\mathbf{j}(\mathbf{k}) = -eN_0 \int \frac{d\Omega_p}{4\pi} \frac{\mathbf{p}_F}{m} \int_{\gamma_0} d\xi_p T \sum_{\omega_n} (G(\mathbf{k}, \mathbf{p}; \omega_n) - G^{(n)}(\mathbf{k}, \mathbf{p}; \omega_n)). \quad (\text{B.28})$$

Having introduced the high-energy cutoff by γ_0 we can exchange the Matsubara sum and the energy integration, which otherwise would have lead to a divergence, see [Abrikosov 1975]. Using the definition of the quasi-classical Green's functions (B.17), the current takes the form

$$\mathbf{j}(\mathbf{x}) = ieN_0\pi T \sum_{\omega_n} \int \frac{d\Omega_p}{4\pi} \mathbf{v}_F (g_{\omega_n}(\mathbf{x}, \mathbf{v}_F) - g_{\omega_n}^{(n)}(\mathbf{x}, \mathbf{v}_F)). \quad (\text{B.29})$$

The quasi-classical Green's function for the normal state $g = \text{sgn}(\omega_n)$ that is found from $G(\mathbf{p}) = 1/(i\omega_n - \xi_p)$ conveniently drops out of Eq. (B.29) and we obtain the quasi-classical current expression (3.6).

Appendix C

Response kernel

Starting from Eqs. (3.19) and (3.20) we derive the linear response kernel $K(x, x')$. The transformation of g , f , and f^\dagger introduced in [Schopohl 1995, Schopohl 1998],

$$a(x, v_x) = \frac{f(x, v_x)}{1 + g(x, v_x)}, \quad a^\dagger(x, v_x) = \frac{f^\dagger(x, v_x)}{1 + g(x, v_x)}, \quad (\text{C.1})$$

decouples the full equations of motions (3.2) to two Riccati differential equations. For the zeroth order equations we obtain

$$\begin{aligned} -v_x \partial_x a_0(x, v_x) &= 2\tilde{\omega}(x) a_0(x, v_x) + \tilde{\Delta}(x) (a_0^2(x, v_x) - 1) \\ v_x \partial_x a_0^\dagger(x, v_x) &= 2\tilde{\omega}(x) a_0^\dagger(x, v_x) + \tilde{\Delta}(x) (a_0^{\dagger 2}(x, v_x) - 1). \end{aligned} \quad (\text{C.2})$$

After linearization of (C.1) we obtain

$$f_1(x, v_x, v_y) = 2 \frac{a_1(x, v_x, v_y) - a_0^2(x, v_x) a_1^\dagger(x, v_x, v_y)}{(1 + a_0(x, v_x) a_0^\dagger(x, v_x))^2} \quad (\text{C.3})$$

$$f_1^\dagger(x, v_x, v_y) = 2 \frac{a_1^\dagger(x, v_x, v_y) - a_0^{\dagger 2}(x, v_x) a_1(x, v_x, v_y)}{(1 + a_0(x, v_x) a_0^\dagger(x, v_x))^2}, \quad (\text{C.4})$$

and Eqs. (3.19) and (3.20) are decoupled to

$$-\frac{v_x}{2} \partial_x a_1(x, v_x, v_y) = \left[\tilde{\omega}(x) + \tilde{\Delta}(x) a_0(x, v_x) \right] a_1(x, v_x, v_y) + e v_y A_y(x) a_0(x, v_x) \quad (\text{C.5})$$

$$\begin{aligned} \frac{v_x}{2} \partial_x a_1^\dagger(x, v_x, v_y) &= \left[\tilde{\omega}(x) + \tilde{\Delta}(x) a_0^\dagger(x, v_x) \right] a_1^\dagger(x, v_x, v_y) \\ &+ e v_y A_y(x) a_0^\dagger(x, v_x). \end{aligned} \quad (\text{C.6})$$

As a consequence of Eq. (C.5) we find $a_1(-v_y) = -a_1(v_y)$ and the same for a_1^\dagger , implying $\langle f_1 \rangle = \langle f_1^\dagger \rangle = 0$. Furthermore, since $a_1^\dagger(v_x) = a_1(-v_x)$, we only have

to consider one of the two equations (e.g. the first one). Equation (C.5) is an inhomogeneous first-order differential equation, which can be integrated analytically. Assuming that f and f^\dagger do not change sign as a function of x , with the help of (3.18) the solution can be written as

$$a_1(x, v_x, v_y) = c(v_x, v_y) \frac{m(v_x, x, x_0)}{f_0^\dagger(x, v_x)} - \frac{2ev_y}{v_x f_0^\dagger(x, v_x)} \int_{x_0}^x [1 - g_0(x', v_x)] m(v_x, x, x') A_y(x') dx' \quad (\text{C.7})$$

where

$$m(v_x, x, x') = \exp \left(\frac{2}{v_x} \int_x^{x'} \frac{\tilde{\Delta}(x'')}{f_0^\dagger(x'', v_x)} dx'' \right) \quad (\text{C.8})$$

In this equation x_0 is an arbitrary reference point and the constant c has to be determined by the appropriate boundary conditions. m satisfies the relations of a propagator, $m(v_x, x, x') = m(u, x', x)^{-1}$ and $m(v_x, x, x'')m(u, x'', x') = m(v_x, x, x')$. Now we determine the constant c for a system of size $[-d_s, d]$. We assume specular reflection at two boundaries at $x = -d_s, d$ and ideal interfaces between different materials inside the system. The appropriate boundary conditions are the continuity of the Green's function along the classical trajectories, i.e., $\hat{g}(x, v_x, v_y) = \hat{g}(x, -v_x, v_y)$ at $x = -d_s, d$ for the specular reflection and $\hat{g}(x = 0-, v_x, v_y) = \hat{g}(x = 0+, -v_x, v_y)$ at the NS interface. The same conditions are valid for a_1 and a_1^\dagger . We thus obtain

$$c(v_x, v_y) = 2e \frac{v_y}{v_x} \int_{-d_s}^d \frac{m(v_x, d, x') + m(-v_x, d, x')}{m(v_x, d, -d_s) - m(-v_x, d, -d_s)} \times [1 - g_0(x', v_x)] A(x') dx' . \quad (\text{C.9})$$

The current is determined by Eq. (3.6), expressed by the solution (C.7). We obtain the following general result for the linear current functional,

$$j_y(x) = - \int_{-d_s}^d K(x, x') A(x') dx' , \quad (\text{C.10})$$

where the kernel $K(x, x')$ is given by

$$K(x, x') = e^2 v_F N_0 \pi T \sum_{\omega_n > 0} \int_0^{v_F} du \frac{v_F^2 - u^2}{v_F^2 u} [1 + g_0(x, u)] [1 - g_0(x', u)] \left[\Theta(x - x') m(u, x, x') + \Theta(x' - x) m(-u, x, x') \right]$$

$$\begin{aligned}
& + \frac{m(-u, x, d)m(u, d, x')}{1 - m(u, d, -d_s)m(-u, -d_s, d)} \\
& + \frac{m(u, x, -d_s)m(-u, -d_s, x')}{1 - m(u, d, -d_s)m(-u, -d_s, d)} \\
& + \frac{m(-u, x, d)m(u, d, -d_s)m(-u, -d_s, x')}{1 - m(u, d, -d_s)m(-u, -d_s, d)} \\
& + \frac{m(u, x, -d_s)m(-u, -d_s, d)m(u, d, x')}{1 - m(u, d, -d_s)m(-u, -d_s, d)} \Big].
\end{aligned} \tag{C.11}$$

Equation (C.11) gives the exact linear-response kernel of any quasi-one-dimensional system, consisting of a combination of normal and superconducting layers extending from $x = -d_s$ to $x = d$. The kernel is expressed in terms of the quasi-classical Green's functions in absence of the fields, which may be specified for the particular problem of interest. We note two characteristic features of Eq. (C.11): The factor $1 - g_0$ measures the deviation from the normal state Green's function $g_0 \equiv 1$, which produces no screening current. The propagator $m(u, x, x')$ shows up in six summands which represent all the ballistic paths from x to x' , accounting for multiple reflection at the walls at $-d_s$ and d . Thus the first two summands connecting x and x' directly constitute the bulk contribution, while the additional four summands are specific to a finite system (assuming specular reflection at the boundary). We note that a form similar to (C.11) may be derived for non-ideal interfaces between the normal and superconducting layers, if the appropriate boundary conditions following [Zaitsev 1984] are taken into account.

For the NS system considered in Chapter 3, the linear response kernel (C.11) may be simplified using $m(u, x, -\infty) \rightarrow 0$ and $m(-u, -\infty, x) \rightarrow 0$ as $d_s \rightarrow \infty$ ($u > 0$), obtaining

$$\begin{aligned}
K(x, x') &= e^2 v_F N_0 \pi T \sum_{\omega_n > 0} \int_0^{v_F} du \frac{v_F^2 - u^2}{v_F^2 u} [1 + g_0(x, u)] [1 - g_0(x', u)] \\
& \left[\Theta(x - x') m(u, x, x') + \Theta(x' - x) m(-u, x, x') \right. \\
& \left. + m(-u, x, d) m(u, d, x') \right].
\end{aligned}$$

Bibliography

- [Abrikosov 1975] A. A. Abrikosov, L. P. Gorkov, and I. E. Dzyaloshinski, *Methods of Quantum Field Theory in Statistical Physics* (Dover, New York 1975).
- [Aleiner 1996] I. L. Aleiner, P. Clarke, and L. I. Glazman, Phys. Rev. B **53**, R7630 (1996).
- [Altland 1996] A. Altland, Y. Gefen, G. Montambaux, Phys. Rev. Lett. **76**, 1130 (1996).
- [Ambegaokar 1982] V. Ambegaokar, U. Eckern, and G. Schön, Phys. Rev. Lett. **48**, 1745 (1982).
- [Anantram 1996] M. P. Anantram and S. Datta, Phys. Rev. B **53**, 16 390 (1996).
- [Andreev 1964] A. F. Andreev, Zh. Eksp. Teor. Fiz. **46**, 1823 (1964) [Sov. Phys. JETP **19**, 1228 (1964)].
- [Andreev 1965] A. F. Andreev, Zh. Eksp. Teor. Fiz. **22**, 655 (1965) [Sov. Phys. JETP **22**, 455 (1966)].
- [Antsygina 1975] T.N. Antsygina, E.N. Bratus, and A.V. Svidzinskii, Sov. J. Low Temp. Phys. **1**, 23 (1975).
- [Argaman 1997] N. Argaman, Europhys. Lett. **38**, 231 (1997).
- [Averin 1995] D. Averin and A. Bardas, Phys. Rev. Lett. **75**, 1831 (1995).
- [Averin 1996] D. Averin and H. T. Imam, Phys. Rev. Lett. **76**, 3814 (1996).
- [Averin 1998] D. V. Averin, Solid State Commun. **105**, 659 (1998).
- [Bakker 1994] S. J. M. Bakker, E. van der Drift, T. M. Klapwijk, H. M. Jaegger, and S. Radelaar, Phys. Rev. B **49**, 13275 (1994).

- [Barzykin 1998] V. Barzykin and A. M. Zagoskin, cond-mat/9805104 (1998).
- [Baselmans 1999] J. J. A. Baselmans, A. F. Morpurgo, B. J. van Wees, and T. M. Klapwijk, *Nature* **397**, 43 (1999)
- [Beenakker 1991] C. W. J. Beenakker and H. van Houten, *Phys. Rev. Lett.* **66**, 3056 (1991).
- [Beenakker 1992a] C. W. Beenakker, *Phys. Rev. B* **46**, 12841 (1992).
- [Beenakker 1992b] C. W. J. Beenakker and M. Büttiker, *Phys. Rev. B* **46**, 1889 (1992).
- [Belzig 1995] W. Belzig, Diploma thesis, Universität Karlsruhe (1995).
- [Belzig 1996a] W. Belzig, C. Bruder, and G. Schön, *Phys. Rev. B* **53**, 5727 (1996).
- [Belzig 1996b] W. Belzig, C. Bruder, and G. Schön, *Phys. Rev. B* **54**, 9443 (1996).
- [Belzig 1998] W. Belzig, C. Bruder, and A. L. Fauchère, *Phys. Rev. B* **58**, 14531 (1998).
- [Belzig 1999] W. Belzig, Ph.D. thesis, Universität Karlsruhe (1999).
- [Bergmann 1987] Th. Bergmann, K. H. Kuhl, B. Schröder, M. Jutzler, and F. Pobell, *J. Low Temp. Phys.* **66**, 209 (1987).
- [Blatter 1988] G. Blatter and D. Browne, *Phys. Rev. B* **37**, 3856 (1988).
- [Blatter 1994] G. Blatter, M. V. Feigel'man, V. B. Geshkenbein, A. I. Larkin, V. M. Vinokur, *Rev. Mod. Phys.* **66**, 1125 (1994).
- [Blonder 1982] G. E. Blonder, M. Tinkham, and T. M Klapwijk, *Phys. Rev. B* **25**, 4515 (1982).
- [Bocko 1997] M. F. Bocko, A. M. Herr, and M. J. Feldman, *IEEE Trans. Appl. Supercond.* **7**, 3638 (1997).
- [Brouwer 1995] P. W. Brouwer, C. W. J. Beenakker, *Phys. Rev. B* **52**, R3868 (1995).
- [Bruder 1998] C. Bruder and Y. Imry, *Phys. Rev. Lett.* **80**, 5782 (1998).
- [Burkard 1999] G. Burkard, D. Loss, and D. P. DiVincenzo, *Phys. Rev. B* **59**, 2070 (1999).

- [Büttiker 1985] M. Büttiker, Y. Imry, R. Landauer, Phys. Lett. **96A**, 365 (1983).
- [Büttiker 1985] M. Büttiker, Y. Imry, R. Landauer, and S. Pinhas, Phys. Rev. B **31**, 6207 (1985).
- [Büttiker 1992] M. Büttiker, Phys. Rev. B **46**, 12485 (1992).
- [Caldeira 1983] A. O. Caldeira, A. J. Leggett, Ann. Phys. **149**, 374 (1983).
- [Charlat 1996] P. Charlat, H. Courtois, Ph. Gandit, D. Mailly, A. F. Volkov, and B. Pannetier, Phys. Rev. Lett. **77**, 4950 (1996).
- [Chaudhuri 1995] S. Chaudhuri and P. F. Bagwell, Phys. Rev. B **51**, 16936 (1995).
- [Chen 1991] L.Y. Chen and C.S. Ting, Phys. Rev. B **43**, 4534 (1991).
- [Christen 1996] T. Christen, M. Büttiker, Europhys. Lett. **35**, 523 (1996).
- [Cirac 1995] J. I. Cirac, P. Zoller, Phys. Rev. Lett. **74**, 4091 (1995).
- [Claughton 1996] N. R. Claughton, R. Raimondi, C. J. Lambert, Phys. Rev. B **53**, 9310 (1996).
- [Courtois 1996] H. Courtois, Ph. Gandit, D. Mailly, and B. Pannetier, Phys. Rev. Lett. **76**, 130 (1996).
- [Covington 1997] M. Covington, M. Aprili, E. Paraoanu, L. H. Greene, F. Xu, J. Zhu, and C. A. Mirkin, Phys. Rev. Lett. **79**, 277 (1997).
- [Dieleman 1997] P. Dieleman, H. G. Bukkems, T. M. Klapwijk, M. Shicke, and K. H. Gundlach, Phys. Rev. Lett. **79**, 3486 (1997).
- [Dorokhov 1982] O. N. Dorokhov, JETP Lett. **36**, 318 (1982).
- [Edwards 1972] J. T. Edwards and D. J. Thouless, J. Phys. C **5**, 807 (1972).
- [Eilenberger 1968] G. Eilenberger, Z. Phys. **214**, 195 (1968).
- [Ekert 1996] A. Ekert and R. Jozsa, Rev. Mod. Phys. **68**, 733 (1996).
- [Eschrig 1997] M. Eschrig, Ph.D. thesis, Universität Bayreuth (1997).
- [Falk 1963] D. S. Falk, Phys. Rev. **132**, 1576 (1963).

- [Fauchère 1997] A. L. Fauchère and G. Blatter, Phys. Rev. B **56**, 14102 (1997).
- [Fauchère 1998] A. L. Fauchère, G. B. Lesovik, and G. Blatter, Phys. Rev. B **58**, 11177 (1998).
- [Fauchère 1999a] A. L. Fauchère, V. Geshkenbein, and G. Blatter, Phys. Rev. Lett. **82**, 1796 (1999).
- [Fauchère 1999b] A. L. Fauchère, W. Belzig, and G. Blatter, Phys. Rev. Lett. **82**, 3336 (1999).
- [Feynman 1996] R. P. Feynman, in *Feynman Lectures on Computation* (Perseus, 1996).
- [Fogelström 1997] M. Fogelström, D. Rainer, and J. A. Sauls, Phys. Rev. Lett. **79**, 281 (1997).
- [Frahm 1996] K. M. Frahm, P. W. Brouwer, J. A. Melsen, and C. W. L. Beenakker, Phys. Rev. Lett. **76**, 2981 (1996).
- [Frassanito 1996] R. Frassanito, *Paramagnetic effect in NS proximity structures*, Ph.D. thesis, ETH Zürich, 1996.
- [de Gennes 1963] P. G. De Gennes and D. Saint-James, Phys. Lett. **4**, 151 (1963).
- [de Gennes 1964] P. G. de Gennes, Rev. Mod. Phys. **36**, 225 (1964).
- [de Gennes 1966a] P. G. de Gennes, *Superconductivity of Metals and Alloys* (Benjamin, New York, 1966).
- [de Gennes 1966b] Orsay Group on Superconductivity, in *Quantum Fluids*, ed. D. Brewer (North-Holland, Amsterdam, 1966).
- [Gershenfeld 1997] N. A. Gershenfeld and I. L. Chuang, Science **275**, 350 (1997).
- [Geshkenbein 1988] V. B. Geshkenbein and A. V. Sokol, Zh. Eksp. Teor. Fiz. **94**, 259 (1988) [Sov. Phys. JETP **67**, 362 (1988)].
- [Geshkenbein 1998] V. B. Geshkenbein, L. B. Ioffe, and A. J. Millis, Phys. Rev. Lett. **80**, 5778 (1998).
- [Giroud 1998] M. Giroud, H. Courtois, K. Hasselbach, D. Mailly, and B. Pannetier, cond-mat/9806161.

- [Glattli 1997] L. Saminadayar, D. C. Glattli, Y. Jin, and B. Etienne, *Phys. Rev. Lett.* **79**, 2526 (1997).
- [Golubov 1997] A. A. Golubov, F. K. Wilhelm, and A. D. Zaikin, *Phys. Rev. B* **55**, 1123 (1997).
- [Golubov 1988] A. A. Golubov and M. Yu. Kuprianov, *J. Low Temp. Phys.* **70**, 83 (1988).
- [Gorelik 1998] L. Y. Gorelik, N. I. Lundin, V. S. Shumeiko, R. I. Shekhter, and M. Jonson, *Phys. Rev. Lett.* **81**, 2538 (1998).
- [Guéron 1996] S. Guéron, H. Pothier, N. O. Birge, D. Esteve, and M. Devoret, *Phys. Rev. Lett.* **77**, 3025 (1996).
- [Hara 1993] J. Hara, M. Ashida, and K. Nagai, *Phys. Rev. B* **47**, 11263 (1993).
- [Haroche 1996] S. Haroche and J.-M. Raimond, *Physics Today* **49-8**, 51 (1996).
- [Hartog 1997] S. G. Hartog, B. J. van Wees, T. M. Klapwijk, Yu. V. Nazarov, and G. Borghs, *Phys. Rev. B* **56**, 13738 (1997).
- [Heida 1998] J. P. Heida, B. J. van Wees, T. M. Klapwijk, and G. Borghs, *Phys. Rev. B* **57**, R5618 (1998).
- [Hekking 1994] F. W. J. Hekking and Yu. V. Nazarov, *Phys. Rev. B* **49**, 6847 (1994).
- [Herath 1989] J. Herath and D. Rainer, *Physica C* **161**, 209 (1989).
- [Hessling 1996] J. P. Hessling, V. S. Shumeiko, Yu. M. Galperin, and G. Wendin, *Europhys. Lett.* **34**, 49 (1996).
- [Higashitani 1995] S. Higashitani and K. Nagai, *J. Phys. Soc. Jpn.* **64**, 549 (1995).
- [Honerkamp 1998] C. Honerkamp and M. Sigrist, *J. Low Temp. Phys.* **111**, 895 (1998).
- [Hoyt 1976a] R. F. Hoyt and A. C. Mota, *Solid State Comm.* **18**, 139 (1976).
- [Hoyt 1976b] R. F. Hoyt, A. C. Mota, and C. A. Luengo, *Phys. Rev. B* **14**, 441 (1976).

- [Il'ichev 1998] E. Il'ichev, V. Zakosarenko, R. P. J. IJsselsteijn, H. E. Hoenig, V. Schultze, H.-G. Meyer, M. Grajcar, R. Hlubina, cond-mat/9811017.
- [Ioffe 1998] L. B. Ioffe, V. B. Geshkenbein, M. V. Feigel'man, A. L. Fauchère, and G. Blatter, *Nature* **398**, 679 (1999).
- [Ishii 1970] C. Ishii, *Progr. Theor. Phys.* **44**, 1525 (1970).
- [Jehl 1999] X. Jehl, C. Baraduc, M. Sanquer, *Recontres de Moriond* (1999).
- [Johnson 1927] M. B. Johnson, *Phys. Rev.* **29**, 367 (1927).
- [de Jong 1994] M. J. M. de Jong and C. W. J. Beenakker, *Phys. Rev. B* **49**, 16 070 (1994).
- [de Jong 1997] M. J. M. de Jong and C. W. J. Beenakker, in [Kouwenhoven 1997].
- [Josephson 1962] B. D. Josephson, *Phys. Lett.* **1**, 251 (1962).
- [Joyez 1994] P. Joyez, P. Lafarge, A. Filipe, D. Esteve, and M. H. Devoret, *Phys. Rev. Lett.* **72**, 2458 (1994).
- [Kastalsky 1991] A. Kastalsky, A. W. Kleinsasser, L. H. Greene, R. Bhat, F. P. Milliken, and J. P. Harbison, *Phys. Rev. Lett.* **67**, 3026 (1991).
- [Khlus 1987] V. A. Khlus, *Zh. Eksp. Teor. Fiz.* **93**, 2179 (1987) [*Sov. Phys. JETP* **66**, 1243 (1987)].
- [Kieselmann 1987] G. Kieselmann, *Phys. Rev. B* **35**, 6762 (1987).
- [Kirtley 1995] J.R. Kirtley *et al.*, *Nature* **373**, 225 (1995).
- [Kopnin 1997] N. Kopnin, *Introduction to the microscopic theory of superconductivity, stationary superconductivity*, Lecture Notes (1997).
- [Kogan 1996] V. G. Kogan, A. Gurevich, J. H. Cho, D. C. Johnston, M. Xu, J. R. Thompson, and A. Martynovich, *Phys. Rev. B* **54**, 12386 (1996).

- [Kouwenhoven 1997] *Mesoscopic Electron Transport*, eds. L. P. Kouwenhoven, L. Sohn, and G. Schön, NATO ASI Series E **345**, Kluwer Academic (1997).
- [Kozhevnikov 1999] A. Kozhevnikov, R. Schoelkopf, D. Prober, *Recontres de Moriond* (1999).
- [Kulik 1970] I. O. Kulik, *Zh. Eksp. Teor. Fiz.* **57**, 1745 (1969) [*Sov. Phys. JETP* **30**, 944 (1970)].
- [Lambert 1991] C. J. Lambert, *J. Phys. Cond. Mat.* **3**, 6579 (1991).
- [Lambert 1998] C. J. Lambert, R. Raimondi, *J. Phys. Cond. Mat.* **10**, 901 (1998).
- [Landauer 1970] R. Landauer, *Philos. Mag.* **21**, 863 (1970).
- [Larkin 1968] A. I. Larkin and Yu. N. Ovchinnikov, *Zh. Eksp. Teor. Fiz.* **55** 2262 (1968) (*Sov. Phys. JETP* **26**, 1200 (1968)).
- [Leadbeater 1996] M. Leadbeater and C. J. Lambert, *J. Phys. Cond. Mat.* **8**, L345 (1996).
- [Ledermann 1998] U. Ledermann, Diploma thesis, ETH Zürich (1998).
- [Ledermann 1999] U. Ledermann, A. L. Fauchère, and G. Blatter, *Phys. Rev. B* **59**, R9027 (1999).
- [Lehnert 1999] K. W. Lehnert, N. Argaman, H.-R. Blank, K. C. Wong, S. J. Allen, E. L. Hu, H. Kroemer, *Phys. Rev. Lett.* **82**, 1265 (1999).
- [Lesovik 1989] G. B. Lesovik, *JETP Lett.* **49**, 592 (1989).
- [Lesovik 1994] G. B. Lesovik and L. S. Levitov, *Phys. Rev. Lett.* **72**, 724 (1994).
- [Lesovik 1997] G. B. Lesovik, A. L. Fauchère, and G. Blatter, *Phys. Rev. B* **55**, 3146 (1997).
- [Lesovik 1998] G. B. Lesovik and G. Blatter, *JETP Lett.* **68**, 599 (1998).
- [Levitov 1996] L. S. Levitov, H. Lee, and G. B. Lesovik, *J. Math. Phys.* **37**, 4845 (1996).
- [Likharev 1979] K.K. Likharev, *Rev. Mod. Phys.* **51**, 101 (1979).

- [Likharev 1991] K. K. Likharev and V. K. Semenov, IEEE Trans. on Appl. Supercond. **1**, 3 (1991).
- [London 1938] F. and H. London, Proc. Phys. Soc., **A149**, 71 (1938).
- [Loss 1998] D. Loss and D. P. DiVincenzo, Phys. Rev. A **57**, 120 (1998).
- [Magnée 1994] P. H. C. Magnée, N. van der Post, P. H. M. Kooistra, B. J. van Wees, and T. M. Klapwijk, Phys. Rev. B **50**, 4594 (1994).
- [Mahan 1990] G. D. Mahan, *Many particle physics* (Plenum Press, New York, 1990).
- [Marmokos 1993] I. K. Marmokos, C. W. Beenakker, and R. A. Jalabert, Phys. Rev. B, **48**, 2811 (1993).
- [Martin 1996] T. Martin, Phys. Lett. A **220**, 137 (1996).
- [McMillan 1968a] W. L. McMillan, Phys. Rev. **167**, 331 (1968).
- [McMillan 1968b] W. L. McMillan, Phys. Rev. **175**, 559 (1968).
- [Melsen 1994] J. A. Melsen, C. W. J. Beenakker, Phys. B **203**, 219 (1994).
- [Meissner 1933] W. Meissner and R. Ochsenfeld, Naturwissenschaften **21**, 787 (1933).
- [Monroe 1995] C. Monroe, D. Meekhof, B. King, W. Itano, and D. Wineland, Phys. Rev. Lett. **75**, 4714 (1995).
- [Morais Smith 1994] C. Morais Smith, B. Ivlev, and G. Blatter, Phys. Rev. B **49**, 4033 (1994).
- [Mota 1982] A. C. Mota, D. Marek, and J. C. Weber, Helv. Phys. Acta **55**, 647 (1982).
- [Mota 1989] A. C. Mota, P. Visani, and A. Pollini, J. Low Temp. Phys. **76**, 465 (1989).
- [Mota 1994] A. C. Mota, P. Visani, A. Pollini, and K. Aupke, Physica B **197**, 95 (1994).
- [Mota 1997] A. C. Mota, R. Frassanito, P. Visani, M. Nideröst, K. Swieca, and F. Pobell, in *Nanowires*, NATO ASI Series, Vol 340, 387-397 (1997).

- [Müller-Allinger 1999] F. B. Müller-Allinger, A. C. Mota, and W. Belzig, *Phys. Rev. B* **59**, 8887 (1999).
- [Muzykantskii 1994] B. A. Muzykantskii and D. E. Khmel'nitskii, *Phys. Rev. B* **50**, 3982 (1994).
- [Nagai 1988] K. Nagai and J. Hara, *J. Low Temp. Phys.* **71**, 351 (1988).
- [Narikiyo 1989] O. Narikiyo and H. Fukuyama, *J. Phys. Soc. Jpn.* **58**, 4557 (1989).
- [Nazarov 1996] Yu. V. Nazarov and T. H. Stoof, *Phys. Rev. Lett.* **76**, 823 (1996).
- [Nguyen 1992] C. Nguyen, H. Kroemer, and E. L. Hu, *Phys. Rev. Lett.* **69**, 2847 (1992).
- [Niño 1984] V. Niño C. and R. Kümmel, *Phys. Rev. B* **29**, 3957 (1984).
- [Nitta 1994] J. Nitta, T. Akazaki, and H. Takayanagi, *Phys. Rev. B* **49**, 3659 (1994).
- [Nyquist 1928] H. Nyquist, *Phys. Rev.* **32**, 110 (1928).
- [Octavio 1983] M. Octavio, M. Tinkham, G. E. Blonder, and T. M. Klapwijk, *Phys. Rev. B* **27**, 6739 (1983).
- [Oda 1980] Y. Oda and H. Nagano, *Solid State Commun.* **35**, 631 (1980).
- [Onoe 1995] H. Onoe, A. Sumuiyama, M. Nakagawa, and Y. Oda, *J. Phys. Soc. Jpn.* **64**, 2138 (1995).
- [Owen 1967] C. S. Owen and D. J. Scalapino, *Phys. Rev. B* **164**, 538 (1967).
- [Petrashov 1995] V. T. Petrashov, V. N. Antonov, P. Delsing, and T. Claeson, *Phys. Rev. Lett.* **74**, 5268 (1995).
- [de-Picciotto 1997] R. de-Picciotto, M. Reznikov, M. Heiblum, V. Umansky, G. Bunin, and D. Mahalu, *Nature* **389**, 162 (1997).
- [Pippard 1953] A. B. Pippard, *Proc. Roy. Soc.* **216**, 547 (1953).
- [Pothier 1994] H. Pothier, S. Guéron, D. Estève, and M. H. Devoret, *Phys. Rev. Lett.* **73**, 2488 (1994).

- [Poirier 1997a] W. Poirier, D. Mailly, and M. Sanquer, Phys. Rev. Lett. **79**, 2105 (1997).
- [Poirier 1997b] W. Poirier, Dissertation, University of Paris (1997).
- [Rammer 1986] J. Rammer and H. Smith, Rev. Mod. Phys. **58**, 323 (1986).
- [Rickayzen 1980] G. Rickayzen, *Green's functions in condensed matter* (Academic Press, London, 1980).
- [Rowell 1966] J. M. Rowell and W. L. McMillan, Phys. Rev. Lett. **16**, 453 (1966).
- [Saint-James 1964] D. Saint-James, J. Physique **25**, 899 (1964).
- [Scheer 1998] E. Scheer, N. Agraït, J. C. Cuevas, A. Levy Yeyati, B. Ludoph, A. Martin-Roderos, G. R. Bollinger, J. M. van Ruitenbeek, and C. Urbina, Nature **394**, 154 (1998).
- [Schön 1990] G. Schön and A. D. Zaikin, Phys. Rep. **198**, 237 (1990).
- [Schopohl 1995] N. Schopohl and K. Maki, Phys. Rev. B **52**, 490 (1995).
- [Schopohl 1998] N. Schopohl, cond-mat/9804064.
- [Schottky 1918] W. Schottky, Ann. Phys. **57**, 541 (1918).
- [Schrieffer 1988] J. R. Schrieffer, *Theory of Superconductivity*, Addison-Wesley (1988).
- [Serene 1983] J. W. Serene and D. Rainer, Physics Reports **4**, 221 (1983).
- [Shelankov 1985] A. L. Shelankov, J. Low Temp. Phys. **60**, 29 (1985).
- [Shnirman 1997] A. Shnirman, G. Schön, and Z. Hermon, Phys. Rev. Lett. **79**, 2371 (1997).
- [Shnirman 1998] A. Shnirman and G. Schön, Phys. Rev. B **57**, 15400 (1998).
- [Shumeiko 1997] V. S. Shumeiko, E. N. Bratus, and G. Wendin, Low Temp. Phys. **23**, 181 (1997).
- [Sigrist 1995] M. Sigrist and T. M. Rice, Rev. Mod. Phys. **67**, 503 (1995).
- [Stoof 1996] T. H. Stoof and Yu. V. Nazarov, Phys. Rev. B **53**, 14496 (1996).

- [Takayanagi 1995a] H. Takayanagi, Y. B. Hansen, and J. Nitta, Phys. Rev. Lett. **74**, 166 (1995).
- [Takayanagi 1995b] H. Takayanagi, T. Akazaki, and J. Nitta, Phys. Rev. Lett. **75**, 3533 (1995).
- [Takane 1991] Y. Takane and H. Ebisawa, J. Phys. Soc. Jap. **61**, 1685 (1991).
- [Takane 1992] Y. Takane and H. Ebisawa, J. Phys. Soc. Jap. **61**, 2858 (1992).
- [Tinkham 1996] M. Tinkham, *Introduction to Superconductivity*, 2nd edition (McGraw-Hill, Singapore, 1996).
- [Turchette 1995] Q. Turchette, C. Hood, W. Lange, H. Mabushi, and H. J. Kimble, Phys. Rev. Lett. **75**, 4710 (1995).
- [Usadel 1970] K. D. Usadel, Phys. Rev. Lett. **25**, 507 (1970).
- [Visani 1990a] P. Visani, A. C. Mota, and A. Pollini, Phys. Rev. Lett. **65**, 1514 (1990).
- [Visani 1990b] P. Visani, A. C. Mota, and A. Pollini, Physica B **165**& **166**, 1631 (1990).
- [Visani 1990c] P. Visani, *Superconducting proximity effect between silver and niobium*, Ph.D. thesis, ETH Zürich, 1990.
- [Volkov 1993] A. F. Volkov, A. V. Zaitsev, and T. M. Klapwijk, Physica C **210**, 21 (1993).
- [Volkov 1994] A. F. Volkov, Physica C **203**, 267 (1994).
- [van Wees 1992] B. J. van Wees, P. d. Vries, P. Magnée, and T. M. Klapwijk, Phys. Rev. Lett. **69**, 510 (1992).
- [Wilhelm 1998] F. K. Wilhelm, A. D. Zaikin, and H. Courtois, Phys. Rev. Lett. **80**, 4289 (1998).
- [Fazio 1996] C. Winkelholz, R. Fazio, F. W. J. Hekking, and G. Schön, Phys. Rev. Lett. **77**, 3200 (1996).
- [Wollman 1993] D. A. Wollman, D. J. Van Harlingen, W. C. Lee, D. M. Ginsberg, and A. J. Leggett, Phys. Rev. Lett. **71**, 2134 (1993).

- [Yip 1995] S. Yip, Phys. Rev. B, **52**, 15504 (1995).
- [Zaikin 1982] A. D. Zaikin, Solid State Commun. **41**, 533 (1982).
- [Zaitsev 1984] A. V. Zaitsev, Zh. Eksp. Teor. Fiz **86**, 1742 (1984) [Sov. Phys. JETP **59**, 1015 (1984)].
- [Zhou 1995] F. Zhou, B. Spivak, and A. Zyuzin, Phys. Rev. B **52**, 4467 (1995).

List of publications

- A. L. Fauchère, W. Belzig, and G. Blatter,
Paramagnetic Instability at Normal-Metal - Superconductor Interfaces,
Physical Review Letters 82, 3336 (1999).
- L. B. Ioffe, V. B. Geshkenbein, M. V. Feigel'man, A. L. Fauchère,
and G. Blatter, *Quiet SDS Josephson Junctions for Quantum Computing*,
Nature 398, 679 (1999).
- U. Ledermann, A. L. Fauchère, and G. Blatter,
Nonlocality in mesoscopic Josephson junctions with strip geometry,
Physical Review B 59, R9027 (1999).
- A. L. Fauchère, V. B. Geshkenbein, and G. Blatter,
*Comment on "Orbital Paramagnetism of Electrons in Proximity to a
Superconductor"*, Physical Review Letters 82, 1796 (1999).
- W. Belzig, C. Bruder, A. L. Fauchère,
Diamagnetic Response at Arbitrary Impurity Concentration,
Physical Review B 58, 14531 (1998).
- A. L. Fauchère, G. Lesovik, and G. Blatter,
Finite Voltage Shot Noise in Normal-Metal - Superconductor Junctions,
Physical Review B 58, 11177 (1998).
- A. L. Fauchère and G. Blatter
Magnetic Breakdown in a Normal-Metal - Superconductor Proximity Sandwich,
Physical Review B 56, 14102 (1997).
- G. Lesovik, A. L. Fauchère, and G. Blatter,
Nonlinearity in NS transport: Scattering Matrix Approach,
Physical Review B 55, 3146 (1997).
- J. Boutin and A. L. Fauchère,
Peptide Libraries: Statistical Evaluation of the Peptide Distribution,
Trends in Pharmacological Sciences (TiPS) 17, 8 (1996).

Curriculum Vitae

- 1/1996 – present Ph. D. research work and teaching assistance at the Institute for Theoretical Physics, Eidgenössische Technische Hochschule (ETH), Zurich, Switzerland
- 3/1999 Dissertation on *Transport and Magnetism in Mesoscopic Superconductors*, under the supervision of Prof. Dr. G. Blatter
- 10/1990 – 10/1995 Physics studies at the Eidgenössische Technische Hochschule (ETH), Zurich, Switzerland
- 10/1995 Masters in theoretical physics, with distinction, thesis on *Transport in Mesoscopic Metallic Cylinders*, with Prof. Dr. G. Blatter
- 12/1993 Nomination to the Swiss Study Foundation — Fonds for talented young people
- 4/1984 – 9/1990 High school, Kantonsschule Limmattal, Urdorf, Switzerland
- 9/1990 Diploma (Matura type B), with distinction
- 8/1988 – 7/1989 Student exchange program (AFS), Walnut Hills High School, Cincinnati, Ohio, USA
- 5/1989 Advanced Placement Exams of College Board
- 4/1978 – 3/1984 Elementary school, Geroldswil and Urdorf, Switzerland
- 21/5/1971 Born in Sion, Valais, Switzerland